Constraints on the global carbon budget from variations in total column carbon dioxide

Thesis by

Gretchen Keppel-Aleks

In Partial Fulfillment of the Requirements

for the Degree of

Doctor of Philosophy

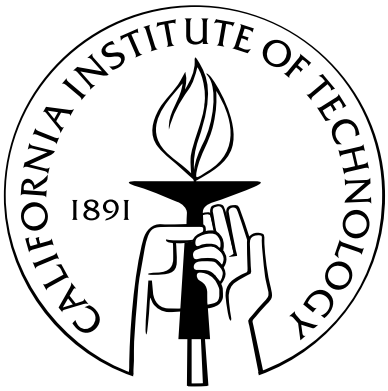

California Institute of Technology

Pasadena, California

2011

(Defended 20 May 2011)

To Bill and Ruth Anne

Acknowledgements

I have had the privilege to work with and learn from many outstanding scientists during my graduate studies at Caltech. I am fortunate that Paul Wennberg and Tapio Schneider both welcomed me into their research groups. Both Paul and Tapio have demonstrated the importance of doing meaningful science, and I appreciate the fresh ideas and the clarity that they bring to scientific research. I would like to thank Geoffrey Toon for patiently explaining the intricacies of Fourier transform spectrometry and retrieval theory, and most importantly for convincing me to start using vi when I first arrived at Caltech. I would like to thank the other members of my thesis committee, Simona Bordoni, and Yuk Yung, who have provided valuable suggestions and insight during graduate school.

This thesis would not be possible without the other scientific collaborators with whom I have been fortunate to work. Rebecca Washenfelder has been a good friend and invaluable mentor. Jean-Francois Blavier, Coleen Roehl, and Debra Wunch have been excellent teachers and collaborators. Coleen, as a fellow midwesterner with a healthy appreciation of the local cuisine and culture, has made trips to Park Falls more enjoyable. My research would not have gotten very far without the willingness of Jeff Ayers to caretake the TCCON container in Park Falls. Timothy Merlis and Yohai Kaspi have provided assistance with the GCM and are always a source of interesting scientific conversation. I would like to thank other members of the Wennberg and Schneider groups, including Kathleen Spencer, who has brightened the many hours spent in 102 North Mudd, Yael Yavin, Jason St. Clair, Melinda Beaver, Nathan Eddingsas, Fabien Paulot, John Crounse, David McCabe, Zhonghua Yang, Alan Kwan, Xavier Levine, Ian Eisenman, Paul O'Gorman, and Rob Korty.

Navigating graduate school has been made easier thanks to the dedicated administrative staff at Caltech. In particular, Dian Buchness, Marcia Hudson, Nora Oshima, and Irma Black have all been

extremely helpful. I also thank Alma Feuerabendt and Vince Riley, friendly faces at Braun Gym, for their willingness to lend an extra set of hands when I was working on the Lamont container.

Friends I have made at Caltech have enriched my time here. Aaron Wolf has made it easier and more exciting to put my principles regarding what constitutes a good life into action. Ashley Lawson, Xinning Zhang, and Sky Rashby became good friends during our first year of classes at Caltech. Many other people have made my years in Pasadena more exciting by sharing in hiking, cycling, culinary, and cultural adventures.

Experiences I had as an undergraduate are the reason I chose to come to Caltech. Greg Lawson's enthusiasm for weather forecasting and his friendly advice contributed to my decision to study atmospheric science, and I am happy to have overlapped with him at both MIT and Caltech. I would also like to thank Mario Molina and the members of his research group for encouraging me to pursue graduate research.

Finally, I would like to thank my family. My sisters Margaret and Rachel are outstanding. Rachel has provided me with both insight and distraction while I have worked on my PhD, and she is the person I admire most. My parents Ruth and Bill have made many sacrifices so that my sisters and I could pursue our educations. It is the work ethic and love of learning I learned from them that have made this dissertation a reality.

Abstract

Diagnosing the patterns and trends in the flux of carbon dioxide, CO_2, between the land or ocean and the atmosphere is necessary to predict the response of the carbon cycle to climate change. Atmospheric observations of the vertically averaged mixing ratio of CO_2, $\langle CO_2 \rangle$, provide a new tool that complements existing observations of boundary layer CO_2 in constraining surface fluxes of CO_2. My dissertation explores how variations in $\langle CO_2 \rangle$ arise and how these variations can be used to estimate surface fluxes.

This thesis takes advantage of $\langle CO_2 \rangle$ measurements from the Total Carbon Column Observing Network (TCCON). This global network uses ground-based Fourier transform spectrometers to obtain direct solar spectra in the near infrared, from which $\langle CO_2 \rangle$ is retrieved. Because variations in atmospheric CO_2 are relatively small, it is essential that the data achieve high precision and accuracy to be useful for carbon cycle science. Using a retrieval algorithm I developed to remove transient interference from clouds and aerosols, precise measurements are achievable under a range of meteorological conditions, allowing the inclusion of data from partially cloudy days.

At midlatitude TCCON sites, $\langle CO_2 \rangle$ varies substantially on diurnal, synoptic, and seasonal timescales. A comparison of diurnal variations in $\langle CO_2 \rangle$ with flux tower observations of net ecosystem exchange in northern Wisconsin suggests that local ecosystem fluxes account for only 10%–15% of variation in $\langle CO_2 \rangle$ on hourly timescales. I use an atmospheric transport model with imposed surface fluxes of CO_2 to examine further the sensitivity of $\langle CO_2 \rangle$ to surface fluxes and find that, as in the observations, simulated $\langle CO_2 \rangle$ is relatively insensitive to local phenomena. Large variations in local fluxes and local physics (e.g., convection) produce only small changes in atmospheric $\langle CO_2 \rangle$ patterns. Patterns in $\langle CO_2 \rangle$ are most sensitive to the large-scale north–south flux gradient, as zonal variations

in fluxes are smoothed by transport and therefore have little impact on the total column.

Rapid temporal variations in midlatitude $\langle CO_2 \rangle$ arise due to transport across north-south gradients, and can be used to infer information about large-scale spatial patterns in CO_2. Here, I use the correlation between synoptic-scale variations in $\langle CO_2 \rangle$ and dynamical tracers, such as potential temperature, to infer spatial gradients in large-scale $\langle CO_2 \rangle$ from sparse ground-based data. These estimated gradients, as well as the amplitude of the seasonal cycle in $\langle CO_2 \rangle$, can be used as diagnostics to evaluate flux models. In simulations with one such model, the Carnegie Ames Stanford Approach (CASA) ecosystem fluxes, gradients inferred from TCCON data are 75% larger than simulated CO_2 gradients during summer, while the seasonal cycle amplitudes in $\langle CO_2 \rangle$ at midlatitude TCCON sites are between 20% and 40% larger than in simulations. Given that $\langle CO_2 \rangle$ is insensitive to local fluxes, the mismatch between observations and simulations points to an underestimation of northern hemisphere ecosystem fluxes. Simulated $\langle CO_2 \rangle$ diagnostics are consistent with TCCON data if boreal net ecosystem exchange is increased by 40%, a finding that suggests boreal ecosystem parameterizations must be reevaluated.

This work demonstrates that variability in $\langle CO_2 \rangle$ is driven by large-scale phenomena rather than local fluxes, and has important implications for interpreting $\langle CO_2 \rangle$ measurements from satellites such as GOSAT and OCO-2. These results suggest that total column measurements will provide a strong constraint on large-scale flux estimates. At the same time, extracting information about regional fluxes from $\langle CO_2 \rangle$ observations alone will be challenging. Coupling column and surface CO_2 observations will yield improved flux estimates as surface CO_2 observations will constrain regional flux patterns, superimposed on top of the large-scale flux distribution revealed by total column observations.

Contents

List of Tables

List of Figures

List of Acronyms

AC – Alternating current

ACOS – Atmospheric Carbon Observations from Space

ADC – Analog-to-Digital converter

AM2 – a general circulation model

CASA – Carnegie-Ames-Stanford Approach biospheric model

DC – Direct current

FFT – Fast Fourier transform

FTS – Fourier transform spectrometer or Fourier transform spectrometry

GCM – General circulation model

GFIT – spectral retrieval fitting software

GOSAT – Greenhouse Gases Observing Satellite

HIPPO – Hiaper Pole-to-Pole Observations

INTEX-NA – Intercontinental Chemical Transport Experiment - North America

IPCC – Intergovernmental Panel on Climate Change

NASA – National Aeronautics and Space Administration

NEE – Net ecosystem exchange

NOAA – National Ocean and Atmosphere Administration

NPP – Net primary productivity

OCO – Orbiting Carbon Observatory

OPD – Optical path difference

SBF – Source brightness fluctuations

SCA – Seasonal cycle amplitude

SNR – Signal to noise ratio

TCCON – Total Carbon Column Observing Network

TM5 – a chemical transport model

WMO – World Meteorological Organization

ZPD – Zero path difference

Chapter 1

Introduction

1.1 The Coupled Carbon-Climate System

Since the onset of the industrial revolution, atmospheric greenhouse gases — so called because they absorb outgoing radiation, warming the Earth's surface — have increased substantially due to human activity (Le Quéré et al., 2009). Carbon dioxide, CO_2, the primary anthropogenic greenhouse gas, has increased from 280 ppm in 1850 to over 390 ppm in 2010 due to fossil fuel combustion and land use change (Marland and Rotty, 1984; van der Werf et al., 2009). Fossil fuel combustion has a relatively larger contribution to historical emissions than does land use change, accounting for $\sim$80% of anthropogenic CO_2 emissions. Currently, the concentration of CO_2 in the atmosphere is growing by $\sim$2 ppm y^{-1}, with fossil fuel combustion accounting for between 85% and 90% and land use change accounting for the remainder (van der Werf et al., 2009).

Increasing concentrations of atmospheric greenhouse gases will cause an increase in mean surface temperatures. Such an increase in mean surface temperature and associated climate variables such as precipitation could have a profound impact on ecosystems and human society. For instance, extreme weather conditions are expected to become more common as the Earth warms. Precipitation extremes are expected to become more intense, increasing the prevalence of drought conditions and potentially affecting agricultural productivity. Sea level will rise due to melting glaciers and thermal expansion of the oceans, affecting coastal populations. Seemingly smaller changes, such as predicted increases in minimum temperature, may reduce the frequency of frosts and allow the spread of plant

pathogens (Meehl et al., 2007).

The potential for wide-ranging impacts from global climate change necessitates accurate prediction of future climate. Although the radiative impacts of CO_2 and other greenhouse gases are well understood, future temperature changes are uncertain. Part of this uncertainty is simply that we cannot predict future concentrations of atmospheric greenhouse gases. Future fossil fuel emission levels are sensitive to international economic and political factors, which belie accurate predictions on even short timescales. In most climate simulations, future CO_2 levels have been prescribed to encompass multiple scenarios consistent with business as usual or with emissions reductions under an international climate treaty such as the Kyoto Protocol. These simulations show that at current atmospheric CO_2 concentrations, the climate system is committed to 0.5 K global mean warming, and that unmitigated future emissions will further increase surface temperatures (Meehl et al., 2007).

Even with a perfect prediction of anthropogenic CO_2 emissions, uncertainty in future atmospheric concentration would remain since concentration of atmospheric CO_2 is not determined solely by fossil fuel emissions of CO_2. Since the 1950s, natural sinks in the ocean and terrestrial biosphere have sequestered approximately one-half of fossil fuel CO_2 emissions each year (Gloor et al., 2010). This fraction varies significantly on interannual timescales, and the long-term response of natural fluxes to increasing CO_2 and changing climate is unknown.

Global climate simulations are only beginning to incorporate feedbacks between climate and the carbon cycle. One of the challenges to estimating future CO_2 levels is that the carbon cycle will change as surface temperatures and atmospheric CO_2 increases. At long timescales, the atmospheric concentration of CO_2 is in equilibrium with dissolved CO_2 in the ocean. Currently, the ocean is taking up CO_2 at a rate of $\sim$1.5 Pg C y^{-1}, but the solubility of CO_2 in seawater will decrease as the ocean warms. Moreover, dissolved CO_2 acidifies the ocean water, further decreasing the ultimate capacity of the ocean as an anthropogenic CO_2 sink (Archer et al., 2009).

Carbon is exchanged between the terrestrial biosphere and atmosphere through the coupled processes of photosynthesis and respiration. At steady state, the sum of these two processes, termed net ecosystem exchange, would be zero integrated over an annual cycle. Presently, rates of photosyn-

thesis exceed respiration globally, and there is a significant carbon sink ($\sim$ 2 Pg C y^{-1}) . This sink could be due to a number of factors including nutrient or CO_2 fertilization or longer growing seasons at higher latitudes (Randerson et al., 1997). Like the ocean sink, the capacity of the terrestrial biosphere to continue taking up anthropogenic CO_2 is sensitive to future climate.

1.2 Infering Fluxes from Atmospheric Observations

To understand how natural fluxes might change with climate, we require better understanding of present-day fluxes. Substantial research has attempted to quantify carbon fluxes, but such efforts are complicated by the fact that net fluxes of CO_2 are dwarfed by gross exchange among the atmosphere, biosphere, and oceans. The gross fluxes of CO_2 between the atmosphere and the oceans and the terrestrial biosphere are much larger than the net fluxes.

Two overarching approaches are used to constrain the global carbon cycle. Fluxes can be measured directly at a variety of locations and ecosystems and then upscaled, a so-called "bottom-up" approach (Saatchi et al., 2007; Davis et al., 2003). Bottom-up methods assume that a small-scale observation is representative of a larger area with similar vegetation types or climate. In contrast, a "top-down" approach involves reconciling observed variations in atmospheric CO_2 with surface fluxes. Top-down methods exploit the fact that the atmosphere integrates fluxes from across a finite-size footprint. Due to the sparseness of data, however, the integrated footprint of all CO_2 observations covers a small fraction of the Earth's surface and therefore cannot fully constrain fluxes.

The reason for this small footprint is that most measurements of atmospheric CO_2 have been made within the boundary layer. Such measurements are used in inverse modeling to optimize surface flux estimates (e.g., Gurney et al. (2002); Peters et al. (2007)). The TransCom experiment was developed to investigate the role of transport error on inverse estimates of CO_2. Sixteen different transport models were constrained by identical observation sets and prior flux estimates. In many regions, such as the tropics, boundary layer CO_2 observations were too sparse to reduce the uncertainty in the optimized flux compared to the prior flux estimates. Even in regions with dense data coverage, such as temperate North America, transport error led to large differences in the optimized

fluxes determined by the ensemble of transport models (Gurney et al., 2002).

Much of the difference in transport between the models owes to the fact that atmospheric processes such as convection occur on spatial scales smaller than the model resolution (i.e., subgridscale). Flux estimates constrained solely by boundary layer CO_2 are quite sensitive to errors in vertical mixing because on seasonal (as well as diurnal) timescales, fluxes and vertical mixing rates covary (Denning et al., 1995). For example, in northern hemisphere summer over terrestrial regions, CO_2 is depleted in the boundary layer due to photosynthesis; at the same time, vertical mixing is vigorous, which mixes relatively high–CO_2 air from aloft into the boundary layer. This induces a positive CO_2 anomaly at the surface relative to what the concentration would be if vertical mixing were constant across all seasons. Therefore, the vertical mixing parameterization in a given model can bias the optimized fluxes (Stephens et al., 2007).

1.3 Total Column CO_2

That robust flux estimates could not be obtained using boundary layer CO_2 observations in the TransCom experiment underscores the utility of new CO_2 observations with both better spatial coverage and less sensitivity to transport errors (Rayner and O'Brien, 2001). The total column measures the mass of gas in the column above a measurement site, and as such is independent of such factors as vertical mixing rates (Keppel-Aleks et al., 2011). Therefore, variations in the column can be more easily related to fluxes (Olsen and Randerson, 2004; Yang et al., 2007). Moreover, the column average mixing ratio of CO_2, $\langle CO_2 \rangle$, can be measured using remote sensing, enabling global observations from satellite platforms (Yang et al., 2002; Crisp et al., 2004).

Simulations show that moderate precision global data, such as would be observed from a satellite, leads to improvements in flux constraints beyond the current boundary layer observation network (Rayner and O'Brien, 2001). Because it is sensitive to CO_2 in the free troposphere, where horizontal mixing is more efficient, $\langle CO_2 \rangle$ has a substantially larger footprint than does boundary layer CO_2. Therefore, flux estimation using $\langle CO_2 \rangle$ will bridge spatial gaps between global flux estimates and more local flux estimates from direct flux observations or from boundary layer CO_2 data. Studies

have used column observations to provide a more robust flux constraint on northern hemisphere net ecosystem exchange (Yang et al., 2007).

In light of these benefits, several satellites have been launched to observe $\langle CO_2 \rangle$. SCIAMACHY, aboard the European Space Agency's ENVISAT, measures $\langle CO_2 \rangle$ using a grating spectrometer (Schneising et al., 2008), but the precision is insufficient for determination of regional surface fluxes (Breon and Ciais, 2010). In 2009, two satellites dedicated to $\langle CO_2 \rangle$ observations were launched. GOSAT, a Japanese satellite, uses a Fourier transform spectrometer to observed $\langle CO_2 \rangle$ (Yokota et al., 2009) whereas OCO, a NASA satellite, uses a grating spectrometer (Crisp et al., 2004). Due to mechanical problems, the OCO satellite failed to reach orbit, but a relaunch is planned for 2013. Both satellites are designed to record $\langle CO_2 \rangle$ at sufficient precision to infer natural fluxes of CO_2, and possibly even to monitor changes in fossil fuel CO_2 emissions.

1.4 The Total Carbon Column Observing Network

The Total Carbon Column Observing Network (TCCON) is a network of ground-based Fourier transform spectrometers (FTS) that measure column CO_2 using direct solar absorption spectrometry (Wunch et al., 2011). Although ground-based observations lack the spatial coverage of satellite observations (Fig 1.1), there are several advantages to ground-based measurements. The use of direct sunlight, rather than reflected sunlight as is used by GOSAT and OCO, increases incident photons and improves the signal to noise. Direct solar viewing also minimizes the influence of aerosols on the measurement, improving the precision and minimizing the opportunity for bias in the retrieved $\langle CO_2 \rangle$. Ground based TCCON sites are therefore used to validate satellite observations of $\langle CO_2 \rangle$. Beyond providing a validation of satellite $\langle CO_2 \rangle$ data, ground-based timeseries are fundamentally different in that they provide near continuous temporal coverage, allowing observation of diurnal and synoptic-scale variations in $\langle CO_2 \rangle$.

Each TCCON site is outfitted with a solartracker to actively track the center of the sun and uses a Bruker IFS 125 HR FTS, a commercially available and highly stable spectrometer, to record interferograms in the near infrared. The TCCON sites built by Caltech use dual acquisition on

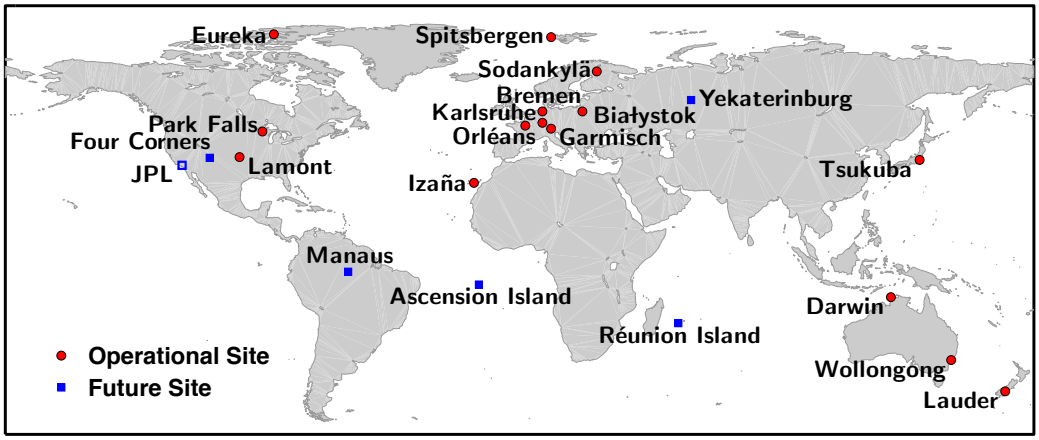

Figure 1.1: Map of TCCON observatories

two detectors, InGaAs (3800-10000 cm^{-1}) and Si Diode (12000-15500 cm^{-1}), to achieve broadband spectral coverage. Fourier transform spectrometers apply the principle of wave superposition to measure the spectral intensity of solar radiation (Brault, 1996). The incoming solar beam is divided using a dichroic CaF_2 beamsplitter and the two beams reflect off a fixed mirror and a scanning mirror. When the two beams recombine, they create an interference pattern whose intensity varies as a function of mirror distance. This interference pattern is then Fourier transformed to yield a spectrum that contains information on the atmospheric transmittance.

We use these spectra to infer the concentration of atmospheric trace gases including CO_2, CH_4, CO, H_2O, and O_2. We retrieve CO_2 from two spectral windows by scaling the a priori profile to best match the recorded spectrum in each window. The retrieved column abundance [mol m^{-2}] is normalized by the retrieved column abundance of O_2 to yield $\langle CO_2 \rangle$ [ppm] (Washenfelder et al., 2006). These data have been calibrated against aircraft profiles so that the measurements are traceable to World Meteorological Organization standards (Wunch et al., 2010). The precision and accuracy across the network are better than 0.2% (0.8 ppm). Such uniformity allows us to use the data from across the network in a joint analysis of hemispheric CO_2.

1.5 Organization of thesis

My doctoral research has focused on understanding how variations in $\langle CO_2 \rangle$ arise and how these variations can be related to surface fluxes. To use column observations for flux attribution, we require observations of sufficient precision and accuracy that variations in the data reflect real changes in $\langle CO_2 \rangle$. In chapter 2, I discuss an algorithm I helped develop to remove the influence of source brightness fluctuations from DC interferograms collected using Fourier transform spectrometry. This algorithm minimizes the loss of precision due to transient thin cloud or aerosol variations that occur during the acquisition of the interferograms. This algorithm enables data acquisition under a greater range of meteorological conditions.

In chapter 3, I discuss how variations arise in global $\langle CO_2 \rangle$ simulated by an atmospheric GCM with various underlying fluxes. In these experiments, I probe the sensitivity of $\langle CO_2 \rangle$ to local versus large-scale fluxes and show that variations in $\langle CO_2 \rangle$ primarily reflect large-scale flux patterns. I develop a method to estimate the meridional gradient in $\langle CO_2 \rangle$ from covariations in $\langle CO_2 \rangle$ and potential temperature, θ, a dynamical tracer, on synoptic timescales. I use the results of these simulations to provide diagnostics to link $\langle CO_2 \rangle$ variations to surface fluxes. These simulations illustrate how column observations from TCCON or from satellites such as OCO-2 or GOSAT could be used most effectively in inverse modeling.

In chapter 4, analysis of TCCON data from four midlatitude sites is presented. The data show that spatial gradients in $\langle CO_2 \rangle$ are larger during the growing season than can be accounted for with standard biospheric flux models. Both the seasonal cycle amplitude and the estimated meridional gradient in $\langle CO_2 \rangle$ in TCCON data suggest that growing season net flux in boreal forests is significantly larger than previously estimated.

Chapter 5 probes whether $\langle CO_2 \rangle$ measurements from space can be used to monitor fossil fuel CO_2 emissions. Global observations from satellites may be able to track changes in fossil fuel emissions through proper averaging of column data.

Bibliography

Archer, D., Eby, M., Brovkin, V., Ridgwell, A., Cao, L., Mikolajewicz, U., Caldeira, K., Matsumoto, K., Munhoven, G., Montenegro, A., and Tokos, K.: Atmospheric lifetime of fossil fuel carbon dioxide, Annu. Rev. Earth Pl. Sci., 37, 117–134, 2009.

Brault, J. W.: New approach to high-precision Fourier transform spectrometer design, Appl. Optics, 35, 2891–2896, 1996.

Breon, F. M, and Ciais, P.: Spaceborne remote sensing of greenhouse gas concentrations, Comptes Rendus Geoscience, 342, 412–424, 2010.

Crisp, D., Atlas, R. M., Breon, F. M., Brown, L. R., Burrows, J. P., Ciais, P., Connor, B. J., Doney, S. C., Fung, I. Y., Jacob, D. J., Miller, C. E., O'Brien, D., Pawson, S., Randerson, J. T., Rayner, P., Salawitch, R. J., Sander, S. P., Sen, B., Stephens, G. L., Tans, P. P., Toon, G. C., Wennberg, P. O., Wofsy, S. C., Yung, Y. L., Kuang, Z. M., Chudasama, B., Sprague, G., Weiss, B., Pollock, R., Kenyon, D., and Schroll, S.: The orbiting carbon observatory (OCO) mission, "Trace constituents in the troposphere and lower stratosphere" in the book series, Adv. Space Res., 34, 700–709, 2004.

Davis, K. J., Bakwin, P. S., Yi, C., Berger, B. W., Zhao, C., Teclaw, R. M., and Isebrands, J. G.: The annual cycles of CO_2 and H_2O exchange over a northern mixed forest as observed from a very tall tower, Global Change Biology, 9, 1278–1293, doi:10.1046/j.1365-2486.2003.00672.x, 2003.

Denning, A. S., Fung, I. Y., and Randall, D.: Latitudinal Gradient of Atmospheric CO_2 due to seasonal exchange with land biota, Nature, 376, 240–243, 1995.

Gloor, M., Sarmiento, J. L., and Gruber, N.: What can be learned about carbon cycle climate feedbacks from the CO_2 airborne fraction?, Atmos. Chem. Phys., 10, 7739–7751, 2010.

Gurney, K. R., Law, R. M., Denning, A. S., Rayner, P. J., Baker, D., Bousquet, P., Bruhwiler, L., Chen, Y.-H., Ciais, P., Fan, S., Fung, I. Y., Gloor, M., Heimann, M., Higuchi, K., John, J., Maki, T., Maksyutov, S., Masarie, K., Peylin, P., Prather, M., Pak, B. C., Randerson, J., Sarmiento, J.,

Taguchi, S., Takahashi, T., and Yuen, C.-W.: Towards robust regional estimates of CO_2 sources and sinks using atmospheric transport models, Nature, 415, 626–630, doi:10.1038/415626a, 2002.

Keppel-Aleks, G., Wennberg, P. O., and Schneider, T.: Sources of variations in total column carbon dioxide, Atmos. Chem. Phys., 11, 3581–3593, 2011.

Le Quéré, C., Raupach, M. R., Canadell, J. G., Marland, G., Bopp, L., Ciais, P., Conway, T. J., Doney, S. C., Feely, R. A., Foster, P., Friedlingstein, P., Gurney, K., Houghton, R. A., House, J. I., Huntingford, C., Levy, P. E., Lomas, M. R., Majkut, J., Metzl, N., Ometto, J. P., Peters, G. P., Prentice, I. C., Randerson, J. T., Running, S. W., Sarmiento, J. L., Schuster, U., Sitch, S., Takahashi, T., Viovy, N., van der Werf, G. R., and Woodward, F. I.: Trends in the sources and sinks of carbon dioxide, Nature Geoscience, 2, 831–836, doi:10.1038/ngeo689, 2009.

Marland, G. and Rotty, R. M.: Carbon-dioxide emissions from fossil-fuels - A procedure for estimation and results for 1950-1982, Tellus B, 36, 232–261, 1984.

Meehl, G. A., Stocker, T. F., Collins, W. D., Friedlingstein, P., Gaye, A. T., Gregory, J. M., Kitoh, A., Knutti, R., Murphy, J. M., Noda, A., Raper, S. C. B., Watterson, I. G., Weaver, A. J., Zhao, C.: Global Climate Projections. In Climate Change 2007: The Physical Science Basis. Contribution of Working Group I to the Fourth Assessment Report of the Intergovernmental Panel on Climate Change, Cambridge University Press, 2007.

Olsen, S. C. and Randerson, J. T.: Differences between surface and column atmospheric CO_2 and implications for carbon cycle research, J. Geophys. Res., 109, D02301, doi:10.1029/2003JD003968, 2004.

Peters, W., Jacobson, A. R., Sweeney, C., Andrews, A. E., Conway, T. J., Masarie, K., Miller, J. B., Bruhwiler, L. M. P., Pétron, G., Hirsch, A. I., Worthy, D. E. J., van der Werf, G. R., Randerson, J. T., Wennberg, P. O., Krol, M. C., and Tans, P. P.: An atmospheric perspective on North American carbon dioxide exchange: CarbonTracker, P. Natl Acad. Sci., 104, 18925–18930, doi:10.1073/pnas.0708986104, 2007.

Randerson, J. T., Thompson, M. V., Conway, T. J., Fung, I. Y., and Field, C. B.: The contribution of terrestrial sources and sinks to trends in the seasonal cycle of atmospheric carbon dioxide, Global Biogeochem. Cy., 11, 535–560, 1997.

Rayner, P. J. and O'Brien, D. M.: The utility of remotely sensed CO_2 concentration data in surface source inversions, Geophys. Res. Lett., 28, 175–178, 2001.

Saatchi, S. S., Houghton, R. A., Alvala, R. C. D. S., Soares, J. V., and Yu, Y.: Distribution of aboveground live biomass in the Amazon basin, Global Change Biol., 13, 816–837, doi:10.1111/j.1365-2486.2007.01323.x, 2007.

Schneising,O., Buchwitz, M., Burrows, J. P., Bovensmann, H., Reuter, M., Notholt, J., Macatangay, M., and Warneke, T.: Three years of greenhouse gas column-averaged dry air mole fractions retrieved from satellite - Part 1: Carbon dioxide, Atmos. Chem. Phys. 8, 3827–3853, 2008.

Stephens, B. B., Gurney, K. R., Tans, P. P., Sweeney, C., Peters, W., Bruhwiler, L., Ciais, P., Ramonet, M., Bousquet, P., Nakazawa, T., Aoki, S., Machida, T., Inoue, G., Vinnichenko, N., Lloyd, J., Jordan, A., Heimann, M., Shibistova, O., Langenfelds, R. L., Steele, L. P., Francey, R. J., and Denning, A. S.: Weak northern and strong tropical land carbon uptake from vertical profiles of atmospheric CO_2, Science, 316, 1732–1735, doi:10.1126/science.1137004, 2007.

van der Werf, G. R., Morton, D. C., DeFries, R. S., Olivier, J. G. J., Kasibhatla, P. S., Jackson, R. B., Collatz, G. J., and Randerson, J. T.: CO_2 emissions from forest loss, Nature Geosci., 2, 737–738, doi:10.1038/ngeo671, 2009.

Washenfelder, R. A., Toon, G. C., Blavier, J.-F., Yang, Z., Allen, N. T., Wennberg, P. O., Vay, S. A., Matross, D. M., and Daube, B. C.: Carbon dioxide column abundances at the Wisconsin Tall Tower site, J. Geophys. Res., 111, D22305, doi:10.1029/2006JD007154, 2006.

Wunch, D., Toon, G. C., Wennberg, P. O., Wofsy, S. C., Stephens, B. B., Fischer, M. L., Uchino, O., Abshire, J. B., Bernath, P., Biraud, S. C., Blavier, J. F. L., Boone, C., Bowman, K. P., Browell, E. V., Campos, T., Connor, B. J., Daube, B. C., Deutscher, N. M., Diao, M., Elkins, J. W.,

Gerbig, C., Gottlieb, E., Griffith, D. W. T., Hurst, D. F., Jimenez, R., Keppel-Aleks, G., Kort, E. A., Macatangay, R., Machida, T., Matsueda, H., Moore, F., Morino, I., Park, S., Robinson, J., Roehl, C. M., Sawa, Y., Sherlock, V., Sweeney, C., Tanaka, T., and Zondlo, M. A.: Calibration of the Total Carbon Column Observing Network using aircraft profile data, Atmos. Meas. Tech., 3, 1351–1362, 2010.

Wunch, D., Toon, G. C., J.-F. L, Blavier, Washenfelder, R. A., Notholt, J., Connor, B. J., Griffith, D., Sherlock, V., and Wennberg, P.: The Total Carbon Column Observing Network, Phil. Trans. R. Soc. A, 369, 2087–2112, 2011.

Yang, Z. H., Toon, G. C., Margolis, J. S., and Wennberg, P. O.: Atmospheric CO_2 retrieved from ground-based near IR solar spectra, Geophys. Res. Lett., 29, 1339, 2002.

Yang, Z., Washenfelder, R. A., Keppel-Aleks, G., Krakauer, N. Y., Randerson, J. T., Tans, P. P., Sweeney, C., and Wennberg, P. O.: New constraints on Northern Hemisphere growing season net flux, Geophys. Res. Lett., 34, L12807, doi:10.1029/2007GL029742, 2007.

Yokota, T., Yoshida, Y., Eguchi, N., Ota, Y., Tanaka, T., Watanabe, H., and Maksyutov, S.: Global Concentrations of CO_2 and CH_4 Retrieved from GOSAT: First Preliminary Results, Sola, 5, 160–163, 2009.

Chapter 2

Reducing the impact of source brightness fluctuations on spectra obtained by Fourier-transform spectrometry*

2.1 Introduction

Traditionally, a high-pass analog filter has been used in Fourier transform spectrometry (FTS) signal chains. This method, called AC recording, has been preferred over DC recording (in which the detector signal is not high-pass filtered prior to digitization) for two reasons. First, most ADCs encompass positive and negative values, so recentering the interferogram at zero, as is done in AC recording, enables the full dynamic range of the ADC to be utilized without the complication of subtracting an electrical offset. Second, AC recording facilitates gain switching, necessary in high-resolution FTS to resolve the interferogram at both high and low optical path difference (OPD). At low OPD — the center burst of the interferogram — the fringes are several orders of magnitude larger in amplitude than those at high OPD. Use of a single gain to record the interferogram requires that the signal be sampled with very large dynamic range (greater than 16-bit resolution), typically in excess of the range available for fast ADCs. Therefore, gain switching during a scan is employed on many high-resolution FTS instruments to avoid saturation of the interferogram at low OPD while

*Adapted from "Reducing the impact of source brightness fluctuations on spectra obtained by Fourier transform spectrometry" by G. Keppel-Aleks, G. C.Toon, P. O. Wennberg, and N. M. Deutscher, *Applied Optics*, 46, 4774–4779, 2007.

amplifying the small fringes at high OPD sufficiently to avoid digitization noise. To accomplish this, the large DC term must be eliminated to center the interferogram at 0 V, consistent with the usual bipolar ADC inputs.

AC recording entails loss of information regarding source brightness fluctuations (SBF) that occur during interferogram acquisition. Since SBF are multiplicative, their effect cannot be removed simply by high-pass filtering; the high frequency interferogram fringes have been amplitude-modulated. Spectrometrists have long recognized that "ratio-recording" reduces the impact of variations in source intensity and have gone to great lengths to implement ratio-recording techniques (e.g., Ahlers et al. (1955)). FTS systems are even more sensitive to such variations than are grating spectrometers due to the fact that the low and high resolution information is not acquired simultaneously. Because the zero path difference (ZPD) region of the interferogram sets the continuum level of the resulting spectrum, while the high OPD fringe amplitudes determine the line depths, SBF during sampling of the interferogram affect broad and narrow spectral features differently. Intensity loss at one region of the interferogram can therefore distort the fractional line depths, since SBF lead to multiplicitave modulation of fringe amplitude.

The DC interferogram can be used to correct for SBF, minimizing the errors that such fluctuations introduce into the spectra. By use of an appropriate digital filter, the low frequency variation due to SBF can be separated from the higher frequencies that contain the interferometrically modulated energy. Knowledge of this DC intensity can then be used to correct for slow variations in source intensity as an interferogram is obtained. This is a fundamentally different approach than that of Shao et al. (2007), who attempt to identify and reject interferograms affected by SBF.

We present here a method and an algorithm that correct for SBF. DC interferograms are passed through a low-pass filter, and the resulting low-pass signal is used to normalize all regions of the interferogram. In reweighting the interferogram, the relative line depth to continuum level ratio is corrected as the fringes altered by SBF are normalized. Use of inexpensive high dynamic range delta-sigma ADCs (24 bits) facilitates such a correction. The large dynamic range eliminates the need for gain switching to properly resolve the high OPD regions of the interferogram. A single interferogram

can then be recorded in low gain without high-pass filtering. Although not demonstrated here, similar benefits could be derived from a lower resolution ADC with two output channels: a low gain DC interferogram and a high gain AC interferogram. The low gain, smoothed DC term would be sufficiently resolved to reweight an interferogram derived from the two channels.

In section 2.2, we present our methodology for correcting DC interferograms and our reweighting algorithm. In sections 2.3 and 2.4, we discuss the application of the reweighting algorithm to solar absorption spectrometry and present a comparison between data processed with and without the reweighting algorithm. Section 2.5 examines the efficacy of the reweighting algorithm in processing spectra affected by nongray SBF. The influence of detector nonideality on the reweighted interferogram is discussed in section 2.6.

2.2 Methods

The algorithm devised to correct for intensity variations is straightforward and had been suggested in the past by Brault (1985). We take a real-to-complex fast Fourier transform of the raw DC interferogram. To the resulting spectrum we apply the spectral filter of equation 2.1, which retains frequencies below the cutoff frequency s.

$$F = \begin{cases} \left(\frac{1+cos(\frac{\pi\nu}{s})}{2}\right)^N & \text{if } \nu < \text{s} \\ 0 & \text{if } \nu > \text{s} \end{cases} \tag{2.1}$$

We choose $s = 300$ cm^{-1} (180 s^{-1}) corresponding to 8% of the low frequency detection limit for the spectra described here, and N=8. The frequency cutoff, s, should be minimized such that it is smaller than the lowest frequency at which interferometric modulation is measured, while still larger than the characteristic SBF frequency. The parameter N determines the steepness of the filter cutoff. A large difference between the characteristic SBF frequency and the low frequency detection limit allows a wider range of permissible s values, and lowers the sensitivity to choice of N. In instances where the highest SBF frequency and the low frequency detection limit are similar, a higher value of N is desired to increase the filter steepness. We discuss the sensitivity of the data

to choice of s in section 2.6.

We take the inverse Fourier Transform of the low-frequency spectrum that results from equation 2.1 using a complex-to-real routine. The resulting low pass-filtered interferogram provides a measure of the SBF at frequencies well below the signal due to interferometric modulation. Ratioing the raw interferogram to this smoothed interferogram yields an interferogram with constant DC level of one, with all regions of the interferogram having a uniform intensity weighting.

$$I_{corr}(x) = \frac{I_{raw}(x)}{I_{smooth}(x)} \cdot I_{smooth}(ZPD) \tag{2.2}$$

We choose to scale the reweighted interferogram by the DC level at ZPD, as written in equation 2.2, so that each interferogram retains information on the absolute intensity at ZPD, which is helpful in many applications. The corrected interferogram can then be processed using standard interferogram processing routines.

2.3 Application

SBF affect many spectra obtained by FTS. Remote sensing is particularly susceptible as scene brightness often changes during the acquisition of an interferogram. We illustrate the benefits of the reweighting algorithm with measurements of infrared solar spectra obtained from the Earth's surface. Ground-based direct solar absorption spectrometry is a common technique used to infer atmospheric composition. High resolution FTS has been used historically by the Network for the Detection of Atmospheric Composition Change (previously called the Network for the Detection of Stratospheric Change) (Kurylo and Solomon, 1990). Although using the sun as a source provides excellent signal-to-noise, the source intensity can vary on the timescale of a single scan due to attenuation by clouds and aerosol. Such variability degrades the accuracy and precision of gas amounts retrieved from such spectra.

In our application, we use near infrared solar absorption spectra to obtain total column abundance of atmospheric gases including O_2, CO_2, CO, CH_4, and H_2O (Washenfelder et al., 2006). These

measurements are obtained at sites affiliated with the Total Carbon Column Observing Network (TCCON) (Wunch et al., 2011). The goal of TCCON is to provide constraints on variability in surface fluxes of CO_2. To accomplish this, it is desired to obtain precisions in column retrievals better than 0.5%. To meet the required precision without the DC correction, interferograms obtained with high SBF, as determined by a measurement of the total solar intensity on a solar tracker quadrant sensor, were discarded. Eliminating these spectra greatly reduced the range of atmospheric conditions under which worthwhile observation was possible. Even optically thin clouds crossing the field of view of the instrument rendered the measurements unusable. Incorporation of the DC correction allows many of these otherwise-discarded spectra to be used.

Data are obtained using a Bruker IFS 125HR Fourier Transform Spectrometer. The instrument is optimized for recording in the near infrared, with gold coated optics and a CaF_2 beamsplitter. A solar tracker with a silicon quadrant sensor centers the solar image on the entrance fieldstop of the FTS. We record the solar intensity at the quadrant sensor at a rate of 0.5 Hz over the 90 s duration of a single-sided scan. The ratio of the standard deviation to the mean of the solar intensity represents the solar intensity variation. If the variation measured by the quadrant sensor for a given interferogram falls below a threshold, we transform the interferogram and retrieve gas columns from the spectrum. Interferograms are recorded on two detectors simultaneously. We obtain full spectral coverage between 3800 and 15750 cm^{-1} using an InGaAs detector (3800-11000 cm^{-1}), and a Si diode detector (10000-15750 cm^{-1}). The detectors are coupled to a 24 bit delta-sigma ADC. We obtain direct solar absorption spectra at 0.02 cm^{-1} resolution (45 cm OPD) and a scan velocity of 10 kHz. For more information on the experimental setup and analysis procedure, see (Washenfelder et al., 2006).

2.4 Results

Figure 2.1a shows an interferogram obtained in DC mode on the InGaAs detector. The smoothed, low-pass signal is shown in Fig. 2.1b. This interferogram was obtained with solar intensity variation of 14%; because intensity decreased during the scan, the weight of the high OPD regions of the

corrected interferogram, shown in Fig. 2.1c, has been increased, amplifying those fringes and restoring the spectral lines to their correct depths. The reweighted interferogram is then transformed using slice-ipp, a fast Fourier transform algorithm developed at NASA JPL, which phase corrects the interferogram prior to taking the real-to-complex FFT. We use GFIT, a line-by-line nonlinear least-squares fitting program also developed at NASA JPL to determine atmospheric composition from the spectra.

We test the algorithm by comparing atmospheric column amounts retrieved from spectra derived both from reweighted interferograms and from control DC interferograms that have not been reweighted. We use data from both cloudy and clear days to determine the effect of the algorithm on both high quality and potentially compromised data.

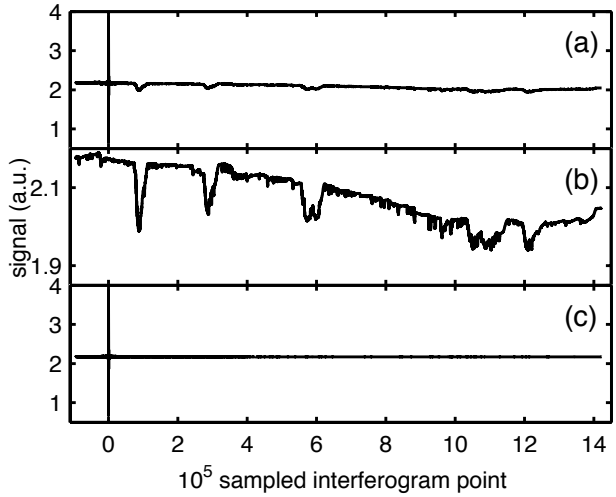

Figure 2.1: (a) Raw DC interferogram with 14% solar intensity variation. (b) Smoothed, low-pass signal. (c) Corresponding reweighted interferogram.

Retrievals from the spectra obtained from the reweighted interferograms show substantially increased precision compared to control data. Shown in Fig. 2.2 are the CO_2 columns retrieved from FTS spectra measured at the US Department of Energy Atmospheric Radiation Measurement site in Darwin, Australia ($-12.4°$ S, $130.9°$ E) on 29 October 2005. This day was characterized by partly cloudy skies with solar intensity variations between 2% and 50% during individual scans. As the site is coastal, we expect minimal diurnal variability in CO_2. We retrieve near constant gas columns from the reweighted data over the range of observed solar intensity variation, in contrast to the control

data where the scatter in the retrieved columns becomes large at high solar variation. The inset to Fig. 2.2 shows that the reweighting algorithm reduces the scatter and gives more consistent retrievals even when solar intensity variations fall below 10%. For the full data set of 227 control scans, the column mean is 8.19×10^{21} molecules cm^{-2}, with a standard deviation of the 227 column values of 6.1×10^{20} molecules cm^{-2}, or 7%. In contrast, the reweighted data has a mean column retrieval of 8.25×10^{21} molecules cm^{-2}, and the standard deviation of the retrievals is 0.6×10^{20} molecules cm^{-2} or 0.7%, an order of magnitude lower. For scans taken with solar intensity variation less than 10%, the standard deviation in the measurements is also reduced by an order of magnitude from 2.5% to 0.25% for the control and reweighted data, respectively.

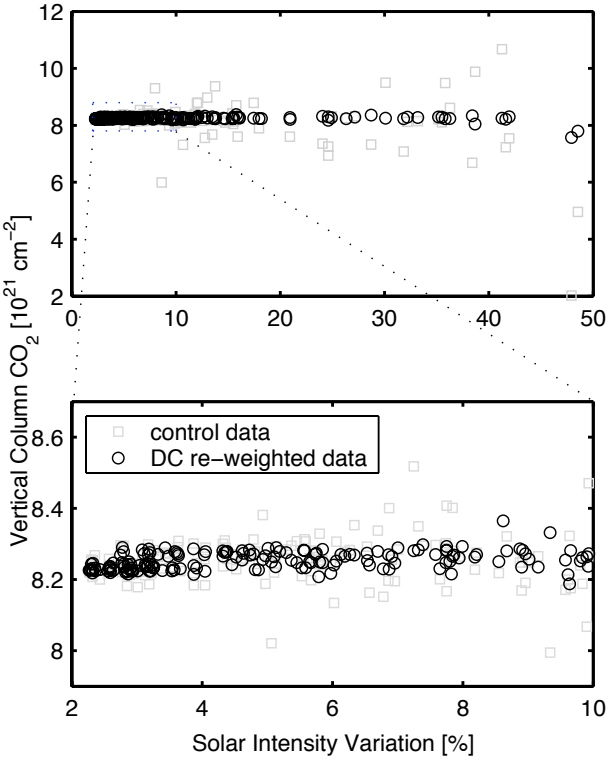

Figure 2.2: A comparison between CO_2 retrievals from reweighted (dark circles) and the raw control (light squares) spectra as a function of relative solar intensity variation during a 90 s scan. The lower panel zooms in on relative solar intensity variation below 10%.

To test whether the reweighting algorithm introduces a bias to the gas retrievals, we use data obtained at Darwin when solar intensity variations were below 3% for all scans recorded. As shown in Fig. 2.3, we see a small negative bias in the reweighted data. For the 238 scans used from 19

December 2005, the mean difference is -0.016%, with a standard deviation of 0.048% and a standard error of the sampling distribution of 0.003%, indicating a statistically significant negative bias in the reweighted data. This bias could be real: the gas columns determined in the control analysis could be higher than the true atmospheric column. We do not have perfect data completely unaffected by SBF on which to test the algorithm, so we must use data with solar intensity variation less than 3% as a proxy. This bias could also be due to artifacts near ZPD in the smoothed interferogram, which will be discussed further in section 2.6. In either case, the 0.02% bias is quite small and is undetectable in observations made at solar intensity variation between 3% and 50%. As seen in Fig. 2.3, the difference between the corrected and uncorrected CO_2 column is generally less than 0.1%, with the largest differences at solar intensity variation approaching 3%. The data suggest that the algorithm improves scatter in the retrievals at all solar intensity variations, with its impact on retrievals increasing with solar intensity variation.

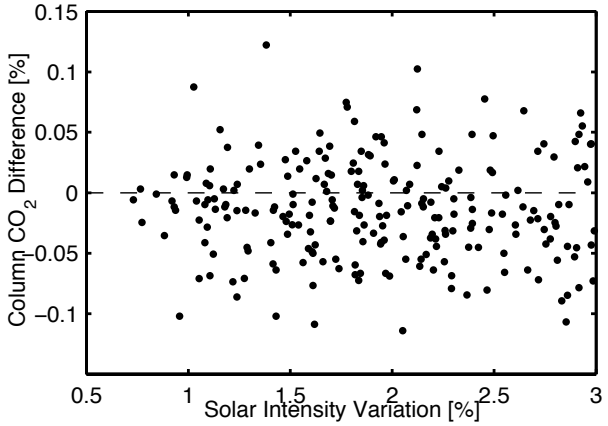

Figure 2.3: The percent difference between CO_2 retrievals from spectra obtained from reweighted and control interferograms with solar intensity variation less than 3%.

Based on the performance of the algorithm in improving retrievals, we have transformed the data obtained at Darwin from August 2005 to August 2006 using the DC reweighting algorithm. DC acquisition was first implemented in late October 2005, so the first two months of data were obtained in AC mode using a high-pass filter. Fig. 2.4 shows the O_2 volume mixing ratio retrieved at solar intensity variations less than 20%. Note the dramatic transition between the AC and DC regimes. Prior to implementing DC recording, we used a threshold of 2% solar intensity variation to

obtain a high precision record under AC acquisition. Using this threshold, we would have discarded all interferograms obtained on 85 out of 286 days between August 2005 and August 2006. Using a higher cutoff of 20% for DC data, the DC reweighting algorithm has enabled us to include data from those 85 days and improve the quality of the data from the other 201 days.

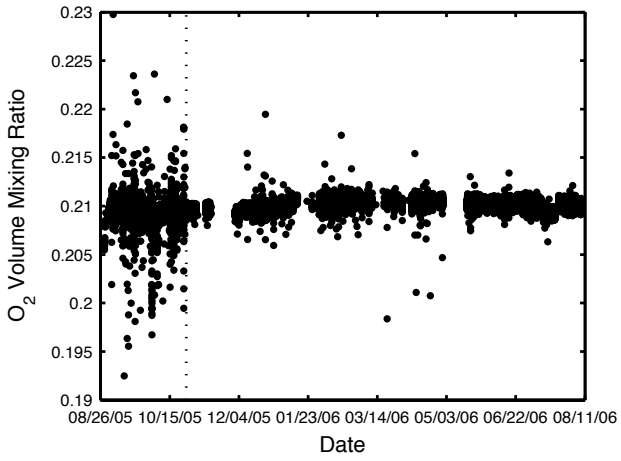

Figure 2.4: Time series of the oxygen mixing ratio retrieved from spectra at Darwin, Australia. Prior to November 2005, AC data acquisition was used. Plotted here are data obtained between 20 and 70 degree solar zenith angle. Only spectra obtained with relative solar variation less than 20% are shown.

The signal-to-noise ratio (SNR) of the spectra decreases by approximately 20%, from 840 to 660 near the peak of the InGaAs spectrum and from 390 to 320 near the peak of the Si spectrum, when we switch from AC to DC acquisition. We stress that this reduction in SNR has a negligible effect on our total error budget compared to the errors introduced by uncorrected SBF. The gain of an order of magnitude in precision and the increase to the range of atmospheric conditions in which measurements can be used both far outweigh this 20% reduction in SNR.

2.5 Nongray source brightness fluctuations

The theory behind the SBF correction method described here is valid for gray source intensity fluctuations: if the shape of the spectrum remains unchanged, and only its intensity varies, the DC correction should be perfect. However, clouds and aerosol in the atmosphere scatter light preferentially at shorter wavelengths; SBF are thus larger at shorter wavelength than at longer

wavelength (i.e., nongray).

To examine the effect of nongray SBF on our gas retrievals, we distort a sample of ideal interferograms with low relative solar intensity variations (0.5%-3%) to simulate the effects of nongray intensity fluctuations. Although the effects of nongray attenuation could be investigated using a stable light source, we chose instead to model the effects of nongray SBF as no such lamp was available. We Fourier transform an ideal interferogram and use $S_{distorted}(\nu) = S_{original}(\nu)\exp(-\tau(\nu/15750)^{\alpha})$ to distort the resulting spectrum for ν between 300 and 15750 cm^{-1}, increasing the value of τ to increase total attenuation (Fig. 2.5a). We choose angstrom exponent, α, of 0.3, a realistic value for clouds in the atmosphere. The ratio of the area under the distorted spectrum to that of the original spectrum between the frequency limits is used to scale the ν=0 point of the distorted DC spectrum and the associated ringing at frequencies below 300 cm^{-1}. The distorted spectra are inverse transformed; the resulting interferograms (Fig. 2.5b) have been influenced by time-independent, nongray attenuation.

We interpolate between the attenuated interferograms to create an interferogram that exhibits a temporal dependence to the modeled nongray attenuation (Fig. 2.5c). This interferogram is then reweighted using the DC correction algorithm (Fig. 2.5d). The control and reweighted interferograms are transformed (Fig. 2.5e,f), and gas columns are retrieved from each spectrum. We have simulated two forms of transience: total intensity linearly falling off by 50% at high OPD and total intensity linearly increasing by a factor of 2 from ZPD to maximum OPD.

We retrieve CO_2 and O_2 from two different bands to determine the performance of the DC reweighting algorithm. The nongray distortion introduces errors of 1%-4% that are dependent on the characteristics of the fitting window and on the temporal distribution of the distortion. Table 2.1 shows the impact of these simulations on retrievals from the three bands: CO_2 6180-6260 cm^{-1}, O_2 7765-8005 cm^{-1}, and O_2 12940-13190 cm^{-1} (A-band).

The distorted interferograms that have been reweighted using our algorithm have errors less than 0.4%, in contrast to errors of several percent in data obtained without using the reweighting algorithm. These simulations demonstrate that the method is robust to nongray SBF. In the simulations

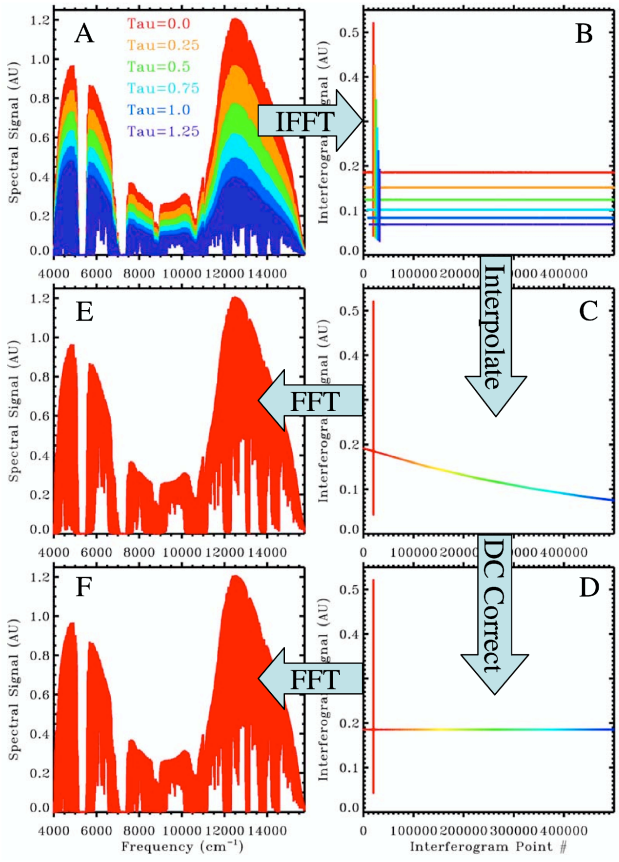

Figure 2.5: A spectrum distorted with nongray interference of optical depth ranging from 0.0 (original spectrum) to 1.25 at 15750 cm^{-1} (Panel A). The spectra are inverse Fourier transformed to yield the interferograms in panel B. We interpolate between these interferograms to generate the interferogram in panel C, which exhibits spectrally- and temporally-dependent attenuation compared to the original interferogram. The attenuated interferogram is reweighted using the DC correction to yield the interferogram in panel D. We then transform each interferogram to yield the control spectrum in panel E, and the reweighted spectrum in panel F. Although the spectra in E and F appear identical, the line depths in the uncorrected spectrum (E) are more shallow than those in panel F.

described in Table 2.1, we use an angstrom exponent of 0.3 which is a realistic spectral dependence for SBF due to clouds. We further simulated SBF with angstrom exponent as large as 4.0 and still see significant improvements, with errors generally smaller than 0.2% in the column retrievals from reweighted interferograms. We therefore recommend use of this algorithm for DC-recorded data in all situations, even when the interference exhibits spectral dependence.

Table 2.1: Retrieval errors [%] from spectra distorted by nongray SBF.

Retrieved Species	Low OPD Distortion		High OPD Distortion	
	control	reweighted	control	reweighted
CO_2 (6180-6260 cm^{-1})	4.185	0.081	-1.902	-0.017
O_2 (7765-8005 cm^{-1})	3.264	0.368	-1.442	-0.084
O_2 (12940-13190 cm^{-1})	-0.549	-0.012	0.216	-0.004

2.6 Artifacts at ZPD

The reweighting method is sensitive to non-ideal detector behavior near ZPD (Fig. 2.6a). In addition to choosing s in equation 2.1 below the low frequency detection limit but above SBF frequency, the filter cutoff can be selected to minimize artifacts resulting from detector nonideality. When using a filter cutoff 80% of our low spectral frequency limit (3000 cm^{-1}), we observed a dip in the low-pass signal at ZPD (Fig. 2.6b). We attribute this dip to detector nonlinearity. Although not discussed further here, this dip can be used to diagnose, model, and account for nonlinearity in the detector. When the frequency cutoff is reduced to 8% of the low frequency limit (300 cm^{-1}), these artifacts are no longer visible, as demonstrated in Fig. 2.6c. The presence of an artifact at ZPD in the smoothed interferograms can bias the resulting fits. The dips at ZPD amplify the center burst of the reweighted interferogram, raising continuum levels and inducing a negative bias in the retrievals from reweighted data an order of magnitude larger than the 0.02% bias observed when s is 8% of the low frequency detection limit. The detector at Darwin exhibits only a small nonlinearity; it is possible that for a detector with a higher degree of nonlinearity, a suitable choice of s above the SBF frequency would not be sufficiently low in frequency to smooth away the artifact observed in Fig. 2.6b. In such a case, the DC correction algorithm would need to be modified to correct for detector non-linearity as well.

2.7 Conclusion

The influence of SBF on spectra recorded using DC signal processing can be substantially minimized by a simple reweighting algorithm. We expect this correction method will have an increasingly signif-

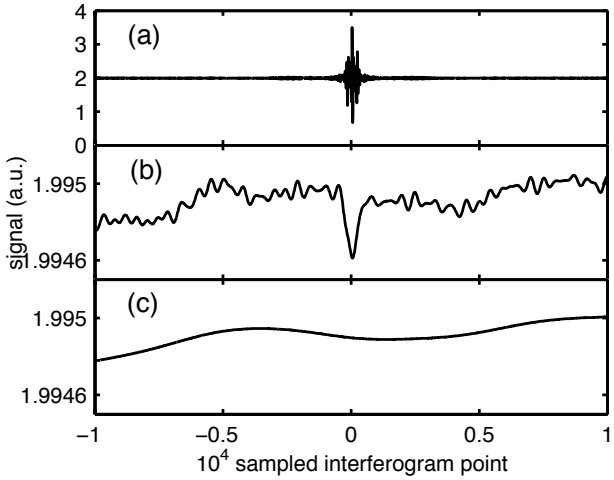

Figure 2.6: (a) Center burst of raw interferogram. (b) Low-pass signal resulting from filter with s = 3000 cm^{-1}. The observed dip at ZPD is likely due to detector nonlinearity. (c) Low-pass interferogram resulting from filter with s = 300cm^{-1}. The dip at ZPD has been smoothed away in lowering the frequency cutoff.

icant impact on choices made regarding DC versus AC interferogram acquisition, especially as higher resolution ADCs become more prominent in FTS. Even without high resolution ADCs, DC recording of low gain interferograms provides the essential tools for separating the low frequency source variations from high frequency interferometric modulation, enabling source brightness fluctuations to be corrected.

Bibliography

Ahlers, N. H. E. and Freedman, H. P.: A simple ratio-recording spectrometer, J. Sci. Instrum., 32, 1955.

Brault, J.W. "Fourier Transform Spectrometry" in *High Resolution in Astronomy*, R.S. Booth, J.W. Brault, A. Labeyrie, Swiss Society of Astrophysics and Astronomy, 3-62, 1985.

Kurylo, M.J., and S. Solomon. Network for the Detection of Stratospheric Change, NASA report, Code EEU, Washington, D.C., 1990.

Shao, L., M.J. Pollard, P.R. Griffiths, D.T. Westermann, and D.L. Bjorneberg: Rejection criteria

for open-path Fourier transform infrared spectrometry during continuous atmospheric monitoring, Vibrational Spectroscopy, 43, 78-85, 2007.

Washenfelder, R. A., Toon, G. C., Blavier, J.-F., Yang, Z., Allen, N. T., Wennberg, P. O., Vay, S. A., Matross, D. M., and Daube, B. C.: Carbon dioxide column abundances at the Wisconsin Tall Tower site, J. Geophys. Res., 111, D22305, doi:10.1029/2006JD007154, 2006.

Wunch, D., Toon, G., J.-F.L, Blavier, Washenfelder, R., Notholt, J., COnnor, B., Griffith, D., Sherlock, V., and Wennberg, P.: The Total Carbon Column Observing Network, Phil. Trans. R. Soc. A, 369, 2087–2112, 2011.

Chapter 3

Sources of variations in total column carbon dioxide*

3.1 Introduction

Diagnosing the patterns and trends in the flux of carbon dioxide, CO_2, between the land or ocean and the atmosphere is a longstanding interest of the carbon cycle community. Such information is needed, for example, to evaluate models of future climate and for evaluating the effectiveness of proposed climate change mitigation strategies.

Direct measurements of fluxes can be made on small spatial scales, but global accounting requires either extrapolation of regional-scale flux observations or use of atmospheric observations of CO_2 to infer fluxes indirectly. Inverse modeling represents one approach for estimating regional and global carbon fluxes from gradients in the observed concentration (or mixing ratio) of CO_2, $[CO_2]$ (Gurney et al., 2002, 2004). Typically, atmospheric transport models are used to simulate global CO_2 fields, given estimates of regional CO_2 fluxes owing to fossil fuel emissions, ocean-atmosphere exchange, and biosphere-atmosphere exchange; the estimated fluxes are then adjusted to best match the observations.

Accurate estimation of CO_2 fluxes using inverse techniques is quite challenging. The sparseness of the data set and the fact that most observations are from the surface or near the surface place considerable demands on the accuracy of the velocity fields in the transport model (Denning et al.,

*Adapted from "Sources of variations in total column carbon dioxide" by G. Keppel-Aleks, P.O. Wennberg, and T. Schneider, *Atmospheric Chemistry and Physics*, 11, 3581–3593, 2011

1995). In particular, studies have illustrated that the inference of regional fluxes is highly sensitive to the representation of subgrid-scale boundary layer dynamics in transport models (Stephens et al., 2007). The use of surface [CO_2] observations in such studies is further complicated by the diurnal and seasonal "rectifier effect", the covariance between surface CO_2 fluxes and the strength of vertical mixing (Denning et al., 1995). In contrast, column data provide a constraint on the total mass of CO_2 in a column, and so are more closely related to the underlying fluxes. Observations of column CO_2 from remote sensing platforms such as GOSAT and OCO-2 (Yokota et al., 2009; Crisp et al., 2004) and from ground-based observatories are anticipated to provide better constraints on the exchange of CO_2 between the atmosphere and the surface (Olsen and Randerson, 2004; Chevallier et al., 2007).

Observed variations of atmospheric CO_2 in time and space are the fundamental data constraint in all inverse studies. Studies suggest that gradients in free tropospheric CO_2 concentrations can differ substantially from gradients at the surface (Miyazaki et al., 2008, 2009). Here, we examine how variations in the total CO_2 column, $\langle CO_2 \rangle$, arise. In particular, we investigate how local, regional, and global fluxes are expressed in variations in $\langle CO_2 \rangle$. We use a global general circulation model (GCM) with prescribed fluxes to determine how changes in the pattern of fluxes alter the global fields. We show that local fluxes have a relatively small impact on the variability in the local column. In contrast, a substantial fraction of both the local and regional scale variability in a column arises from advection of global-scale gradients by weather systems. We describe several meteorological diagnostics that allow this variability to be quantified. In a subsequent manuscript, we will apply these diagnostics to observed $\langle CO_2 \rangle$.

3.2 Methods

We simulate CO_2 fields with a GCM, using standard surface fluxes as boundary conditions. We use the AM2 GCM developed at NOAA's Geophysical Fluid Dynamics Laboratory (Anderson et al., 2004). AM2 is a free-running GCM with prescribed sea surface temperatures. It uses a finite-volume dynamical core, which conserves mass better than a spectral model and is thus well-suited for tracer-

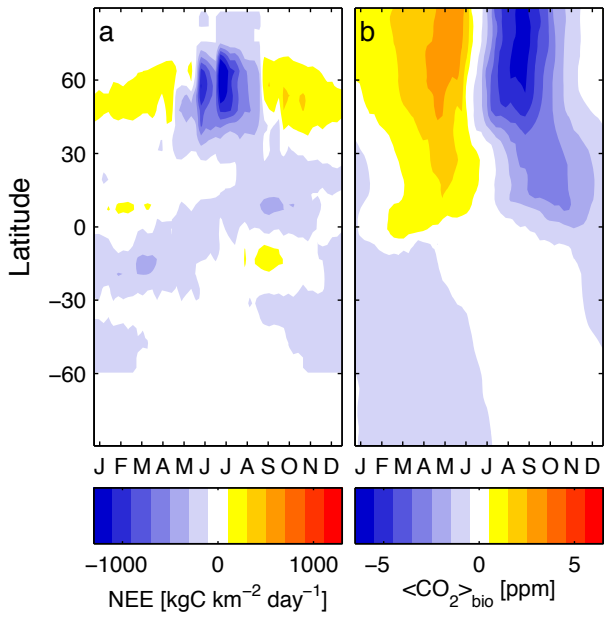

Figure 3.1: (a) Net ecosystem exchange (NEE) as a function of latitude and month of the year. Strong temporal and spatial gradients in NEE characterize the northern hemisphere. Gradients are weaker in the tropics and southern hemisphere. The resulting $\langle CO_2 \rangle_{\rm bio}$ is shown in (b). $\langle CO_2 \rangle_{\rm bio}$ has accordingly stronger spatial and temporal gradients in the northern hemisphere, and these gradients are stronger during summer than winter.

transport simulations (Lin, 2004). In multi-year runs, the total mass of the atmosphere changes by less than 1 ppm over one year. We run the model at 2° latitude by 2.5° longitude resolution with 25 vertical levels using a hybrid pressure-sigma coordinate.

Biosphere-atmosphere exchange in our simulations is based on monthly Carnegie Ames Stanford Approach (CASA) net ecosystem exchange (NEE) (Randerson et al., 1997). NEE represents the residual of monthly net primary production (NPP) and respiration fluxes that have been redistributed at 3 hour resolution based on 2001 climatology (Olsen and Randerson, 2004). The net annual exchange is approximately zero at each grid box (i.e.,'balanced' biosphere); it does not interact with AM2 climatology. Zonally integrated CASA NEE is shown in Fig. 3.1a, and the resulting biospheric $\langle CO_2 \rangle$ in Fig. 3.1b. Ocean exchange, shown in Fig. 3.2a, is based on monthly-mean fluxes derived from surface ocean pCO2 data (Takahashi et al., 2002). The ocean fluxes we use represent an annual and global mean sink of atmospheric CO_2 of ∼1.4 Pg C y^{-1}. Resulting oceanic $\langle CO_2 \rangle$ is shown in Fig. 3.2b. Fossil emissions in the model are annual mean emissions for the year 1990 (An-

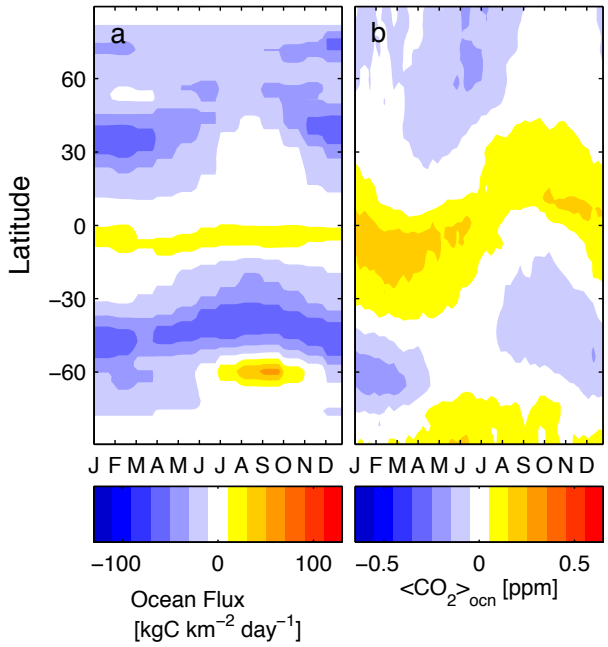

Figure 3.2: (a) Ocean exchange as a function of latitude and month of the year. The scale has been reduced by a factor of 10 compared to NEE (Fig. 3.1), as ocean fluxes are smaller. (b) $\langle CO_2 \rangle_{ocn}$ resulting from ocean exchange.

dres et al., 1996), when net global emissions were 5.5 PgC y^{-1}. These emissions are determined from self-reported fuel consumption at the national level and converted to regional fluxes proportional to local population density (Marland and Rotty, 1984).

We integrate output from the model to determine the vertically averaged dry mole mixing ratio of $\langle CO_2 \rangle$ [ppm],

$$\langle CO_2 \rangle = \frac{\int [CO_2] dp}{\int (1-q)\, dp}, \tag{3.1}$$

where p is the moist pressure, q is the specific humidity, and $[CO_2]$ is the molar mixing ratio of CO_2 in parts per million (ppm). The quantity $\langle CO_2 \rangle$ is the mass of CO_2 in a column normalized by the mass of dry air in the column and as such removes the variation due to topography. We carry separately the tracers $\langle CO_2 \rangle_{bio}$, $\langle CO_2 \rangle_{ocn}$, and $\langle CO_2 \rangle_{fossil}$ associated with CO_2 fluxes from the land biosphere, from the oceans, and from fossil fuels. We sum these three components to determine

$\langle CO_2 \rangle$.

AM2 has not been used extensively in tracer transport studies (Parrington et al., 2009). To evaluate its performance, we compare $\langle CO_2 \rangle$ fields from AM2 with $\langle CO_2 \rangle$ generated with the TM5 tracer transport model underlying CarbonTracker using identical fluxes. NOAA's CarbonTracker is a reanalysis product that uses near surface CO_2 observations to optimize flux estimates for the biosphere and the ocean. We use CarbonTracker optimized biospheric and ocean fluxes and prescribed fossil fuel and biomass burning modules to generate $\langle CO_2 \rangle$ with AM2 and compare to the CarbonTracker output (Peters et al., 2007). We find that $\langle CO_2 \rangle$ is statistically similar between the two models, and that the use of AM2 introduces no bias relative to TM5. More details are provided in the results section.

Although AM2 has relatively poor vertical resolution above the tropopause, simulated distributions of stratospheric $[CO_2]$ seem reasonable compared to available data. We compare seasonal patterns in upper tropospheric–lower stratospheric $[CO_2]$ against data obtained aboard commercial aircraft travelling between Europe and Japan (Sawa et al., 2008). Seasonal patterns (as plotted in Sawa et al. (2008), Fig. 7) are captured qualitatively by AM2, and both meridional and vertical contrasts in AM2 $[CO_2]$ are generally within $\sim$20% of the observed contrasts of up to 5 ppm across the tropopause. Given that the stratosphere only represents $\sim$15%-20% of the midlatitude atmospheric column mass, this represents sufficient agreement for our purposes.

In this chapter, we show both global $\langle CO_2 \rangle$ fields and $\langle CO_2 \rangle$ sampled from the model at locations that are part of the Total Carbon Column Observing Network (TCCON). TCCON is a network of ground-based Fourier transform spectrometers that obtain direct solar absorption spectra in the near infrared (Washenfelder et al., 2006). $\langle CO_2 \rangle$ is retrieved from these spectra, and the data are used both as validation for satellites and as independent data sets that, although spatially sparse, are temporally dense. In a subsequent chapter, we compare the model output presented here with the data from six TCCON sites (Table 3.1).

Table 3.1: TCCON sites sampled in AM2. Site acronym and location are listed, as well as the seasonal cycle amplitude (SCA) from AM2 and TM5 when CarbonTracker year 2008 fluxes underlie the two models.

Site	Lat.	Lon.	AM2 SCA (ppm)	TM5 SCA (ppm)
Bialystok, Poland	53° N	23° E	8.3	8.2
Orleans, France	48° N	2° E	6.5	7.5
Park Falls, Wisconsin, US	45° N	90° W	7.8	8.1
Lamont, Oklahoma, US	37° N	97° W	5.8	5.7
Pasadena, California, US	34° N	118° W	4.7	4.9
Lauder, New Zealand	45° S	170° E	1.0	0.7

3.3 Results

3.3.1 Sources of $\langle CO_2 \rangle$ variations

On multiyear timescales, fossil fuel emissions determine the interhemispheric $\langle CO_2 \rangle$ gradient. The impact of fossil fuel emissions on the north–south $\langle CO_2 \rangle$ gradient is seen in Fig. 3.3a, which shows a map of global $\langle CO_2 \rangle_{\text{fossil}}$, averaged over August with the global mean removed. Fossil fuel emissions occur largely in the northern hemisphere, where the bulk of the global population and land are located (Andres et al., 1996). Mean $\langle CO_2 \rangle_{\text{fossil}}$ is higher by 2 ppm in the northern hemisphere than in the southern hemisphere, with a pole-to-pole gradient of $\sim$4 ppm. Although we use 1990 fossil fuel fluxes in AM2, the observed gradient in the early 1990s may have been smaller, likely due to net uptake by the biosphere, which is ignored here (Ciais et al., 1995). On yearly timescales, not all CO_2 emitted to the atmosphere by fossil fuel burning remains airborne: approximately 40%-50% is taken up by natural oceanic or terrestrial sinks (Le Quéré et al., 2009). Inference of the strength and location of these natural sinks is the focus of many inverse studies (Gurney et al., 2002, 2004).

Within the northern hemisphere, variations in the terrestrial biospheric fluxes largely determine the patterns of $\langle CO_2 \rangle$ variability. Fig. 3.1b shows a Hovmöller diagram (Hovmöller, 1949) of $\langle CO_2 \rangle_{\text{bio}}$ resulting from the fluxes shown in Fig. 3.1a. During winter and spring, northern hemisphere $\langle CO_2 \rangle_{\text{bio}}$ decreases from north to south. The gradient is generally small (< 2 ppm) from equator to pole; it reaches a maximum in late spring of $\sim$3 ppm. At the beginning of the summer, the north–south gradient of $\langle CO_2 \rangle_{\text{bio}}$ rapidly reverses, and hemispheric mean $\langle CO_2 \rangle_{\text{bio}}$ decreases as net respiration in

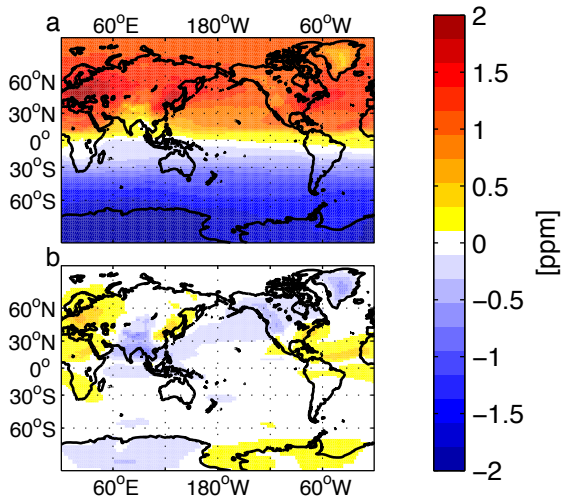

Figure 3.3: (a) August $\langle CO_2 \rangle_{fossil}$ with global mean removed. Because the bulk of emissions occurs in the north, mean $\langle CO_2 \rangle_{fossil}$ is 2 ppm higher in the northern hemisphere than in the southern hemisphere. (b) Deviation of August $\langle CO_2 \rangle_{fossil}$ from the zonal mean at each latitude. Contrasts in $\langle CO_2 \rangle_{fossil}$ between emission regions (e.g., eastern United States, Europe, and China) and upwind regions are less than 1 ppm. Overall, the meridional gradients are stronger than the zonal gradients.

the northern hemisphere transitions to net uptake. Such a signal is largely missing in the southern hemisphere as, outside the tropics, there is little landmass. The northern hemisphere shows the strongest gradients in $\langle CO_2 \rangle_{bio}$ during summer when the biosphere is most active. In August and September, meridional gradients are at least twice as large in the zonal mean than outside the growing season. Southern hemisphere $\langle CO_2 \rangle_{bio}$ is anticorrelated with northern hemisphere $\langle CO_2 \rangle_{bio}$, with low values in the northern hemisphere winter and high values in the northern hemisphere summer. The amplitude of seasonal $\langle CO_2 \rangle_{bio}$ variations is smaller throughout the southern hemisphere, and equator-pole gradients are very weak.

Fig. 3.2b shows the Hovmöller diagram for $\langle CO_2 \rangle_{ocn}$. Net ocean fluxes (Fig. 3.2a) are an order of magnitude smaller than land biosphere fluxes, and yield correspondingly smaller gradients (Fig. 3.2b) (Nevison et al., 2008). The seasonality in $\langle CO_2 \rangle_{ocn}$ is phaseshifted compared with $\langle CO_2 \rangle_{bio}$.

Local fluxes are manifest as temporal variations in $\langle CO_2 \rangle$ on short timescales. Shown in Fig. 3.4 are $\langle CO_2 \rangle_{bio}$ time series for the first two weeks of June and December. Diurnal patterns in $\langle CO_2 \rangle_{bio}$ vary among the northern hemisphere gridboxes shown: a tropical forest in southern Venezuela, a

midlatitude mixed forest near Park Falls, Wisconsin, and a boreal forest near Poker Flats, Alaska. These sites have been chosen to illustrate differences in $\langle CO_2 \rangle$ at forested sites at different latitudes within the northern hemisphere. In June, the diurnal cycle is the most notable signature in tropical $\langle CO_2 \rangle_{bio}$ (Fig. 3.4a). Carbon is taken up by photosynthesis during the day and is respired at night, producing a peak-to-trough diurnal amplitude of ∼0.5 ppm. In midlatitudes (Fig. 3.4b), the diurnally varying flux forces a peak-to-trough diurnal amplitude of ∼0.5-0.75 ppm. The diurnal cycle in $\langle CO_2 \rangle_{bio}$ at the high latitude site is less clear during the summer growing season (Fig. 3.4c). Due to the long day and short night at high latitudes, photosynthetic uptake of carbon occurs over a greater fraction of the day. Outside the tropics, carbon taken up during the day is not in close balance with carbon respired, and a larger net drawdown is evident at high latitudes and midlatitudes over this two-week period. The diurnal cycle is similar in both winter and summer in the tropics because the biosphere experiences neither seasonal temperature nor sunlight limitation (Fig. 3.4d). At middle and high latitues, little or no diurnal signal is present during the winter, because respiration dominates total NEE both day and night (Fig. 3.4e-f). Rather, the variations in these time series occur on multiday timescales, with changes in $\langle CO_2 \rangle_{bio}$ of order 1 ppm.

Even during the middle of the growing season, only a small fraction of the variation in middle and high latitude $\langle CO_2 \rangle_{bio}$ is due to local fluxes. Fig. 3.5 shows the relationship between flux and CO_2 in the column at the midlatitude gridbox (Park Falls) for June. In Fig. 3.5, the difference in CO_2 between the time with maximum concentration (∼8:00 local time) and minimum concentration (∼15:00 local time) is plotted against the integrated flux for this seven-hour period. The change in $\langle CO_2 \rangle_{bio}$ shows a positive correlation with flux: greater uptake by the biosphere leads to drawdown in the column. The solid line in Fig. 3.5 represents the change expected in the column due to flux alone in the absence of horizontal transport. The dashed line in Fig. 3.5 represents the least squares fit to the data. It accounts for only 12% of the variance. Simulations that include only biospheric exchange for the gridboxes neighboring Park Falls confirm the small influence of local fluxes; the diurnal cycle at the peak of the growing season is 0.5-0.7 ppm, and local fluxes account for 20% of the variance in $\langle CO_2 \rangle$ during the day, confirming that even on short time scales, other factors are

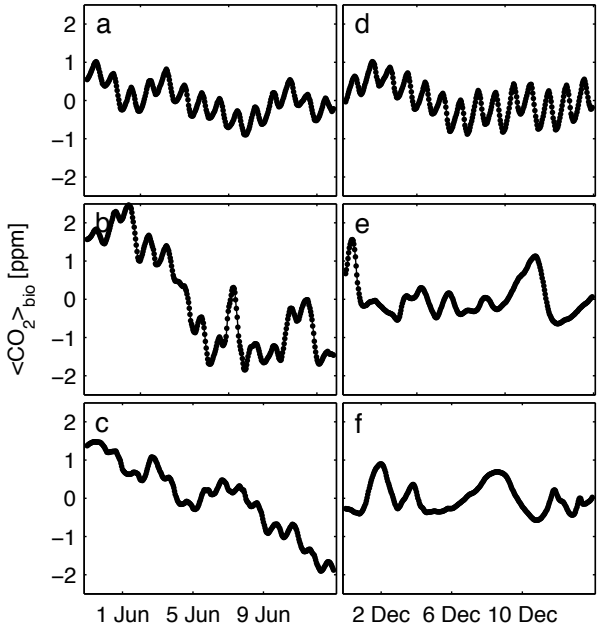

Figure 3.4: Biospheric $\langle CO_2 \rangle_{bio}$ sampled at three northern hemisphere gridboxes in June (left) and December (right). (a, d) Tropical Venezuela (3° N, 295° E). (b, e) Midlatitude (46° N, 270° E). (c, f) High latitude Alaska (65° N, 213° E). A diurnal cycle is evident at all sites during the summer, but it is dwarfed by synoptic-scale variability in mid- and high-latitudes. During the winter, only the tropical site shows a diurnal cycle in $\langle CO_2 \rangle_{bio}$.

more important for $\langle CO_2 \rangle_{bio}$ variability. Flux estimation from column data is complicated by the large footprint of sources and sinks affecting $\langle CO_2 \rangle$. At 500 hPa, the center of mass of the column, westerly winds in the midlatitudes average 8.5 m s^{-1} during June. Thus, over the seven-hour period used to calculate $\Delta\langle CO_2 \rangle_{bio}$ in Fig. 3.5, the column is influenced by air originating more than 200 km upstream. Without spatial gradients in $\langle CO_2 \rangle$, this advection would have a much less pronounced influence on variability. In the presence of regional gradients, however, transport induces substantial temporal variability in $\langle CO_2 \rangle$. A simulation with labeled CO_2 from local NEE shows that the the diurnal cycle due to local fluxes is between 0.5 and 0.75 ppm, and that intraday differences in June are quite small (less than 0.1 ppm).

Regional fluxes can have a persistent effect on the column. The large-scale influence of regional fluxes is demonstrated through a relatively simple example: seasonally stationary fossil fuel emis-

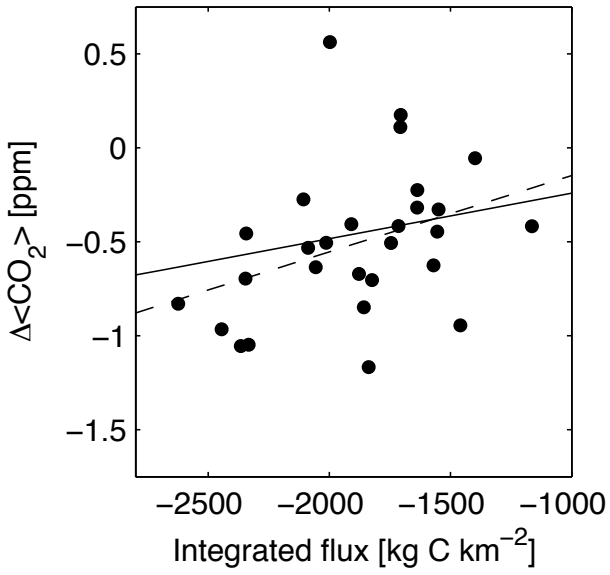

Figure 3.5: Relationship between daytime $\Delta\langle CO_2\rangle_{\rm bio}$ (15:00 minus 8:00) and daytime NEE at the gridbox corresponding to Park Falls, Wisconsin in June. The dashed line represents the best fit to the data, but it accounts for only 13% of the variance (as determined by R^2). The solid line represents the change expected in $\langle CO_2\rangle$ due to the surface flux alone.

sions. Because fossil fuel fluxes are somewhat localized and steady (i.e., of one sign), $\langle CO_2\rangle_{\rm fossil}$ has a distinct regional signature. In Fig. 3.3b, we remove the zonal mean at each latitude to reveal these regional signatures. There is contrast in $\langle CO_2\rangle_{\rm fossil}$ between emission regions, such as Europe and East Asia, and their upwind counterparts. The mean residence time of fossil CO_2 within $\sim 30^\circ$ longitude of emission is only 3-4 days, so these zonal gradients do not exceed 0.5 ppm even when the flux is rather large (e.g., Eastern U.S.). The regional signature of fossil fuel fluxes is, however, proportional to the strength of the flux as expected for the linearity of passive tracer advection; in simulations with doubled fossil fuel emissions, the regional contrasts also double.

In the northern hemisphere, spatial gradients in $\langle CO_2\rangle$ are largely determined by the land biosphere fluxes. Unlike for the fossil fuel emissions, biospheric fluxes are sufficiently diffuse that even in the middle of the growing season, the regional pattern of $\langle CO_2\rangle$ has little to do with the regional biospheric fluxes. Rather, the pattern in $\langle CO_2\rangle$ reflects the north–south gradient in the fluxes acted upon by the large-scale dynamics. To illustrate, we redistribute the standard CASA fluxes (shown for August in Fig. 3.6a) uniformly around latitude bands (Fig. 3.6b). Thus, both simulations have

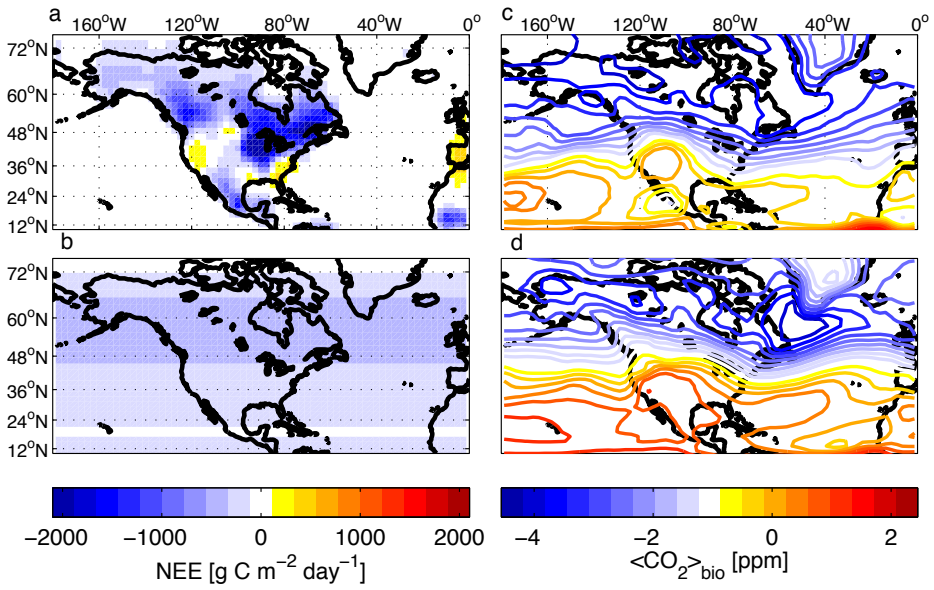

Figure 3.6: (a) August-mean NEE from the CASA model. Fluxes over the ocean are zero, and land fluxes are generally negative, indicating uptake of carbon by the terrestrial biosphere. (b) Zonal mean August NEE. Fluxes over land and ocean at a given latitude are the same, and there are only weak north–south gradients in fluxes over the northern hemisphere. Nonetheless, gradients in $\langle CO_2 \rangle_{bio}$ are similar for both distributions of underlying surface fluxes (c and d).

the same north–south flux gradient in the zonal mean. The resulting August-mean $\langle CO_2 \rangle$ distributions are shown in Fig. 3.6c and 3.6d. The patterns of $\langle CO_2 \rangle$ variability in the two simulations are quite similar; averaged over August, fewer than 50% of northern hemisphere gridboxes show a difference greater than 1 ppm between the simulations with CASA fluxes and those with zonally uniform fluxes, and fewer than 10% show a difference greater than 2 ppm (Fig. 3.7). The pattern of $\langle CO_2 \rangle$, even over the center of the growing region of North America, is largely a manifestation of the north–south gradient in the *zonally averaged* flux. Local maxima (e.g., southern California) and minima (e.g., midwestern U.S.) in the CASA simulations do not reflect the strength of the underlying sources and sinks but result from the interaction of climatological stationary waves and the large-scale north–south differences in biospheric carbon uptake.

The north–south distribution of surface fluxes also dominates the seasonal variations in $\langle CO_2 \rangle$. We calculate the peak-to-trough seasonal cycle amplitude in $\langle CO_2 \rangle$ to estimate temporal variations

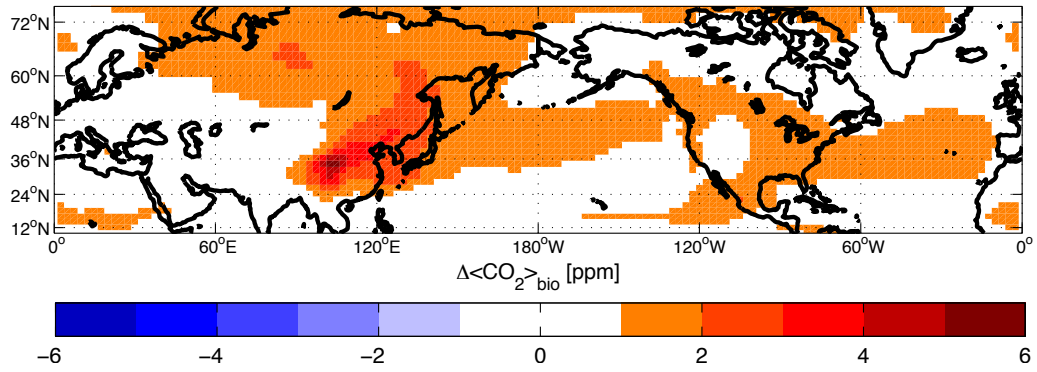

Figure 3.7: $\Delta\langle CO_2\rangle_{\rm bio}$ is generally smaller than 2 ppm and exhibits a positive anomaly downwind of land uptake regions. Northern hemispheric summer CO_2 increases by $\sim$0.1% in the simulation with zonal fluxes compared to the simulation with CASA fluxes.

at five northern hemisphere TCCON sites. The northern hemisphere $\langle CO_2\rangle$ time series have been detrended by subtracting the southern hemisphere $\langle CO_2\rangle$ trend from the gridbox corresponding to Lauder, New Zealand. The seasonal cycle amplitude (the difference between the maximum and minimum of the monthly mean $\langle CO_2\rangle$) changes little when zonally averaged biospheric fluxes are used. The seasonal cycle amplitude at the gridbox corresponding to Park Falls, for example, is reduced by less than 20% in simulations with zonal fluxes rather than CASA fluxes. The seasonal cycle amplitudes at other midlatitude sites change by less than 15%, and at the subtropical sites, by less than 5%, when zonally symmetric biospheric fluxes are used. To further test the response of the seasonal cycle amplitude to perturbations in surface fluxes, we uniformly scale NEE across the northern hemisphere by factors between one and two. Fig. 3.8a shows that the seasonal cycle amplitudes at all five TCCON sites scale linearly with NEE.

To probe the signature of a regional flux increase on $\langle CO_2\rangle_{\rm bio}$ at various latitudes, we amplify NEE in 10° latitude bands. We scale NEE in each band by an amount that increases northern hemisphere NPP by 25% (Table 3.2). Because NEE in our model is the residual of NPP and respiration at three-hourly intervals, a uniform increase in NPP increases NEE at high latitudes, where there is a large seasonality in NEE, but has little effect at low latitudes where NPP is in balance with respiration on short time scales. Fig. 3.9 shows the relative increase of the seasonal cycle amplitude in $\langle CO_2\rangle_{\rm bio}$ at northern hemisphere TCCON sites as a function of the latitude of

Table 3.2: Scale factors used to increase northern hemisphere net primary productivity (NPP) by 25% in CASA.

Latitude range	Annual NPP [Pg C]	Weighting factor	% Increase to NEE
15–20°	1.66	4.25	5
20–30°	3.08	2.80	3
30–40°	4.10	2.30	3
40–50°	5.63	1.95	10
50–60°	4.78	2.15	41
60–70°	2.21	3.45	98

amplification. In general, the seasonal cycle amplitude increases as fluxes are amplified further north, due to the greater seasonality of NEE at higher latitudes. Except for Pasadena, California (34°N), the sites show little sensitivity to an increase in subtropical fluxes. Although Pasadena shows the largest response among all sites to flux amplification south of 30°N, its seasonal cycle amplitude changes more (30% compared to 15%) when fluxes are amplified north of 50°. Lamont, Oklahoma, which also sits on the edge of the subtropics (36°N), shows a step function increase in seasonal cycle amplitude as enhanced exchange moves north of the subtropical jet: the seasonal cycle amplitude is essentially unaffected by changes in flux south of 30°, but it increases by a uniform 30% when fluxes are enhanced north of 40°. The seasonal cycle amplitude at Park Falls, located in the center of a biospherically active region (46°N), peaks when amplification impacts local fluxes between 40° and 50°. However, the seasonal cycle amplitude at European sites (48° and 53°N) increase monotonically as fluxes increase to their north. These diverse responses highlight the sensitivity of the seasonal cycle amplitude to remote fluxes. Enhancing the seasonal cycle in NEE at high latitudes has a significant impact on the atmospheric signal thousands of kilometers away. These results, together with the fact that seasonal cycle amplitude scales linearly with total northern hemisphere fluxes, confirm that hemispheric-scale fluxes determine the seasonal cycle amplitude in the column (Yang et al., 2007).

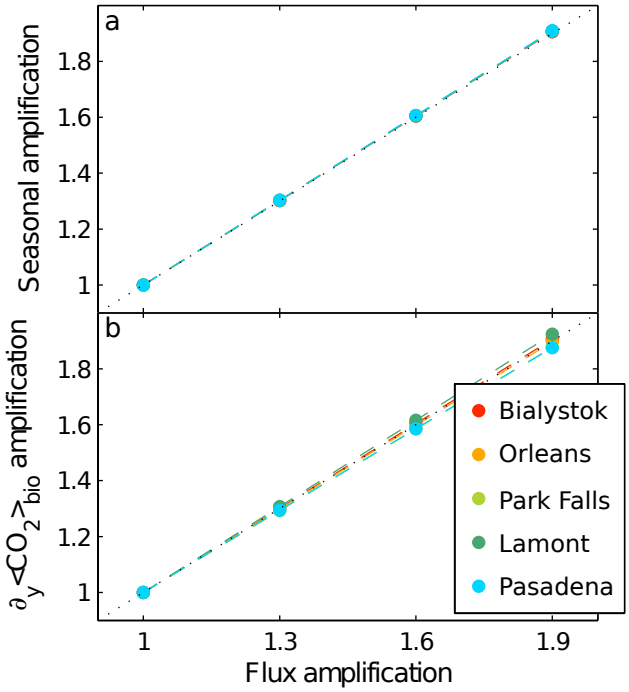

Figure 3.8: (a) Amplification to the seasonal cycle amplitude in simulations with amplified NEE versus CASA NEE. Scaling NEE throughout the northern hemisphere increases the seasonal cycle amplitude proportionally at each of five northern hemisphere TCCON sites. (b) Amplification to the estimated gradients in simulations with amplified NEE versus CASA NEE. The estimated $\langle CO_2 \rangle_{bio}$ gradient, $\partial_y \langle \widehat{CO_2} \rangle_{bio}$, also increases proportionally at each of the TCCON sites. The unit diagonal is plotted in each panel. Site acronyms are defined in Table 3.1.

3.3.2 Synoptic-scale variations and relation to gradients

Synoptic variations in $\langle CO_2 \rangle$ are intimately tied to the large-scale gradients. Because $\langle CO_2 \rangle$ fields are strongly influenced by the interaction between fluxes and large-scale dynamics, we use a dynamic coordinate to diagnose the influence of synoptic activity. We analyze the relationship between meridional gradients in $\langle CO_2 \rangle$ and synoptic scale variability by using an empirical relationship between variations in $\langle CO_2 \rangle$ and variations in potential temperature, θ, which acts as a dynamical tracer of the latitude of origin of airmasses because θ is conserved following adiabatic flow. Near the surface, such flow is largely horizontal because vertical motion is inhibited. Latent heat release and boundary layer turbulence, however, can cause deviations from adiabaticity on large scales. We therefore choose θ near the surface but above the boundary layer, at 700 hPa, to define a meridional

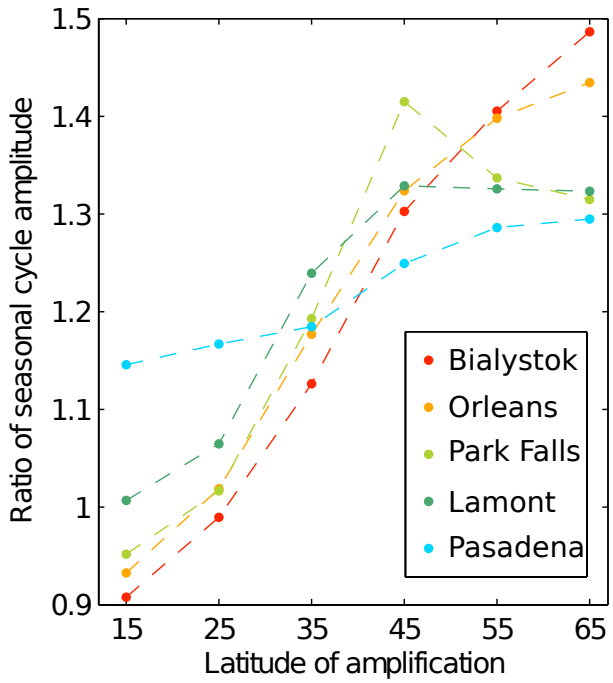

Figure 3.9: Amplification in $\langle CO_2 \rangle_{bio}$ seasonal cycle amplitude when NEE is enhanced in 10° latitude bands relative to CASA NEE. The seasonal cycle amplitude from simulations with enhanced NEE is normalized by the corresponding seasonal cycle amplitude resulting from CASA fluxes. The seasonal cycle amplitude is more sensitive to flux enhancements in boreal ecosystems, due to the greater seasonality of NEE.

displacement scale,

$$L = \frac{\theta' - \overline{\theta}_0}{\partial_y \overline{\theta}}, \tag{3.2}$$

where θ' is the local potential temperature band-pass filtered to remove low-frequency (greater than 21 days) and high-frequency variability (less than three days), thus isolating synoptic variations. The reference value $\overline{\theta_0}$ represents monthly mean θ at a reference location (by default, the local gridbox). The gradient $\partial_y \overline{\theta}$ represents the monthly mean meridional gradient in θ smoothed by a radial Gaussian filter with standard deviation of 1500 km. The displacement scale L has units of length and can be interpreted as the mean meridional distance from the reference latitude from which an adiabatically transported air parcel originates. We can then infer an estimate of the $\langle CO_2 \rangle$ gradient using variations in $\langle CO_2 \rangle$:

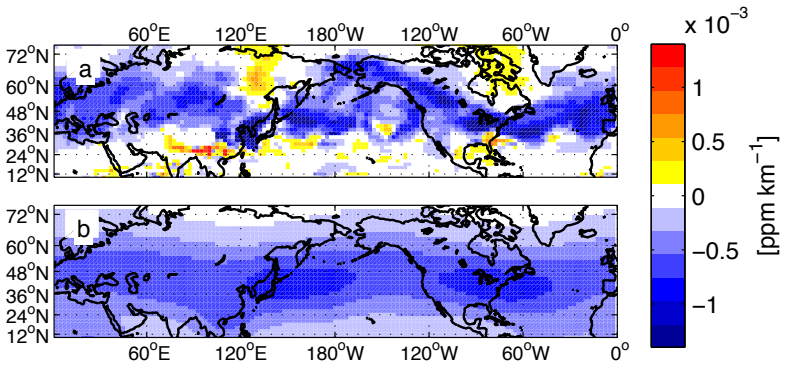

Figure 3.10: August gradients in simulated $\langle CO_2 \rangle$. (a) Estimated gradient $\partial_y \widehat{\langle CO_2 \rangle}$ calculated at each gridbox from variations in $\langle CO_2 \rangle$ and θ. (b) Actual meridional gradient in $\langle CO_2 \rangle$ smoothed over 1500 km.

$$\partial_y \widehat{\langle CO_2 \rangle} = \frac{\langle CO_2 \rangle'}{L}. \tag{3.3}$$

Here, $\langle CO_2 \rangle'$ represents the 3–21 day band-pass filtered $\langle CO_2 \rangle$. The band-pass filtering isolates the synoptic variations that are well resolved in GCMs. It makes it possible to compare our results with actual data, in which small-scale, high-frequency variations that may not be well resolved in GCMs also contribute to fluctuations, particularly of passive tracers such as CO_2, which have a relatively flat spectrum as a function of length scale.

The gradient estimated from variations in $\langle CO_2 \rangle$, $\partial_y \widehat{\langle CO_2 \rangle}$, approximates the north–south gradient in the midlatitudes. In Fig. 3.10a, we plot the August $\langle CO_2 \rangle$ gradient estimated using equation 3.3, while in Fig. 3.10b, we plot the gradient obtained directly from AM2 $\langle CO_2 \rangle$, smoothed using the 1500 km radial filter. Thus, covariations in observed $\langle CO_2 \rangle$ and θ can be used to infer the large-scale north–south gradient in $\langle CO_2 \rangle$, provided that data are obtained in a region with sufficient synoptic-scale turbulent activity (i.e., in midlatitudes). Outside the midlatitudes, Fig. 3.10 suggests that the method does not provide an accurate estimate of the large scale gradient as θ gradients are relatively small and eddy activity is weaker.

The large-scale north–south gradient can thus be constrained from variations within a single time series. We estimate the mean 30°-60°N $\langle CO_2 \rangle$ contrast over North America in AM2 using equation

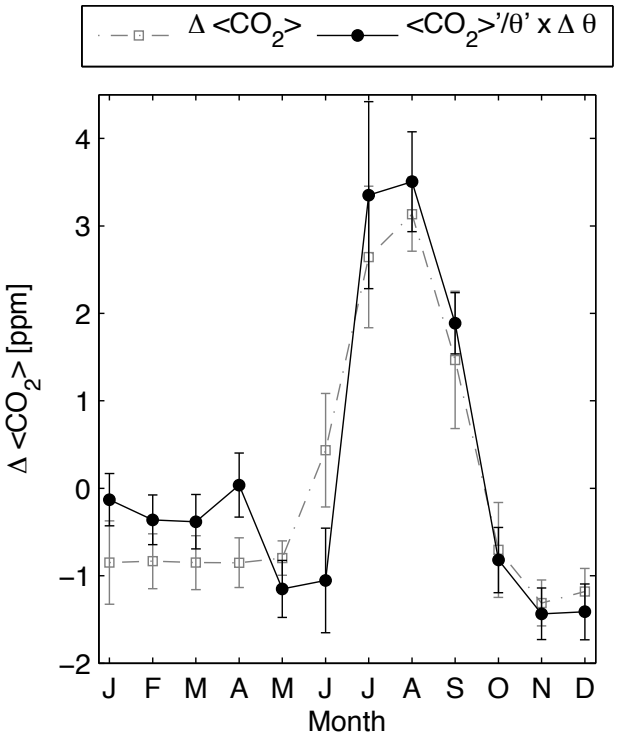

Figure 3.11: $\langle CO_2 \rangle$ contrast between 30 and 60°N over North America (averaged between 180 and 300°W). The gray squares are the actual contrast, while the black circles are the contrast calculated from variations in $\langle CO_2 \rangle$ and θ.

3.3 with $\langle CO_2 \rangle'$ sampled at the gridbox corresponding to Park Falls and with the displacement L determined from the potential temperature contrast between 30°N and 60°N (equation 3.2). Fig. 3.11 compares the thus estimated $\langle CO_2 \rangle$ contrast to the contrast determined from taking the difference in $\langle CO_2 \rangle$ averaged over 180°-300°W at 30° and 60°. The two methods of determining the $\langle CO_2 \rangle$ contrast are in good agreement across seasons, confirming that quantitative information about the large-scale gradient is contained in synoptic variations at a single midlatitude site.

Fig. 3.12 shows that the correlation between variations in $\langle CO_2 \rangle$ and variations in θ reflects meridional gradients in $\langle CO_2 \rangle$ at northern hemisphere TCCON sites. Fig. 3.12a shows the seasonal cycle in $\langle CO_2 \rangle$ for five TCCON sites in a simulation forced by zonal biospheric fluxes. The seasonal cycle amplitude is greater in midlatitudes than in the subtropics, and the summer minima in $\langle CO_2 \rangle$ are earlier. During the summer, the $\langle CO_2 \rangle$ contrast among sites grows, and the contrast decreases in winter. The dynamical connection between the sites is seen in the lower panels, where daily $\langle CO_2 \rangle'$

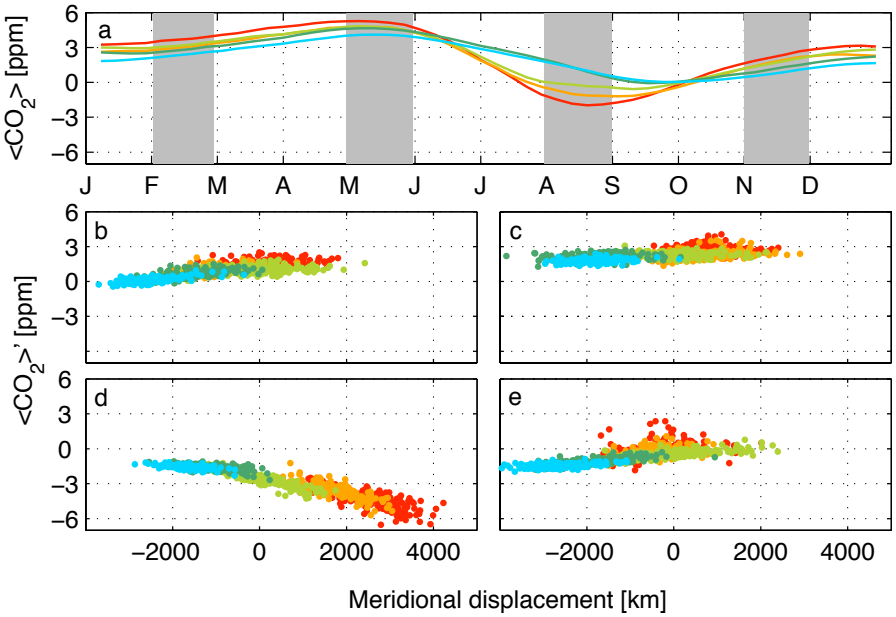

Figure 3.12: (a) Detrended $\langle CO_2 \rangle$ for each of five TCCON sites sampled in AM2 driven by zonal-mean NEE. The data at each site have been detrended based on annual mean southern hemisphere data. Shaded regions represent the months plotted in panels b-e, which show band-pass filtered $\langle CO_2 \rangle$ plotted against the meridional displacement relative to Park Falls (46°N), for four months: (b) February (c) May (d) August (e) November. Colors are the same as Fig. 3.8 and 3.9.

in February, May, August, and November (corresponding to shaded periods in Fig. 3.12a) is plotted against the meridional displacement relative to Park Falls (i.e., $\overline{\theta_0}$ in equation 3.2 represents the monthly mean θ at the gridbox corresponding to Park Falls rather than at the local gridbox). A negative displacement represents southerly origin while a positive displacement represents northerly origin.

The range of $\langle CO_2 \rangle'$ in Fig. 3.12b-e reflects the gradient in $\langle CO_2 \rangle$ at the sites. In general, outside the growing season, the $\langle CO_2 \rangle$ gradient is positive (higher to the north). During May, the gradient is essentially flat as the north–south $\langle CO_2 \rangle$ gradient reverses at the growing season onset at high latitudes (Fig. 3.1b). August data is plotted in Fig. 3.12d. During summer, the total $\langle CO_2 \rangle'$ range is largest and the $\langle CO_2 \rangle$ gradient is negative because northern $\langle CO_2 \rangle$ has been drawn down by the biosphere. Fig. 3.12b-e demonstrate how transport mixes $\langle CO_2 \rangle$ among the sites: there is a substantial overlap of $\langle CO_2 \rangle$ sampled at different sites along the meridional displacement curve.

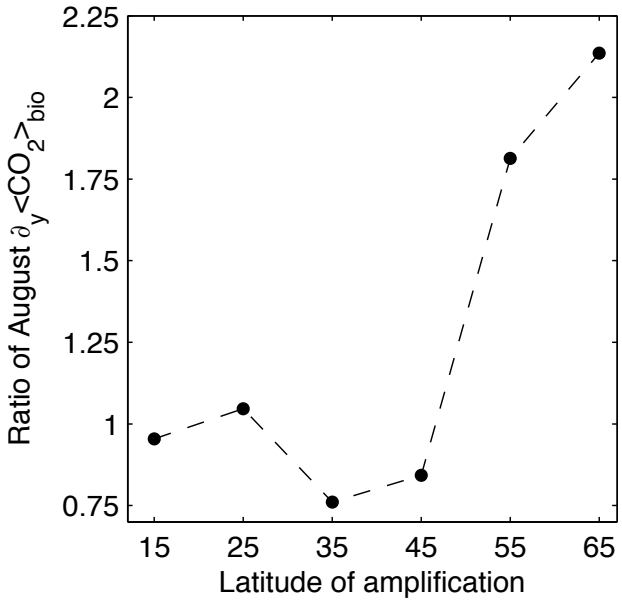

Figure 3.13: August $\partial_y \widehat{\langle \mathrm{CO_2} \rangle}_{\mathrm{bio}}$ estimated at Park Falls, Wisconsin as NEE is amplified in the 10° bands shown in Table 3.2. The estimated gradient remains essentially the same when fluxes are amplified to the south of the site, whereas the gradient doubles when fluxes are amplified north of the site. Enhancing NEE north of the site draws down $\langle \mathrm{CO_2} \rangle$ during August, leading to a larger north–south gradient.

3.3.3 Relationship between synoptic scale variability and flux

Like the seasonal cycle amplitude, $\partial_y \widehat{\langle \mathrm{CO_2} \rangle}$ scales linearly with fluxes, and therefore linearly with the north–south gradient in the midlatitudes. Fig. 3.8b shows the ratio of $\partial_y \widehat{\langle \mathrm{CO_2} \rangle}_{\mathrm{bio}}$ for simulations with northern hemisphere amplified fluxes relative to CASA fluxes. With NEE amplified over a range of latitudes, $\partial_y \widehat{\langle \mathrm{CO_2} \rangle}_{\mathrm{bio}}$ responds differently to amplification north or south of the storm track. Figure 3.13 shows $\partial_y \widehat{\langle \mathrm{CO_2} \rangle}_{\mathrm{bio}}$ at Park Falls for simulations with amplified NEE relative to those with CASA NEE. When flux amplification occurs between 10° and 50°, $\partial_y \widehat{\langle \mathrm{CO_2} \rangle}_{\mathrm{bio}}$ changes little. When flux amplification occurs north of 50°, however, the estimated gradient essentially doubles.

Diagnostics such as the seasonal cycle amplitude and $\partial_y \widehat{\langle \mathrm{CO_2} \rangle}$ provide information about the large-scale distribution of the fluxes. We can also use them to attribute regional fluxes. Fig. 3.14a shows the seasonal cycle for $\langle \mathrm{CO_2} \rangle$ at northern hemisphere TCCON sites in a simulation with CASA biospheric fluxes. May and August $\langle \mathrm{CO_2} \rangle'$ from this simulation are plotted against meridional

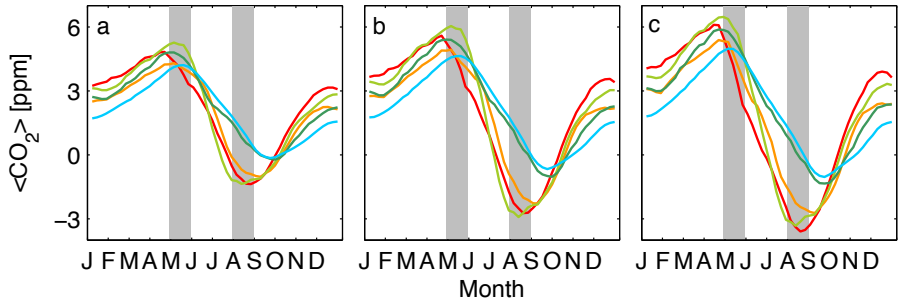

Figure 3.14: Detrended $\langle CO_2 \rangle$ at TCCON sites in three simulations with different surface fluxes. (a) CASA fluxes. (b) Boreal fluxes enhanced. (c) Boreal fluxes enhanced with early onset of the growing season. When boreal fluxes are increased, the seasonal cycle amplitude increases. When the length of the growing season increases, the seasonal cycle amplitudes increase further despite no increase in net exchange between (b) and (c). Colors are the same as Fig. 3.8. Daily data from the shaded periods (May and August) are plotted in Fig. 3.15.

displacement relative to Park Falls in Fig. 3.15a. The TCCON sites do not fall along a smooth curve, as they did when zonal biospheric fluxes were used (Fig. 3.12c,d). During May, $\langle CO_2 \rangle$ sampled at the European sites is slightly lower than at North American sites due to earlier onset of the growing season, evident in the Fig. 3.14a time series. During August, the data sampled at Park Falls are offset about 2 ppm compared to the European sites, and compared to the simulation with zonal fluxes. Part of this offset ($\sim$0.5 ppm) is due to persistent influence of regional fossil emissions (Fig. 3.3b), and $\sim$1.5 ppm is due to the regional biospheric drawdown in Park Falls (Fig. 3.7). These regional differences are not simply confined to the boundary layer, but also exist in the lower troposphere. At the three midlatitude TCCON sites, between 20% and 40% of the summer variability in Fig. 3.15a is explained by variability in the meridional displacement (as measured by the R^2 value). This fraction is smaller in the subtropics (15%–20% during the summer). During the winter months (not shown), total variability decreases, but the fraction explained by the meridional displacement is still $\sim$20% in the midlatitudes, and increases to 40%–50% in the subtropics.

We present two sensitivity studies to demonstrate further the response of these diagnostics to regional changes in flux. In the first study, we amplify boreal exchange. In the second, we lengthen the boreal growing season. Based on a comparison of the seasonal cycle amplitude of $\langle CO_2 \rangle$ observed at Park Falls with modeled $\langle CO_2 \rangle$, Yang et al. (2007) suggest that the northern hemisphere NEE

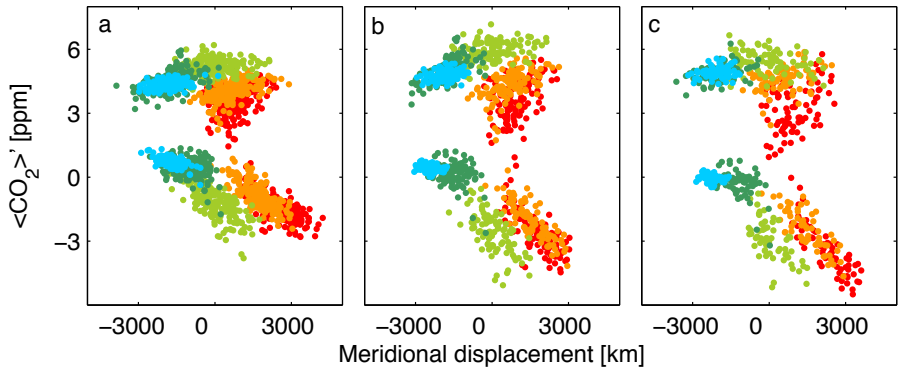

Figure 3.15: Northern hemisphere TCCON $\langle CO_2 \rangle'$ plotted against meridional displacement (relative to Park Falls) for three simulations with perturbed surface fluxes. In each panel, the top cloud of points shows May data while the lower cloud of points shows August data. (a) CASA fluxes. (b) Boreal fluxes enhanced. (c) Boreal fluxes enhanced with early onset of the growing season.

is underestimated by ∼30%. Given that the midlatitude seasonal cycle amplitude is insensitive to NEE amplification in the tropics (Fig. 3.9), we enhance boreal fluxes by 50% between 45° and 65° to increase hemispheric NEE by 30%. We plot the time traces in $\langle CO_2 \rangle$ sampled at TCCON sites in Fig. 3.14b. The seasonal cycle amplitudes of the northern sites increase by ∼25% and the gradient among the northern hemisphere sites grows during the summer (by ∼60% in Fig. 3.15b compared with Fig. 3.15a). The early drawdown in Europe in May is even more obvious when the northern uptake is greater (Fig. 3.15b) and the range of $\langle CO_2 \rangle'$ increases during August.

The phasing of the growing season onset also is apparent in our diagnostics. Numerous studies have suggested that earlier spring warming leads to early onset of net flux into the ecosystem (Piao et al., 2008). We hasten the onset of the growing season in the simulation with enhanced boreal NEE between 50 ° and 60°N by one month. We add July NEE to May NEE (turning a net source into a net sink), and increase respiration across non-summer months (September to March) so that NEE is balanced annually. A time series of NEE for a representative location in boreal North America is shown in Fig. 3.16. With earlier onset of the growing season, the maximum $\langle CO_2 \rangle$ occurs at Bialystok three weeks earlier in spring, while the phasing of $\langle CO_2 \rangle$ at other sites is unaffected (Fig. 3.14c). The net effect of a longer growing season is stronger north–south gradients during the early summer and lower summer minima in $\langle CO_2 \rangle$ at the European sites such that the TCCON sites

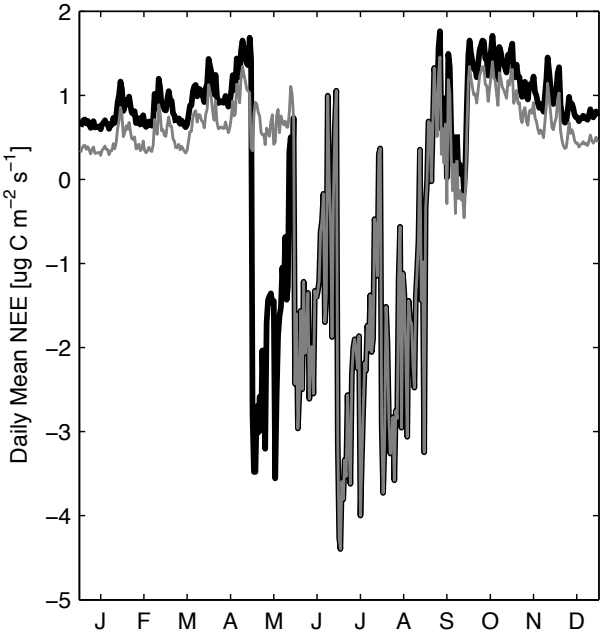

Figure 3.16: Daily mean NEE at 270°W, 60°N for boreal-enhanced CASA fluxes (gray) and long boreal growing season (black). July NEE has been added to May to hasten the onset of the growing season in spring, and the net flux of carbon to the atmosphere is increased outside the growing season to balance the fluxes

more clearly fall along a single $\langle CO_2 \rangle'$-L curve for August in this scenario (Fig. 3.15c).

3.3.4 Effect of model transport errors

A further illustration of the role of large-scale flux patterns in determining the pattern in $\langle CO_2 \rangle$ is the small sensitivity of the fields to vertical mixing. We alter the vertical layer where carbon exchange in the model occurs. CASA biospheric fluxes were imposed at three different levels in the model, corresponding to the surface, ∼800 hPa and ∼700 hPa, the latter being well in the free troposphere.

Overall, vertical mixing has a small effect on the mass gradient in $\langle CO_2 \rangle$. Fig. 3.17 shows the difference in the monthly mean 30–60°N $\langle CO_2 \rangle_{\rm bio}$ contrast over North America between simulations with elevated and surface exchange. When surface exchange occurs at 800 or 700 hPa, the $\langle CO_2 \rangle_{\rm bio}$ gradient induced by improper vertical mixing is less than 0.2 ppm at all seasons. The fact that

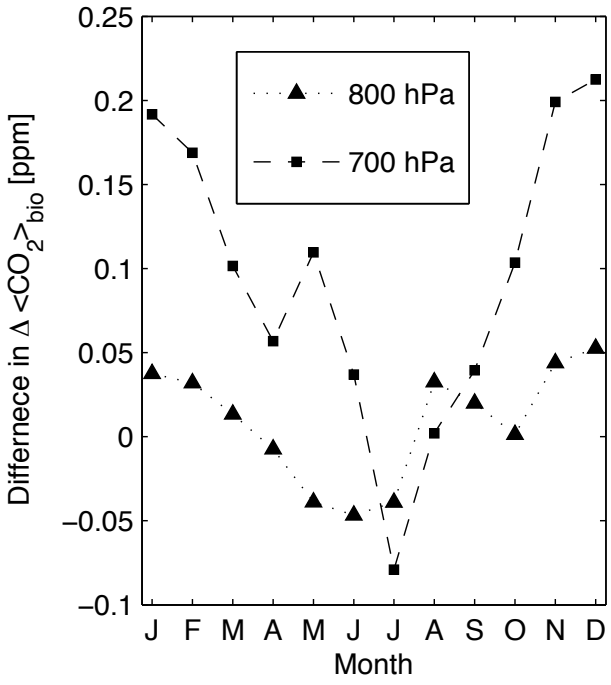

Figure 3.17: Difference in the 30°-60°N $\langle CO_2 \rangle_{bio}$ contrast, averaged over North America (180°-300°W) when fluxes are emitted at two levels in AM2 versus at the surface.

$\langle CO_2 \rangle$ is a mass constraint and that the footprint is inherently larger means that local fluxes and sub-gridscale physics have minimal influence on gradients. Even with a gross error in vertical mixing, the large-scale diagnostics in $\langle CO_2 \rangle$ change little. Fig. 3.18 shows a difference map between the $\langle CO_2 \rangle_{bio}$ from simulations with exchange at 700 hPa and exchange at the surface during August (top) and February (bottom). Except over the Tibetan Plateau in summer, mean $\langle CO_2 \rangle_{bio}$ changes by less than 0.75 ppm everywhere.

Although, in general, fluxes covary with meteorological variables such as temperature and boundary layer height, small-scale physics has little influence on the ultimate diagnostics, such as seasonal cycle amplitude or the estimated $\partial_y \widehat{\langle CO_2 \rangle}$. This is illustrated in a comparison of $\langle CO_2 \rangle$ diagnostics at TCCON sites between AM2 and CarbonTracker, both run with the same fluxes. CarbonTracker uses reanalysis meteorology, so there are correlations between the fluxes and the dynamics, whereas in AM2, the fluxes and meteorology are independent. Both models yield similar seasonal cycle amplitudes (Table 3.1) and estimates for seasonal $\partial_y \widehat{\langle CO_2 \rangle}$ (Fig. 3.19) despite very different mete-

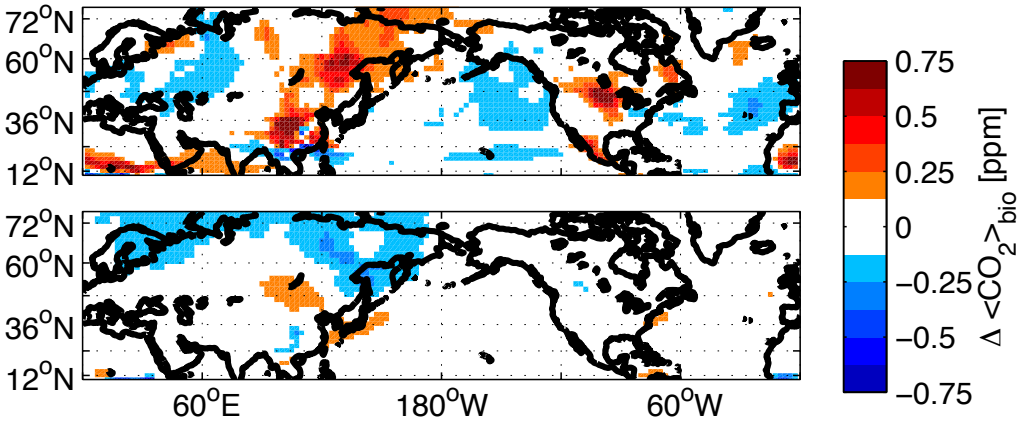

Figure 3.18: (a) Difference in August-mean $\langle CO_2 \rangle_{bio}$ between simulations in which CASA fluxes are located above the boundary layer at 700 hPa versus at the surface. (b) same, except for February-mean $\langle CO_2 \rangle_{bio}$.

orology. Such results suggest that analysis of $\langle CO_2 \rangle$ using a dynamical coordinate such as θ may help mediate differences between models.

Despite these encouraging results, studies have shown that the inversion of simulated $\langle CO_2 \rangle$ is sensitive to model-specific transport (Chevallier et al., 2010). The extent to which transport errors are aliased into errors in the optimized fluxes is, however, quite sensitive to the spatial covariance structures specified in the inversion setup. The discussion in this chapter of the footprint of $\langle CO_2 \rangle$ may help to inform the design of spatial covariance structures used in future inversions of $\langle CO_2 \rangle$.

3.4 Conclusions

Column-averaged $\langle CO_2 \rangle$ has a very large footprint. As such, variations in $\langle CO_2 \rangle$ are primarily determined by large-scale phenomena. Advection of large-scale $\langle CO_2 \rangle$ gradients on synoptic timescales dwarfs diurnal variations in all seasons. These gradients are set primarily by the north–south flux distribution. One implication of this finding is that analyses of $\langle CO_2 \rangle$ for flux constraints must use a global domain. Differences in $\langle CO_2 \rangle$ due to regional fluxes will be revealed only after the large-scale forcing is accounted for.

At midlatitude TCCON sites, much of the variability in $\langle CO_2 \rangle$ is tied to synoptic variability

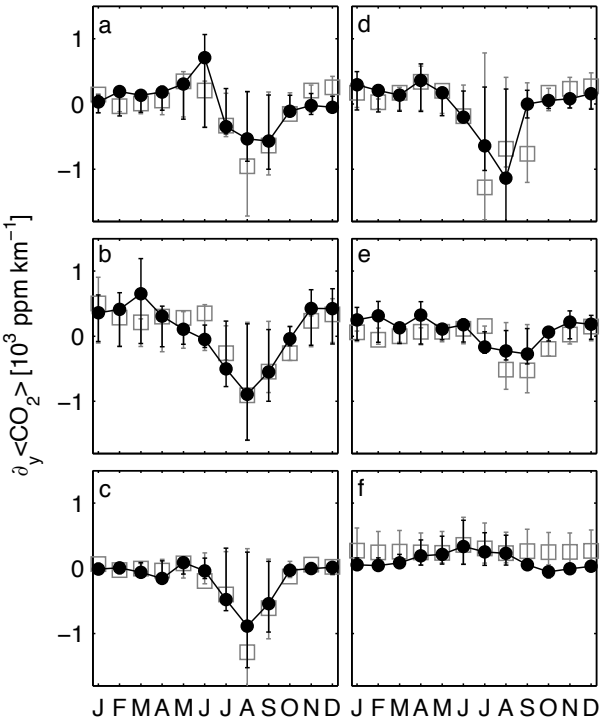

Figure 3.19: Estimated $\partial_y \widehat{\langle CO_2 \rangle}$ at six TCCON sites in AM2 (black circles) and in TM5 (gray squares) using identical surface fluxes. (a) Bialystok, Poland (b) Orleans, France (c) Park Falls, USA (d) Lamont, USA (e) Pasadena, USA (f) Lauder, New Zealand. The estimated gradients generally agree when the two models are driven with identical surface fluxes despite different meteorology.

acting on large-scale gradients rather than to underlying fluxes. This fact complicates interpretation of sparse measurements without considering the larger domain. Accurate description of the mean state, however, does allow regional flux information to emerge. For example, in simulations with CASA fluxes, $\langle CO_2 \rangle$ from Bialystok is low in May relative to other sites when plotted as a function of meridional displacement (Fig. 3.15a) due to earlier regional onset of the growing season. In contrast, the Bialystok $\langle CO_2 \rangle$ from a simulation driven by zonal biospheric fluxes fall along a smooth curve with the other sites (Fig. 3.12c). Likewise, regional drawdown is evident in Park Falls in the experiment with CASA fluxes (Fig. 3.15a), where Park Falls $\langle CO_2 \rangle$ is $\sim$1.5 ppm lower than in the zonally uniform flux experiment (Fig. 3.12c) during August, in agreement with the $\langle CO_2 \rangle$ difference at Park Falls in Fig. 3.7. Comparisons such as these provide quantitative information on the regional flux phasing and strength, even in the context of large-scale gradients.

The relative contribution of regional fluxes to $\langle CO_2 \rangle$ depends on gradients in the mean state.

For instance, in the northern hemisphere the mean state is set by the biosphere. As the $\langle CO_2 \rangle_{bio}$ gradient increases in the amplified simulations, the relative contribution of regional fluxes diminishes. In Fig. 3.15a, regional fluxes draw down the Park Falls mean $\langle CO_2 \rangle_{bio}$ by ∼1.5 ppm during summer, a large deviation relative to a total north–south gradient of only 3 ppm across all TCCON sites. In Fig. 3.14b, the relative deviation is smaller because the large-scale signal is larger. To further illustrate, the relative effect of $\langle CO_2 \rangle_{fossil}$ decreases in experiments with CASA fluxes amplified in the boreal forests relative to standard CASA fluxes. The zonal contrasts in $\langle CO_2 \rangle_{fossil}$ shown in Fig. 3.3b are masked by contrasts set by biospheric fluxes and dynamics. During the growing season, the contrast between eastern and western United States owing to eastern fossil fuel emissions is ∼0.3 ppm while the contrast in $\langle CO_2 \rangle_{bio}$ over the same area is ∼1 ppm. In the simulation with enhanced boreal biospheric fluxes, this contrast increases to ∼1.5 ppm.

Recent studies suggest that vertical mixing in many transport models is sluggish in the mean (Yang et al., 2007; Nakatsuka and Maksyutov, 2009). Such errors have a large effect on near-surface $[CO_2]$ simulations. As we show here, however, vertical mixing has only a small effect on simulated $\langle CO_2 \rangle$. In AM2, a gross error in mixing (e.g., by putting the fluxes in the troposphere) alters the north–south gradient across the northern hemisphere midlatitudes by at most 0.2 ppm. Although such a bias in the $\langle CO_2 \rangle$ gradient must be taken into account when working with satellite or ground-based $\langle CO_2 \rangle$, it suggests that the insensitivity of $\langle CO_2 \rangle$ to local surface fluxes extends to insensitivity to local vertical mixing.

Because variations in $\langle CO_2 \rangle$ arise due to the large-scale gradients, the correlation of $\langle CO_2 \rangle'$ with θ' provides an important constraint. We anticipate that diagnostics such as the gradient $\partial_y \widehat{\langle CO_2 \rangle}$ estimated from covariations in $\langle CO_2 \rangle$ and θ can be used widely in total column and free tropospheric CO_2 studies to better understand large-scale patterns in carbon fluxes. As demonstrated through AM2 simulations, $\partial_y \widehat{\langle CO_2 \rangle}$ is sensitive to the north–south flux distribution. In a companion manuscript, we illustrate the use of the relationship between $\langle CO_2 \rangle$ and θ variations to evaluate fluxes based on TCCON $\langle CO_2 \rangle$ data, free tropospheric data, and recent satellite observations. We illustrate that the estimated $\langle CO_2 \rangle$ gradient provides new constraints on the gross fluxes on conti-

nental scales.

Potential temperature, θ, provides an alternative coordinate to compare multiple data sources. Commonly, CO_2 observations from different platforms are compared by averaging in time and space to satisfy coincidence criteria. Such averaging aliases error because of the large temporal and spatial variations in free tropospheric CO_2, associated with synoptic atmospheric variability. Instead, free tropospheric θ or L can be used as a conditional averaging coordinate. Satellite $\langle CO_2 \rangle$ will provide spatially and temporally dense data sets of modest precision, which can be statistically compared to $\langle CO_2 \rangle$ from other, more precise data sources using this approach.

Variations in CO_2 concentration are the driver of atmospheric inversion studies to infer CO_2 fluxes, so it is crucial to attribute these variations correctly, either to the mean state or to other factors, such as flux variability. Because large-scale gradients generate temporal variability through synoptic activity acting on them, accurate estimation of the north–south gradients ensures that the major source of variations in $\langle CO_2 \rangle$ is captured. These simulations suggest that $\langle CO_2 \rangle$ has a unique niche to fill in carbon cycle science, as it provides a strong constraint on large-scale flux estimates. In contrast, extracting information about regional scales (e.g., fossil fuel emissions) will be challenging. Coupled with data obtained at the surface and in the free troposphere, however, both large-scale and regional flux estimates should improve.

Bibliography

Anderson, J. L., Balaji, V., Broccoli, A. J., Cooke, W. F., Delworth, T. L., Dixon, K. W., Donner, L. J., Dunne, K. A., Freidenreich, S. M., Garner, S. T., Gudgel, R. G., Gordon, C. T., Held, I. M., Hemler, R. S., Horowitz, L. W., Klein, S. A., Knutson, T. R., Kushner, P. J., Langenhost, A. R., Lau, N. C., Liang, Z., Malyshev, S. L., Milly, P. C. D., Nath, M. J., Ploshay, J. J., Ramaswamy, V., Schwarzkopf, M. D., Shevliakova, E., Sirutis, J. J., Soden, B. J., Stern, W. F., Thompson, L. A., Wilson, R. J., Wittenberg, A. T., and Wyman, B. L.: The new GFDL global atmosphere and land model AM2-LM2: Evaluation with prescribed SST simulations, J. Climate, 17, 4641–4673, 2004.

Andres, R. J., Marland, G., Fung, I., and Matthews, E.: A 1x 1 Distribution of Carbon Dioxide Emissions From Fossil Fuel Consumption and Cement Manufacture, Global Biogeochem. Cy., 10, 419–429, doi:10.1029/96GB01523, 1996.

Chevallier, F., Breon, F. M., and Rayner, P. J.: Contribution of the Orbiting Carbon Observatory to the estimation of CO_2 sources and sinks: Theoretical study in a variational data assimilation framework, J. Geophys. Res.-Atmos., 112, D09307, doi:10.1029/2006JD007375, 2007.

Chevallier, F., L. Feng, H. Bosch, P. I. Palmer, and Rayner,P. J.: On the impact of transport model errors for the estimation of surface fluxes from GOSAT observations, Geophys. Res. Lett., 37, L21803, doi:10.1029/2010GL044652, 2010.

Ciais, P., Tans, P.P., Trolier, M., White, J. W.C., and Francey, R.J.: A Large Northern-hemisphere Terrestrial CO_2 Sink Indicated By the C-13/C-12 Ratio of Atmospheric CO_2, Science, 269, 1098–1102, 1995.

Crisp, D., Atlas, R. M., Breon, F. M., Brown, L. R., Burrows, J. P., Ciais, P., Connor, B. J., Doney, S. C., Fung, I. Y., Jacob, D. J., Miller, C. E., O'Brien, D., Pawson, S., Randerson, J. T., Rayner, P., Salawitch, R. J., Sander, S. P., Sen, B., Stephens, G. L., Tans, P. P., Toon, G. C., Wennberg, P. O., Wofsy, S. C., Yung, Y. L., Kuang, Z. M., Chudasama, B., Sprague, G., Weiss, B., Pollock, R., Kenyon, D., and Schroll, S.: The orbiting carbon observatory (OCO) mission, "Trace constituents in the troposphere and lower stratosphere" in the book series, Adv. Space Res., 34, 700–709, 2004.

Denning, A. S., Fung, I. Y., and Randall, D.: Latitudinal gradient of atmospheric CO_2 due to seasonal exchange with land biota, Nature, 376, 240–243, 1995.

Gurney, K. R., Law, R. M., Denning, A. S., Rayner, P. J., Baker, D., Bousquet, P., Bruhwiler, L., Chen, Y.-H., Ciais, P., Fan, S., Fung, I. Y., Gloor, M., Heimann, M., Higuchi, K., John, J., Maki, T., Maksyutov, S., Masarie, K., Peylin, P., Prather, M., Pak, B. C., Randerson, J., Sarmiento, J., Taguchi, S., Takahashi, T., and Yuen, C.-W.: Towards robust regional estimates of CO_2 sources and sinks using atmospheric transport models, Nature, 415, 626–630, doi:10.1038/415626a, 2002.

Gurney, K. R., Law, R. M., Denning, A. S., Rayner, P. J., Pak, B. C., Baker, D., Bousquet, P., Bruhwiler, L., Chen, Y. H., Ciais, P., Fung, I. Y., Heimann, M., John, J., Maki, T., Maksyutov, S., Peylin, P., Prather, M., and Taguchi, S.: Transcom 3 inversion intercomparison: Model mean results for the estimation of seasonal carbon sources and sinks, Global Biogeochem. Cy., 18, GB1010, doi:10.1029/2003GB002111,2004.

Hovmöller, E., The trough and ridge diagram: Tellus, 1, 62-66, 1949.

Le Quéré, C., Raupach, M. R., Canadell, J. G., Marland, G., Bopp, L., Ciais, P., Conway, T. J., Doney, S. C., Feely, R. A., Foster, P., Friedlingstein, P., Gurney, K., Houghton, R. A., House, J. I., Huntingford, C., Levy, P. E., Lomas, M. R., Majkut, J., Metzl, N., Ometto, J. P., Peters, G. P., Prentice, I. C., Randerson, J. T., Running, S. W., Sarmiento, J. L., Schuster, U., Sitch, S., Takahashi, T., Viovy, N., van der Werf, G. R., and Woodward, F. I.: Trends in the sources and sinks of carbon dioxide, Nature Geosci., 2, 831–836, 2009.

Lin, S. J.: A "vertically Lagrangian" finite-volume dynamical core for global models, Mon. Weather Rev., 132, 2293–2307, 2004.

Marland, G. and Rotty, R. M.: Carbon-dioxide Emissions From Fossil-fuels - A Procedure For Estimation and Results For 1950-1982, Tellus B, 36, 232–261, 1984.

Miyazaki, K., Patra, P. K., Takigawa, M., Iwasaki, T., and Nakazawa, T.: Global-scale transport of carbon dioxide in the troposphere, J. Geophys. Res., 113, D15301, doi:10.1029:2007JD009557, 2008.

Miyazaki, K., Machida, T., Patra, P. K., Iwasaki, T., Sawa, Y., Matsueda, H., and Nakazawa, T.: Formation mechanisms of latitudinal CO_2 gradients in the upper troposphere over the subtropics and tropics, J. Geophys. Res., 114, D03306, doi:10.1029/2008JD010545, 2009.

Nakatsuka, Y. and Maksyutov, S.: Optimization of the seasonal cycles of simulated CO_2 flux by fitting simulated atmospheric CO_2 to observed vertical profiles, Biogeosciences, 6, 2733–2741, 2009.

Nevison, C. D., Mahowald, N. M., Doney, S. C., Lima, I. D., Van der Werf, G. R., Randerson, J. T., Baker, D. F., Kasibhatla, P., and McKinley, G. A.: Contribution of ocean, fossil fuel, land biosphere, and biomass burning carbon fluxes to seasonal and interannual variability in atmospheric CO_2, J. Geophys. Res.-Biogeo., 113, G01010,doi:10.1029/2007JG000408, 2008.

Olsen, S. C. and Randerson, J. T.: Differences between surface and column atmospheric CO_2 and implications for carbon cycle research, J. Geophys. Res., 109, D02301, doi:10.1029/2003JD003968, 2004.

Parrington, M., Jones, D.B.A., Bowman, K.W., Thompson, A.M., Tarasick, D.W., Merrill, J., Oltmans, S.J., Leblanc, T., Witte, J.C, and Millet, D.B.: Impact of the assimilation of ozone from the Tropospheric Emission Spectrometer on surface ozone across North America, Geophys. Res. Lett., 36, L04802, doi:10.1029/2008GL036935, 2009.

Peters, W., Jacobson, A. R., Sweeney, C., Andrews, A. E., Conway, T. J., Masarie, K., Miller, J. B., Bruhwiler, L. M. P., Pétron, G., Hirsch, A. I., Worthy, D. E. J., van der Werf, G. R., Randerson, J. T., Wennberg, P. O., Krol, M. C., and Tans, P. P.: An atmospheric perspective on North American carbon dioxide exchange: CarbonTracker, P. Natl. Acad. Sci., 104, 18925–18930, doi:10.1073/pnas.0708986104, 2007.

Piao, S. L., Ciais, P., Friedlingstein, P., Peylin, P., Reichstein, M., Luyssaert, S., Margolis, H., Fang, J. Y., Barr, A., Chen, A. P., Grelle, A., Hollinger, D. Y., Laurila, T., Lindroth, A., Richardson, A. D., and Vesala, T.: Net carbon dioxide losses of northern ecosystems in response to autumn warming, Nature, 451, 49–53, 2008.

Randerson, J.T., Thompson, M.V., Conway, T.J., Fung, I.Y., Field, C.B.: The contribution of terrestrial sources and sinks to trends in the seasonal cycle of atmospheric carbon dioxide, Global Biogeochem. Cy., 11, 535–560, 1997.

Sawa, Y., Machida, T., and H. Matsueda: Seasonal variations of CO_2 near the tropopause observed by commercial aircraft, J. Geophs. Res.-Atmos., 113, D23301, doi:10.1029/2008JD010568, 2008.

Stephens, B. B., Gurney, K. R., Tans, P. P., Sweeney, C., Peters, W., Bruhwiler, L., Ciais, P., Ramonet, M., Bousquet, P., Nakazawa, T., Aoki, S., Machida, T., Inoue, G., Vinnichenko, N., Lloyd, J., Jordan, A., Heimann, M., Shibistova, O., Langenfelds, R. L., Steele, L. P., Francey, R. J., and Denning, A. S.: Weak northern and strong tropical land carbon uptake from vertical profiles of atmospheric CO_2, Science, 316, 1732–1735, 2007.

Takahashi, T., Sutherland, S. C., Sweeney, C., Poisson, A., Metzl, N., Tilbrook, B., Bates, N., Wanninkhof, R., Feely, R. A., Sabine, C., Olafsson, J., and Nojiri, Y.: Global sea-air CO_2 flux based on climatological surface ocean pCO_2, and seasonal biological and temperature effects, Deep-Sea Res. Pt II, 49, 1601–1622, 2002.

Washenfelder, R. A., Toon, G. C., Blavier, J.-F., Yang, Z., Allen, N. T., Wennberg, P. O., Vay, S. A., Matross, D. M., and Daube, B. C.: Carbon dioxide column abundances at the Wisconsin Tall Tower site, J. Geophys. Res., 111, D22305 , doi:10.1029/2006JD007154, 2006.

Yang, Z., Washenfelder, R. A., Keppel-Aleks, G., Krakauer, N. Y., Randerson, J. T., Tans, P. P., Sweeney, C., and Wennberg, P. O.: New constraints on Northern Hemisphere growing season net flux, Geophys. Res. Lett., 34, L12807, doi:10.1029/2007GL029742, 2007.

Yokota, T., Yoshida, Y., Eguchi, N., Ota, Y., Tanaka, T., Watanabe, H., and Maksyutov, S.: Global Concentrations of CO_2 and CH_4 Retrieved from GOSAT: First Preliminary Results, Sola, 5, 160–163, 2009.

Chapter 4

The imprint of surface fluxes and transport on variations in total column carbon dioxide

4.1 Introduction

Accurate determination of surface fluxes of carbon dioxide is important both to predict future climate and increasingly to support climate and energy policy. The long-term trend in atmospheric CO_2 depends not only on anthropogenic emissions; natural fluxes of CO_2 to sinks in the ocean and terrestrial biosphere control the fraction of anthropogenic CO_2, presently ∼45%, that remains in the atmosphere (Gloor et al., 2010). These natural fluxes respond to changes in atmospheric composition and climate on both interannual and longer timescales. Partitioning uptake and release of CO_2 among its terrestrial and oceanic components is necessary to gain insight into the processes controlling these fluxes.

Ideally, self-consistent flux estimates over spatial scales ranging from local to global could be determined from a single set of observations. In reality, no single type of measurement is capable of providing such a constraint. For example, observations of the isotopic composition of CO_2 (Ciais et al., 1995) and the atmospheric O_2 mixing ratio (Keeling et al., 1996) provide estimates of net ocean and biospheric uptake globally, but provide little or no information about the spatial distribution of fluxes. At local scales, terrestrial biospheric carbon fluxes can be measured quite accurately via inventory (e.g., changes in carbon stocks (Saatchi et al., 2007)) and by atmospheric observations

(e.g., eddy-covariance (Baldocchi, 2008)). Such measurements are, however, representative only of small spatial scales (<10 km^2); other data sets such as measures of land color or chlorophyll fluorescence from satellite are needed to scale the local flux estimates to regional and global scales (Frankenberg et al., 2011). Likewise, estimation of ocean fluxes from surface pCO_2 measurements requires substantial upscaling of sparse observations.

To infer surface fluxes at intermediate spatial scales (e.g., continental scale), inverse modeling of atmospheric carbon dioxide observations has been used in a variety of approaches (Rayner and O'Brien, 2001). For example, the TransCom experiment estimated continental fluxes at scales of 10^7 km^2 using a suite of transport models, each constrained by the same boundary layer CO_2 mixing ratio, $[CO_2]$, data (Gurney et al., 2002), whereas CarbonTracker optimizes regional fluxes via CO_2 data assimilation (Peters et al., 2007). Like other methods, inverse modeling has its limitations. Although the global network to monitor CO_2 is growing, there are only limited observations of atmospheric CO_2, most of which are obtained within the planetary boundary layer. Therefore, a sparse set of CO_2 observations with small, non-overlapping footprints must simultaneously and coherently constrain fluxes at larger spatial scales.

Inverse modeling is also complicated by a more fundamental constraint. The ability to use surface concentration data to infer fluxes requires accurate modeling of boundary layer height and rates of entrainment between the boundary layer and the free troposphere. Gradients in atmospheric carbon dioxide are influenced by covariance between the strength of surface fluxes and the strength of vertical mixing (Denning et al., 1995). Primarily as a result of this covariance, studies have shown that inversion results are very sensitive to how vertical mixing is represented in transport models (Stephens et al., 2007).

Total column carbon dioxide, $\langle CO_2 \rangle$, is a new measurement that will complement surface data in inverse studies by bridging the spatial gap between the small-scale flux constraints provided by direct flux observations or boundary layer concentration data and the global constraints provided by isotopes or atmospheric O_2. Because the column integrates not only boundary layer CO_2 but also free tropospheric CO_2, its footprint is much larger. A companion paper (Keppel-Aleks et al., 2011),

hereafter KWS11, suggests based on simulations that $\langle CO_2 \rangle$ has a large footprint and is largely insensitive to assumptions about small scale mixing. In simulations in KWS11, variations in $\langle CO_2 \rangle$ at all timescales are primarily tied to large-scale rather than local fluxes. Diurnal changes in the column are only weakly influenced by local fluxes, while synoptic-scale variations in the column are due primarily to advection across the mean hemispheric-scale north-south gradient.

Here, we use data from the Total Carbon Column Observing Network (TCCON) to test the simulations of KWS11. TCCON is a network of high resolution ground-based Fourier transform spectrometers (FTS) that obtain direct solar absorption spectra (Wunch et al., 2011). We focus our analysis on two diagnostics for variations in the column. The first is the seasonal cycle amplitude (SCA), which quantifies the seasonal variation in $\langle CO_2 \rangle$ at a given location. The second is the north-south gradient in $\langle CO_2 \rangle$, which can be estimated even from sparse ground-based observations using covariations in observed $\langle CO_2 \rangle$ and a dynamical tracer such as potential temperature, θ (KWS11).

We complement TCCON data with eddy covariance data to determine the contribution of local surface fluxes to variations in $\langle CO_2 \rangle$. We also use aircraft in situ profiling to further test the hypothesis that large-scale spatial variations in free tropospheric CO_2 are driven by zonal fluxes.

The structure of this paper is as follows: In section 4.2, we describe the $\langle CO_2 \rangle$, eddy covariance flux, and in situ $[CO_2]$ data used in this study. We also briefly describe the simulations to which the data are compared. In section 4.3, we discuss variations in column data at diurnal and seasonal timescales. A comparison of variations in $\langle CO_2 \rangle$ to variations in local fluxes (eddy covariance observations) and gradients in the free troposphere (aircraft observations) both confirm that $\langle CO_2 \rangle$ variations primarily contain hemispheric-scale flux information. In section 4.3.4, we compare the SCAs and the north-south gradient from northern hemisphere TCCON sites to KWS11 simulations to reveal discrepencies in current estimates of biospheric fluxes. In section 4.4, we discuss the implications of these results.

Table 4.1: TCCON sites and their seasonal cycle amplitudes (SCA)

Site	Lat	Lon	Observed SCA	CASA SCA	Boreal SCA	Early SCA	CarbonTracker SCA
Bialystok	52° N	20° E	10.6	6.7±0.3	8.4±0.3	9.8±0.2	8.2±0.3
Park Falls	46° N	90° W	8.6±1.0	6.9±0.5	8.8±0.4	9.6±0.4	8.2 ±1.0
Lamont	37° N	100° W	6.8±1.0	5.3±0.2	6.6±0.3	7.3±0.4	5.8±0.6
Pasadena	34° N	119° W	6.0	4.4±0.2	5.3±0.3	5.9±0.2	4.9±0.2
Lauder	45° S	170° E	1.7±0.3	0.9±0.2	1.1±0.2	1.2±0.3	1.1±0.2

4.2 Data and Methods

4.2.1 Ground based total column data

We use $\langle CO_2 \rangle$ data from Total Carbon Column Observing Network (TCCON) observatories. The first dedicated TCCON observatories became operational in 2004 and the network has subsequently grown. Table 4.1 lists the sites used in this study, limited to midlatitude sites that have obtained data over at least one complete seasonal cycle. We summarize the data acquisition and retrieval method, but more details are provided in Wunch et al. (2011) and references therein.

Briefly, TCCON observatories use Fourier transform spectrometers (FTS) to record high resolution spectra (0.02 cm^{-1}) in the near infrared (3800-15500 cm^{-1}). A profile scaling retrieval is used to determine the vertical CO_2 column from observed spectra. A priori CO_2 profiles are generated using an analytical function that varies seasonally and meridionally based on GLOBALVIEW CO_2 in the troposphere and applies the age-of-air measurements of Andrews et al. (2001) in the stratosphere. Temperature, water vapor profiles, and tropopause pressure from NCEP reanalysis (Kalnay et al., 1996) are used to map the assumed profile onto 71 vertical layers at 1 km resolution. Gases, including CO_2, O_2, and H_2O are retrieved simultaneously in selected spectral windows. The CO_2 retrieval scales the a priori profile to best match the recorded spectrum in two spectral windows centered at 6220 cm^{-1} (80 cm^{-1} wide) and 6339 cm^{-1} (85 cm^{-1} wide). The retrieved column abundance [mol m^{-2}] is normalized by the retrieved column abundance of O_2 to yield $\langle CO_2 \rangle$ [ppm].

TCCON data are corrected to account for known biases. $\langle CO_2 \rangle$ is corrected empirically for airmass dependence due to bias in spectroscopic parameters used in the retrievals (Wunch et al., 2011).

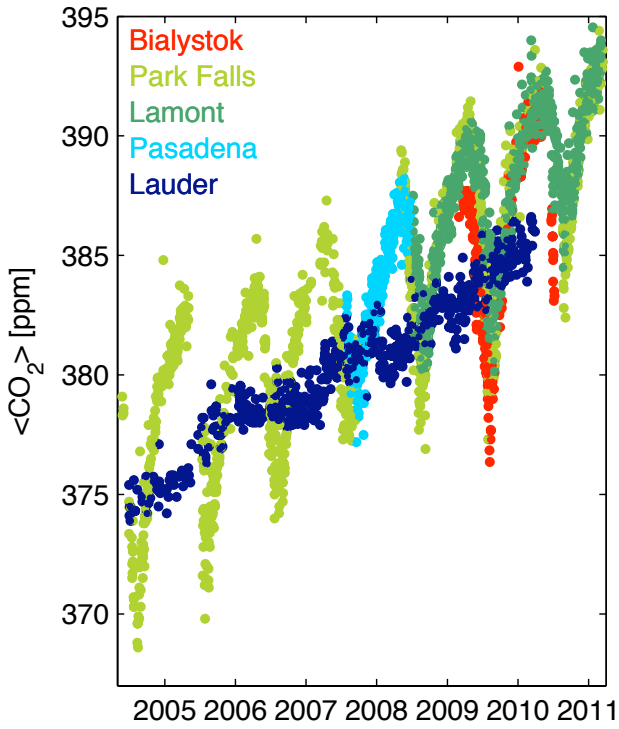

Figure 4.1: Daily mean $\langle CO_2 \rangle$ at five TCCON sites. Details about the location and operational dates for each site are provided in Table 4.1.

TCCON data have been rigorously calibrated against aircraft profiles of CO_2 and are traceable to World Meteorological Organization standards (Wunch et al., 2010). After calibration, the accuracy and precision are both better than 0.2% (0.8 ppm in $\langle CO_2 \rangle$). In the analysis presented here, we have used simultaneous measurements of $\langle CO \rangle$ to remove the local fossil component of observed CO_2 for data obtained at the Pasadena site, in the Los Angeles urban area (Wunch et al., 2009). More details are provided in Appendix A. At the other sites, $\langle CO_2 \rangle$ and $\langle CO \rangle$ are not correlated, so no empirical correction was applied.

Fig. 4.1 shows the daily median $\langle CO_2 \rangle$ at the sites used in this study. We include all observations for which the retrieved error is <1.5 ppm. These timeseries show variability at several timescales: a long-term secular increase, seasonal variations, particularly in the northern hemisphere, and day-to-day variations are all evident in TCCON data. There is also substantial interannual variability in the SCA which will be discussed in Section 4.4.

Because the column data are sparse and not all the observatories have operated simultaneously, we focus on a statistical comparison of the data with simulations. For each site, we subtract the linear trend in $\langle CO_2 \rangle$ at Lauder, New Zealand, a southern hemsiphere site with small seasonal and interannual variability (Fig. 4.1). Thus, the detrended data retain the absolute offset between $\langle CO_2 \rangle$ at each site. We then compare the seasonal variation in $\langle CO_2 \rangle$ by computing the peak-to-trough seasonal cycle amplitude as the difference between maximum and minimum monthly median $\langle CO_2 \rangle$.

We estimate the north-south gradient across TCCON sites using the covariation between $\langle CO_2 \rangle$ and potential temperature at 700 hPa, a dynamical tracer, as described in KWS11. The daily mean $\langle CO_2 \rangle$ timeseries from TCCON sites are gap-filled using a cubic spline before we apply a 3-21 day bandpass filter to remove seasonal variations at low frequencies and to isolate synoptic-scale variations in $\langle CO_2 \rangle$. The results are not sensitive to the exact filter cutoffs. We denote variations as $\langle CO_2 \rangle'$. We use NCEP reanalysis data to calculate bandpass filtered θ variations and the meridional θ gradient at each site in order to estimate the meridional displacement, L, of observed air parcels from a reference latitude with mean potential temperature $\overline{\theta_0}$:

$$L = \frac{\theta' - \overline{\theta}_0}{\partial_y \overline{\theta}}, \tag{4.1}$$

We then use the meridional displacement and variations in $\langle CO_2 \rangle$ to calculate the meridional gradient, $\partial_y \widehat{\langle CO_2 \rangle}$ [ppb km^{-1}]:

$$\partial_y \widehat{\langle CO_2 \rangle} = \frac{\langle CO_2 \rangle'}{L}. \tag{4.2}$$

Here, we use the overhat to represent that the gradient is an estimated quantity.

We calculate $\partial_y \widehat{\langle CO_2 \rangle}$ only where there is enough data (more than two years of data from a single site). Additionally, direct estimation of $\partial_y \widehat{\langle CO_2 \rangle}$ using this method only works well in the midlatitudes where eddy activity is substantial and significant CO_2 and θ gradients exist (KWS11). We can, however, use θ as an alternative meridional coordinate everywhere outside the tropics. Therefore, we compare $\langle CO_2 \rangle$ at various TCCON sites as a function of meridional displacement.

However, we only calculate $\partial_y \widehat{\langle \mathrm{CO}_2 \rangle}$ directly from the observations at Park Falls and Lamont due to these methodological and data constraints.

4.2.2 Net ecosystem exchange estimated from column drawdown

We examine diurnal variations in $\langle \mathrm{CO}_2 \rangle$ by computing the mass change in the total column over the course of a single day. The vertical column of any gas, $\mathrm{VC_G}$ [mol m^{-2}] is the product of the vertically averaged mixing ratio of the gas, $\langle \mathrm{G} \rangle$, and the mass of the atmospheric column as expressed in Equation 4.3:

$$VC_G = \langle G \rangle \cdot \frac{P_s - q}{g \cdot M_{air}} = \langle G \rangle \cdot VC_{air} \tag{4.3}$$

where P_s is the surface pressure, q is the vertically integrated contribution of water to the surface pressure, g the gravitational acceleration, and M_{air} the molecular mass of air.

We differentiate Equation 4.3, assuming the vertical column of air is constant, to determine the time rate of change in VC_{CO2}:

$$\frac{dVC_{CO2}}{dt} = \frac{d\langle CO_2 \rangle}{dt} \cdot VC_{air} \tag{4.4}$$

In equation 4.4, $\frac{dVC_{CO2}}{dt}$ has units of flux [mol m^{-2} s^{-1}]. The column-averaged mixing ratio, $\langle \mathrm{CO}_2 \rangle$, may change due either to local surface fluxes, to changes in the tropopause height, or to advection across horizontal CO_2 gradients. If we assume advection has a negligible influence on the change in $\langle \mathrm{CO}_2 \rangle$, we can substitute Equation 4.3 for G=O_2 into Equation 4.4 to calculate NEE from TCCON observations as:

$$NEE_{FTS} = \frac{VC_{O2}}{\langle O_2 \rangle} \cdot \frac{\Delta \langle CO_2 \rangle}{\Delta t} \tag{4.5}$$

We calculate $\Delta \langle \mathrm{CO}_2 \rangle$ as the four hour difference in $\langle \mathrm{CO}_2 \rangle$ centered around solar noon. This method of calculating $\frac{\Delta \langle \mathrm{CO}_2 \rangle}{\Delta t}$ maximizes the number of days with adequate temporal coverage while yielding similar results to fitting a line through the data obtained on a single day. VC_{O2} is averaged from

retrievals within two hours on either side of solar noon, and we use a constant value of 0.20939 for $\langle O_2 \rangle$ (Tohijma et al., 2005). Although the atmospheric concentration of O_2 is decreasing by $\sim$4 ppm y^{-1}, this change has a negligible impact on our estimate of NEE. Equation 4.5 neglects the contributions of changes in pressure and water vapor to the change in VC_{CO2}, which are small on four hour timescales.

We test how well NEE inferred from column drawdown represents local biospheric fluxes by comparing Park Falls NEE to eddy covariance flux observations at the same location (discussed in section 4.2.3). Because the column retrieval is not equally sensitive to all levels of the atmosphere, we must incorporate the averaging kernel of the FTS into the comparison (see Appendix B for more details). We incorporate the averaging kernel by multiplying the eddy covariance NEE by the mean averaging kernel at the surface at $\pm$2 hours of solar noon. This method is similar to the approach used by Wunch et al. (2009) to analyze diurnal variations in $\langle CO_2 \rangle$ and other greenhouse gases in the Los Angeles basin.

4.2.3 Eddy covariance flux data

Fluxes of CO_2, water vapor, virtual temperature, and momentum are measured continuously at 30, 122, and 396 m on the WLEF tower in Park Falls. CO_2 and water vapor mixing ratios are measured using infrared gas analyzers (Li-Cor Inc., Lincoln, Nebraska, model LI-6262). Virtual temperature and momentum are measured using sonic anemometers (Applied Technologies Inc., Boulder, Colorado, model SATI/3K or Campbell Scientific Inc., Logan, Utah, model CSAT3). High-precision, high-accuracy CO_2 mixing ratio measurements are simultaneously recorded at 11, 30, 76, 122, 244, and 396 m using two Li-Cor model LI-6251 infrared gas analyzers (Bakwin et al., 1998; Zhao et al., 1997). These measurements are used to calibrate the fast-response infrared gas analyzers and to calculate the rate of change of storage for CO_2 (Davis et al., 2003). The eddy covariance instrumentation and methodology is described in detail in Berger et al. (2001) and Davis et al. (2003). Previous work has examined the long-term average of NEE at the three observation levels of the WLEF tower (Davis et al., 2003), with consideration of the measurement footprint under

varying conditions of convective mixing. Davis et al. (2003) developed an algorithm for preferred NEE that combines measurements at the three levels to maintain a large footprint while avoiding the influence of the clearing around the tower. We determine daily average NEE within two hours of solar noon to compare with drawdown in the column. We use data obtained between 2004 and 2009, only on days with both column and eddy covariance data.

4.2.4 Aircraft data

Free tropospheric [CO_2] data from two field campaigns that had extensive geographic coverage are used in this analysis. Free tropospheric [CO_2] data was obtained in situ during the Intercontinental Chemical Transport Experiment (INTEX-NA), a NASA-sponsored aircraft mission in July-August 2004 (Choi et al., 2008). Data were obtained between 28° and 54°N along the flight tracks shown in Fig. 4.2. Carbon dioxide mixing ratios were determined using a modified LI-COR model 6252 non-dispersive infrared gas analyzer. This dual-cell instrument achieves high precision by measuring the differential absorption between sample air and a calibrated reference gas that is traceable to the WMO primary CO_2 standards. The LI-COR-based CO_2 sampling system was operated at constant pressure (333 hPa) and temperature (40°C), and had a precision of 0.07 ppm and accuracy of 0.20 ppm (1 second, 1-σ precision, 1-σ accuracy). Experimental procedures are described in detail by Vay et al. (2003).

Free tropospheric [CO_2] was measured during the first HIAPER Pole-to-Pole Observations (HIPPO 1) campaign in January 2009 over the Pacific (Wofsy et al., 2011). [CO_2] were measured between 80°N and 67°S using three instruments, two Li-Cor non-dispersive infrared gas analyzers as well as a quantum cascade laser system and two flask samplers. In this study, we use QCLS data, which has precision of 0.02 ppm and accuracy of 0.1 ppm (1 second, 1-σ precision, 1-σ accuracy), except for data obtained on 28-30 January, where we use the mean of the data from the OMS and AO2 infrared gas analyzers. The OMS instrument has 0.01 ppm precision and 0.01 ppm accuracy and the AO2 instrument has 0.3 ppm precision and 0.1 ppm accuracy. During HIPPO 1, [CO_2] was sampled in the free troposphere over a series of vertical profiles. We integrate profiles that exceed 7 km in

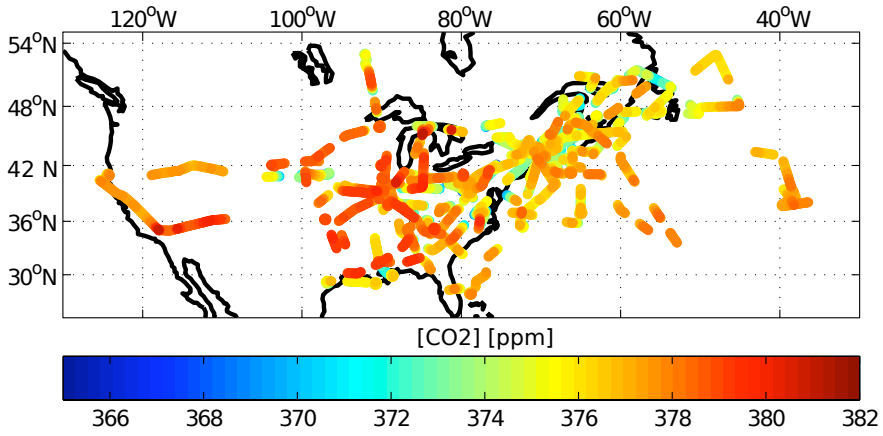

Figure 4.2: Flight tracks in the free troposphere (350-800 hPa) during INTEX-NA during July-August 2004. Free tropospheric CO_2 is highly variable during these two months.

vertical extent to determine the partial column mixing ratio. The location of the profiles obtained in the northern hemisphere are shown in Fig. 4.3.

For both campaigns, the cited accuracy is relative to the WMO standards. It is worth noting that actual limits to accuracy are in the form of non-random, systematic biases. Expression of accuracy as a 1-σ value represents a judgment based on intercomparison activities that these biases are less than or equal to the given values 68% of the time. During both INTEX-NA and HIPPO 1, profile measurements were obtained at TCCON sites. These profiles are among the data used to calibrate TCCON $\langle CO_2 \rangle$ data (Washenfelder et al., 2006; Wunch et al., 2010).

4.2.5 Simulations with a transport model

Below, we compare variations in observed $\langle CO_2 \rangle$ against simulations from KWS11. Briefly, these simulations use the AM2 general circulation model (GCM) of NOAA's Geophysical Fluid Dynamics Laboratory, a free-running GCM with prescribed sea surface temperatures (Anderson et al., 2004). We run the model at 2° latitude by 2.5° longitude resolution with 25 vertical levels. We use annually balanced NEE from the monthly Carnegie Ames Stanford Approach (CASA) (Randerson et al., 1997). Here, NEE represents the residual of monthly net primary production (NPP) and respiration fluxes that have been redistributed at 3 hour resolution based on 2001 climatology (Olsen and

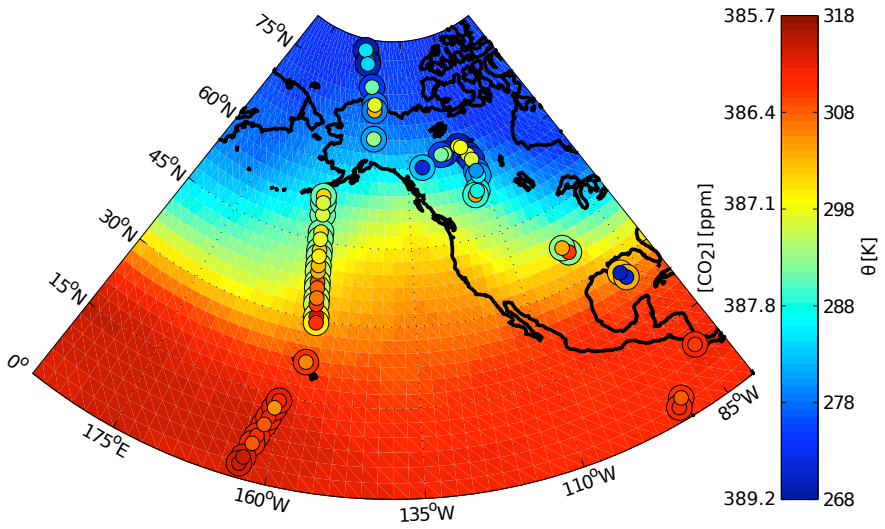

Figure 4.3: HIPPO partial CO_2 columns overlaid on January monthly mean potential temperature, θ. The inner circle is colored by $\langle CO_2 \rangle$, while the outer circle is colored by θ at 700 hPa at the time the profile was acquired. Although there are outliers over the Gulf of Mexico, θ and $\langle CO_2 \rangle$ are generally anticorrelated during January.

Randerson, 2004). CASA biospheric fluxes are commonly used by the carbon cycle community and are the basis for prior fluxes in many inversion simulations including TransCom (Gurney et al., 2002) and CarbonTracker (Peters et al., 2007).

Ocean exchange is based on monthly-mean fluxes derived from surface ocean pCO2 data (Takahashi et al., 2002). These ocean fluxes represent an annual and global mean sink of atmospheric CO_2 of $\sim$1.4 Pg C y^{-1}. We use annual mean fossil emissions for the year 1990 (Andres et al., 1996), when net global emissions were 5.5 PgC y^{-1}. These emissions are determined from self-reported fuel consumption at the national level (Marland and Rotty, 1984) and converted to regional fluxes proportional to local population density. We also use updated fossil fluxes determined at monthly time resolution from 2004-2007 (Gregg and Andres, 2008; Gregg et al., 2009; Andres et al., 2011) to test the sensitivity of the column to these larger and temporally varying parameterization of the fossil fluxes.

We compute the SCA and the estimated gradient $\partial_y \widehat{\langle CO_2 \rangle}$ for the model gridboxes corresponding to TCCON sites to compare to the observations. We incorporate the FTS averaging kernel when comparing AM2 and TCCON $\langle CO_2 \rangle$; more details on how the averaging kernel was applied to the

simulations are provided in Appendix B.

As shown in KWS11, biospheric fluxes impart the largest variations in $\langle CO_2 \rangle$. We therefore focus our comparisons of observed $\langle CO_2 \rangle$ against three simulations with variations in biospheric fluxes: CASA exchange, boreal amplified CASA exchange, and boreal extended exchange as described in KWS11. In the boreal amplified simulations, NEE has been amplified by a Gaussian weighting function centered at 55°N with a peak value of 1.5 that decays to unity over a standard deviation of 10°. Integrated over 45-65°N, NEE is increased by 40%; integrated over the northern hemisphere, NEE is increased by 30%. In the boreal extended sensitivity simulations, we use NEE with the boreal amplification described above, but move the onset of the growing season forward by one month in the boreal regions between 50-60°N.

4.3 Results

4.3.1 Diurnal Variations

Diurnal gradients in observed $\langle CO_2 \rangle$ are small and influenced by a large spatial footprint. At Park Falls, the change in $\langle CO_2 \rangle$ during the summer growing season is ∼2 ppm within a given day (Fig. 4.4). NEE inferred from column drawdown shows little correlation with NEE inferred from eddy covariance on daily timescales (Fig. 4.5a). A regression of NEE from column drawdown against NEE from eddy covariance on individual days yields a slope of 0.9 ±0.3, an intercept of -5 ± 2 μmol $m^{-2}s^{-1}$, and an R^2 of 0.11. Consistent with this large scatter, KWS11 show that diurnal variations in simulated $\langle CO_2 \rangle$ are only weakly correlated with the underlying flux.

Aggregating NEE on weekly and monthly timescales in Fig. 4.5b and Fig. 4.5c, the comparison between the two methods becomes more favorable (weighted R^2 of 0.94 and 0.86 for weekly and monthly data, respectively). We use a fit that accounts for the standard error in both eddy covariance NEE and column NEE over the aggregated time period (York et al., 2004). The slopes are 1.5±0.2 for the weekly mean data and 1.5±0.2 for monthly mean data and the fits have a negative intercept of -4.9±0.8 μmol m^{-2} s^{-1} for weekly mean data and -4.3±0.7 μmol m^{-2} s^{-1} for monthly mean data.

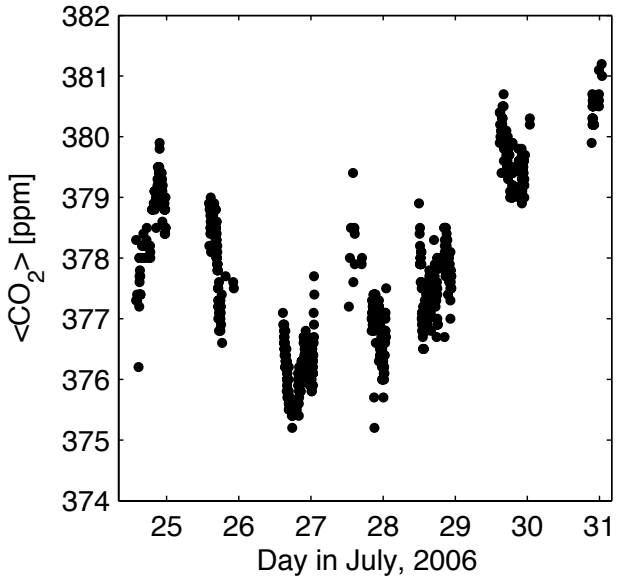

Figure 4.4: Daily drawdown in $\langle CO_2 \rangle$ at Park Falls during one week in July 2006. Within one day, $\langle CO_2 \rangle$ changes by up to 2 ppm.

The larger NEE inferred from the FTS may be attributable to column drawdown having a larger footprint. Regional studies have shown divergent estimates for NEE in the area around Park Falls using several bottom-up and top-down methods (Desai et al., 2010). We have confirmed that the offset between NEE from column drawdown and from eddy covariance is not due to seasonal, large-scale uptake by removing the seasonal trend from $\langle CO_2 \rangle$ before determining the diurnal drawdown in the column. Neither the slope nor the intercept are significantly affected.

While horizontal and vertical advection make a negligible contribution to daytime NEE determined from eddy covariance (Wang et al., 2005; Yi et al., 2000), horizontal advection has a large influence on variations in the column even over four hours. Our formulation for calculating NEE from column drawdown assumes that the change in column CO_2 was caused only by the underlying flux. On time scales of days and less, however, the column is influenced by advection of CO_2 from other locations. Consistent with this hypothesis, aggregating NEE inferred from the column over several synoptic cycles improves the agreement with eddy covariance NEE, as shown in Fig. 4.5b-c. We have investigated whether there is a relationship between the mismatch in NEE derived from the two measurements and meteorological variables such as wind speed, wind direction, and diurnal

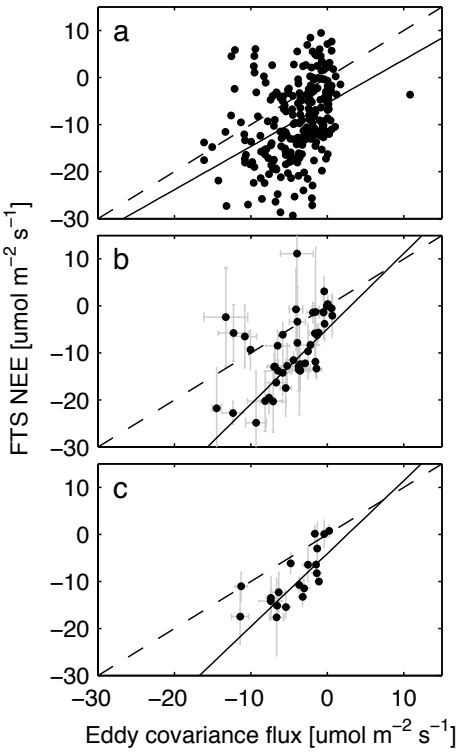

Figure 4.5: Comparison between NEE calculated from drawdown in the total column and NEE infered from eddy covariance measurements at Park Falls, Wisconsin. Drawdown in the column is calculated over a 4 hour period symmetric about solar noon. Eddy covariance fluxes are averaged over the same time period. (a) NEE calculated each day for which data are available. (b) Data aggregated by week of year. (c) Data aggregated for each month.

changes in pressure and temperature. We do not find correlations between diagnostics for advection and mismatch in NEE. Modelling tools such as back trajectory analysis originating from multiple levels in the column may prove helpful in diagnosing changes in $\langle CO_2 \rangle$ on sub-diurnal timescales, but they require accurate background $\langle CO_2 \rangle$ distributions to be useful.

In summary, the comparison between drawdown in $\langle CO_2 \rangle$ and eddy covariance flux confirms that regional information is contained in column observations, but regional flux signals are obscured by larger-scale variations in $\langle CO_2 \rangle$ even on diurnal timescales.

4.3.2 Horizontal gradients as sources of synoptic variations in $\langle CO_2 \rangle$

Advection leaves a notable signature on $\langle CO_2 \rangle$ at seasonal timescales as well as at shorter timescales. Fig. 4.6 illustrates the relationship between synoptic-scale variability and north-south gradients in

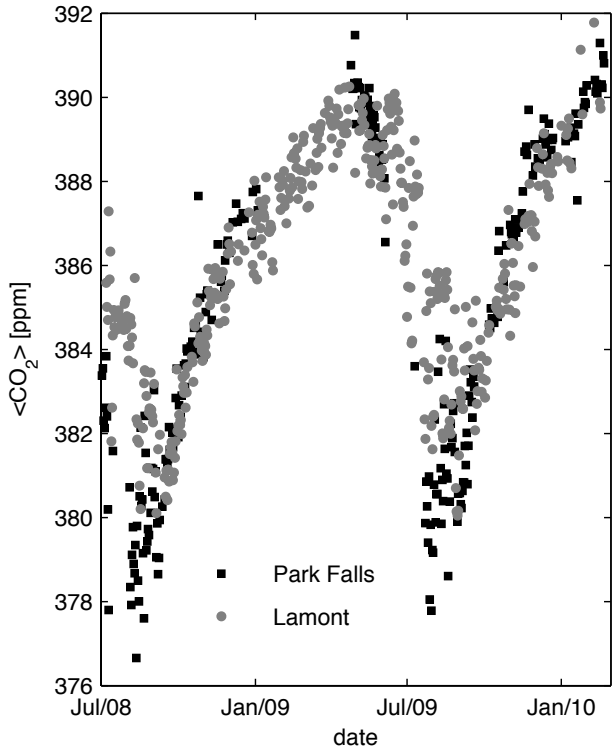

Figure 4.6: Fifteen months of daily mean $\langle CO_2 \rangle$ at Park Falls and Lamont. We see the impact of large-scale gradients in these two timeseries: the records are similar outside the growing season (when north-south gradient in CO_2 is small) and the records diverge during the growing season (June-August) when CO_2 is drawn down in the north. When the north-south gradient is larger, synoptic scale variations in daily mean $\langle CO_2 \rangle$ are larger, reflecting the fact that variations arise from advection across gradients.

$\langle CO_2 \rangle$ at Park Falls and Lamont, two North American TCCON sites that are separated by 9° latitude. Outside the growing season, the two timeseries esentially overlap, indicative of a small meridional $\langle CO_2 \rangle$ contrast between the two sites. At the onset of the growing season (May), the two timeseries diverge; the larger decrease in $\langle CO_2 \rangle$ at Park Falls results in a significant contrast ($\sim$3 ppm) between the two sites. During the period of divergence, the variability at each site increases noticeably. This variability is a result of the increased meridional gradient and weather systems advecting air to each site from the north and south. Although the mean $\langle CO_2 \rangle$ is quite different at the two sites during the growing season, there is overlap between the high $\langle CO_2 \rangle$ values at Park Falls and the lowest $\langle CO_2 \rangle$ values at Lamont.

We exploit the variability in daily mean $\langle CO_2 \rangle$ to infer the north-south gradient through its

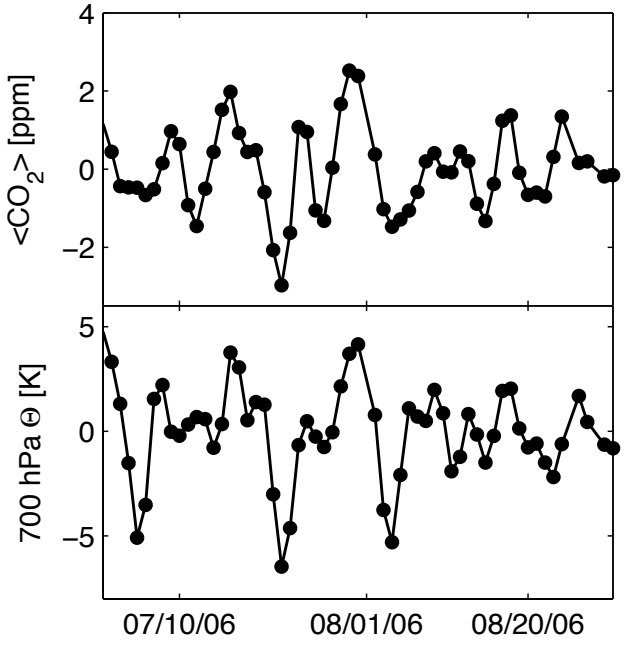

Figure 4.7: (a) Daily mean $\langle CO_2 \rangle$ at Park Falls for two months in summer 2006. Within a week, daily mean $\langle CO_2 \rangle$ varies by up to 5 ppm. (b) Daily mean potential temperature, θ from NCEP reanalysis sampled at Park Falls at 700 hPa. $\langle CO_2 \rangle$ covary because both have strong north-south gradients and variations arise from advection across these gradients.

covariation with free tropospheric potential temperature, θ. Fig. 4.7 shows daily median $\langle CO_2 \rangle$ at Park Falls, Wisconsin for one month in summer 2006. Day-to-day variations are large ($\sim$4 ppm), approximately half the amplitude of the seasonal cycle. These variations correlate with changes in θ at 700 hPa. Cold air (low θ) from the north has lower $\langle CO_2 \rangle$; warm air (high θ) from the south has higher $\langle CO_2 \rangle$. During the growing season, approximately one-third of the variations in $\langle CO_2 \rangle$ at Park Falls can be accounted for by variations in θ (R^2=0.34). We estimate $\partial_y \widehat{\langle CO_2 \rangle}$ at Park Falls to be 1.1 ppb km^{-1} and at Lamont to be 1.3 ppb km^{-1} (Table 4.2).

In Fig. 4.8, we show the TCCON $\langle CO_2 \rangle$ in July and August as a function of meridional displacement relative to Park Falls. A negative meridional displacement signifies that an airmass originated south of Park Falls, while a positive displacement indicates that the airmass originated north of Park Falls. Variations in $\langle CO_2 \rangle$, $\langle CO_2 \rangle'$, are determined relative to annual mean $\langle CO_2 \rangle$ at Lauder. Negative $\langle CO_2 \rangle'$ values, such as those at Park Falls and Bialystok, indicate that during summer,

Table 4.2: Estimated meridional gradient [ppb km^{-1}] in $\langle CO_2 \rangle$ at Park Falls and in free tropospheric [CO_2] from INTEX-NA data and AM2 simulations.

Location	Data	CASA	Boreal enhanced	Early boreal
Park Falls	1.1±0.3	0.6±0.1	0.9±0.2	1.1±0.3
Lamont	1.3 ±0.6	0.4 ±0.2	0.7 ±0.3	0.7±0.3
INTEX	1.1±0.2	0.7±0.2	1.1±0.2	1.2±0.3

$\langle CO_2 \rangle$ is consistently lower than at Lauder. The $\langle CO_2 \rangle'$ values at Lamont are centered around zero, indicating that summer mean $\langle CO_2 \rangle$ is similar at Lamont and Lauder. The range of $\langle CO_2 \rangle$ sampled at sites between 34° and 53°N is ∼9 ppm corresponding to meridional displacements between 3000 km south and 1500 km north of Park Falls at 46°N.

4.3.3 Free tropospheric data from aircraft

Free tropospheric [CO_2] measured during the INTEX-NA mission show a similar correlation with θ. We obtained coincident 700 hPa θ from the NCEP North American Regional Reanalysis (Mesinger et al., 2006) by interpolation along the flight tracks. The in situ data show a positive correlation of CO_2 with θ throughout the free troposphere (Fig. 4.9a). The correlation between [CO_2] and θ is much stronger than that between CO_2 and latitude because synoptic systems passing through the sampled regions obscure the north-south gradient (Fig. 4.9b).

We can quantitatively estimate the north-south gradient in CO_2 from INTEX-NA data using the same approach we use for column data. We designate three free tropospheric layers between 350-800 hPa and a fourth bin for the boundary layer (between the surface and 800 hPa). We recenter [CO_2] and θ by the mean value within each pressure bin and fit a line to relate variations in [CO_2] to variations in θ. The resulting slopes are weighted by the atmospheric mass in each pressure bin and summed. We then normalize by the meridional gradient in θ at 45°N to determine the meridional gradient in CO_2. Quantitatively, the resulting north-south gradient agrees very well with the gradient estimated at Park Falls (Table 4.2).

Analysis of northern hemisphere HIPPO data obtained in January 2009, primarily over the north Pacific, show a smaller north-south gradient that has reversed sign relative to the summer gradient.

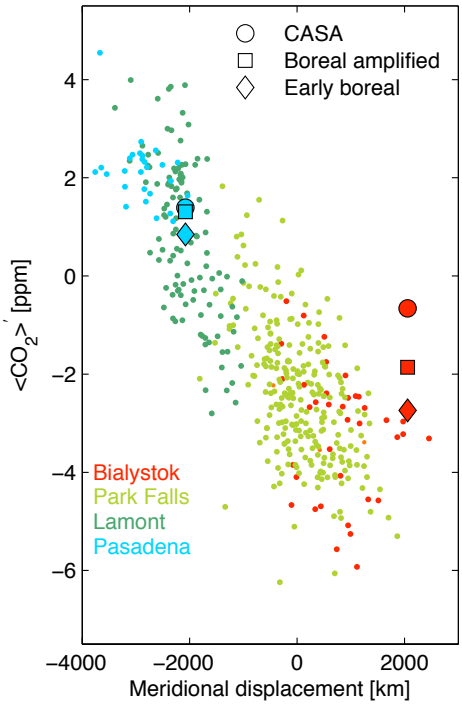

Figure 4.8: July-August $\langle CO_2 \rangle'$ from four northern hemisphere TCCON sites plotted against its meridional displacement relative to Park Falls, determined from variations in θ. Also plotted are the July-August mean $\langle CO_2 \rangle$ for Pasadena (southern most site) and Bialystok (northern most site) from three AM2 simulations with variations on NEE. $\langle CO_2 \rangle$ from a simulation using CASA NEE (circles) underestimates the north-south gradient between the two TCCON sites, while amplified boreal fluxes (squares) and amplified boreal fluxes with an early growing season (diamonds) better capture the north-south gradient during summer.

In Fig. 4.3, we map January 2009 mean 700 hPa θ contours from NCEP reanalysis, and overlay HIPPO partial column $\langle CO_2 \rangle$ with θ at the time of the observation. The observed $\langle CO_2 \rangle$ and θ are generally anti-correlated, as expected for winter. The calculated gradient is -0.2 ppb km^{-1} determined from 52 partial columns in the northern hemisphere are used to constrain this gradient. Fig. 4.10 shows HIPPO free tropospheric $[CO_2]$ (between 350-800 hPa) plotted against observed θ interpolated to 700 hPa colored by latitude; between 30-60°, the $[CO_2]$ contrast is only 2 ppm, smaller than that during INTEX-NA during the northern hemisphere growing season.

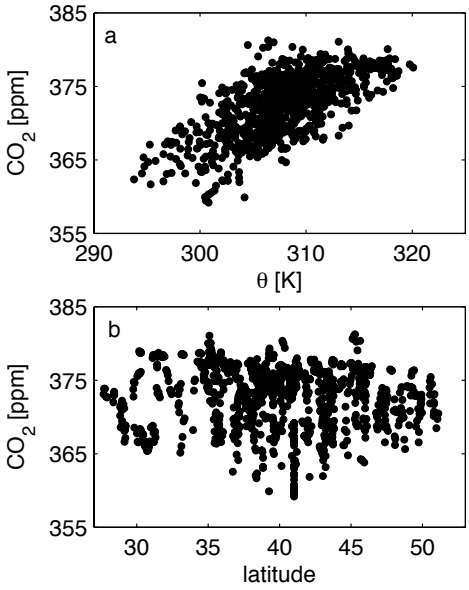

Figure 4.9: Free tropopsheric [CO_2] measured during INTEX-NA plotted against (a) latitude and (b) θ at 700 hPa determined from regional reanalysis data. [CO_2] better correlates with potential temperature because synoptic activity obscures the north-south gradient while a dynamical coordinate reveals it.

4.3.4 Comparison with models

The SCA in $\langle CO_2 \rangle$ is underestimated throughout the northern hemisphere in AM2 with CASA NEE as a boundary condition. Fig. 4.11a shows the seasonal cycle in observed $\langle CO_2 \rangle$ at four northern hemisphere TCCON sites compared to $\langle CO_2 \rangle$ from AM2 with underlying CASA biospheric and standard ocean and fossil fluxes. At all northern hemisphere sites, the amplitude is smaller in AM2 than in the observations; the y-axis reflects the offset from annual mean Lauder $\langle CO_2 \rangle$. Table 4.1 shows that the SCA at all four northern hemisphere TCCON sites is underestimated in CASA simulations by 25-35%, consistent with Yang et al. (2007). There is substantial interannual variability in the SCA at TCCON sites with multiple years of data. We report the median SCA and standard deviation for Park Falls, Lamont, and Lauder. For Bialystok and Pasadena, the data record contains only one complete seasonal cycle. Based on the Park Falls timeseries, drawdown in the northern hemisphere was unusually large in summer 2009, so the Bialystok SCA may represent above average uptake. We average five seasonal cycles from AM2 to estimate a climatological mean SCA for each

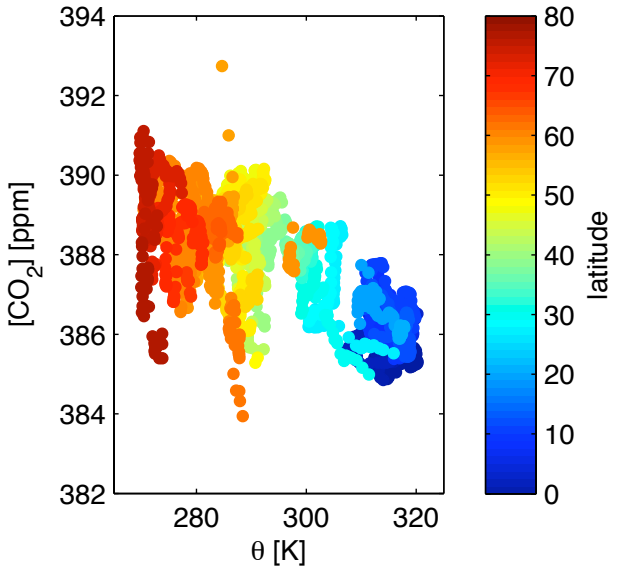

Figure 4.10: Free tropopsheric [CO_2] measured during HIPPO-1 plotted against local θ and colored by latitude. The contrast across the entire northern hemisphere is smaller during winter than the contrast across only the midlatitudes during summer (Fig.9)

site. Such an approach ignores the large interannual variability in fluxes, but shows that on mean, CASA underestimates column SCA in northern hemisphere midlatitudes.

We test the potential for bias in the comparison due to the fact that TCCON data are only obtained when the sun is not obscured by clouds. We limit sampling in AM2 to days in which the cloud fraction in the 2° by 2.5° gridbox corresponding to each TCCON site is less than 70%. This cloud filter removes ∼80% of days in winter and ∼25% of days in the summer at Park Falls. Removing cloud-contaminated days decreases the SCA by ∼5% at Park Falls and Lamont, and has little effect at Bialystok and Pasadena, suggesting that sampling the model only under cloud-free conditions would increase the disagreement between AM2 with CASA fluxes and the observations.

The north-south gradient in $\langle CO_2 \rangle$ during summer is underestimated by ∼45% with CASA fluxes. This is evident from $\partial_y \widehat{\langle CO_2 \rangle}$ estimated at Park Falls or along INTEX tracks (Table 4.2), or simply by inspecting the $\langle CO_2 \rangle$ contrast between TCCON sites. At the gridbox corresponding to Park Falls, $\partial_y \widehat{\langle CO_2 \rangle}$ in AM2 is only 0.6 ppb km^{-1} compared to 1.1 ppb km^{-1} determined from the data. For Lamont, $\partial_y \widehat{\langle CO_2 \rangle}$ is only 0.4 ppb km^{-1}, in contrast to 1.3 ppb km^{-1} determined

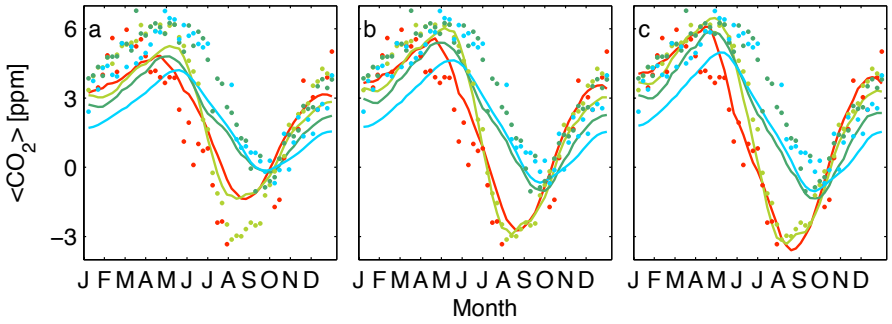

Figure 4.11: Detrended weekly mean $\langle CO_2 \rangle$ at four northern hemisphere TCCON sites (circles) coplotted with simulated $\langle CO_2 \rangle$ from AM2 (solid lines). In each panel, the data are the same, while the simulated seasonal cycles result from (a) CASA net ecosystem exchange, (b) boreal amplified CASA net ecosystem exchange, (c) boreal amplified CASA net ecosystem exchange with an early growing season onset. CASA NEE underestimates the seasonal cycle amplitude in the column at all four sites, while simulations with enhanced boreal exchange better match the data. The colors are the same as in Fig. 1

from the data. When sampling in AM2 is limited to days with less than 70% cloud cover, the estimated gradients decrease by ∼10%. Likewise, the gradient estimated from free tropospheric $[CO_2]$ sampled in the model along INTEX flight tracks is underestimated by 30%. The north-south contrast across TCCON sites is also too small, as is evident in Fig. 4.8. The large red and cyan circles represent summer mean $\langle CO_2 \rangle$ at the northern-most site (Bialystok) and southern-most site (Pasadena). While the mean Pasadena $\langle CO_2 \rangle$ generally agrees with the observations, the simulated mean $\langle CO_2 \rangle$ is too high further north at Bialystok.

We tested whether the use of 1990 annual mean fossil fuel CO_2 emissions could account for the discrepency by running AM2 with 2004-2007 monthly mean fossil fuel emissions (Andres et al., 2011). At all four northern hemisphere TCCON sites, including urban Pasadena, the SCA changes by less than 0.1 ppm when accounting for seasonality in the fluxes. Fossil fuel emissions in 2004-2007 show a more pronounced subtropical source than do 1990 emissions estimates, but the change in the north-south gradient in the column due to updated fluxes is likewise small (< 0.04 ppb km^{-1} at Park Falls).

Simulations with enhanced boreal fluxes better match TCCON diagnostics. Fig. 4.11b-c shows weekly mean timeseries for TCCON data compared to AM2 simulations using boreal-amplified

CASA fluxes and boreal-extended CASA fluxes. The two simulations with amplified boreal fluxes have increased SCAs that bracket the observed column SCAs (Table 4.1). The simulation with CASA NEE amplified by 40% has SCAs that agree at Park Falls and Lamont, while the simulation with amplified NEE and early onset to the growing season somewhat overestimates the SCA at these two sites while better representing the SCA at Bialystok and Pasadena. This experiment has a growing season net flux somewhat greater than 40% in boreal regions because of the longer growing season. Nevertheless, this simulation better matches the phasing of the observations (Fig 4.11b-c), particularly at higher latitude sites. Even sites that are not affected locally by the flux enhancement (i.e., Lamont at 34°N) show an increase in the modeled SCA with the boreal amplified fluxes. The dominant role of the high latitude biosphere in determining the SCA in the subtropics has been noted before (Randerson et al., 1997). There is still a mismatch between simulated and observed $\langle CO_2 \rangle$ at Pasadena due to AM2 having a different mean $\langle CO_2 \rangle$ contrast between Lauder and Pasadena, indicating that the model may be placing Pasadena further into the subtropics dynamically than is realistic.

As the seasonal cycle amplitude increases due to greater summer drawdown in boreal regions in the enhanced simulations, the north-south gradient across TCCON sites grows correspondingly larger (Fig. 4.8). Increasing boreal uptake during summer has little effect on the mean $\langle CO_2 \rangle$ at Pasadena but reduces mean $\langle CO_2 \rangle$ at Bialystok such that the contrast is in better agreement with the data. At Park Falls, $\partial_y \widehat{\langle CO_2 \rangle}$ increases in the boreal-enhanced and boreal-extended simulations to 0.9 and 1.1 ppb km^{-1} respectively, in much better agreement with the observations. At Lamont $\partial_y \widehat{\langle CO_2 \rangle}$ doubles to 0.7 ppb km^{-1}, but is still too small by 50% compared to observations. We caution that Lamont may lie too far in the dynamical subtropics in AM2 for accurate calculation of $\partial_y \widehat{\langle CO_2 \rangle}$.

A comparison of CASA fluxes to reanalysis fluxes from CarbonTracker reveals that atmospheric surface observations suggest greater uptake in the boreal forests. Fig. 4.12 shows the zonal mean July NEE from CASA and 2008 CarbonTracker biospheric fluxes (Peters et al., 2007). NOAA's CarbonTracker data assimilation system uses CASA fluxes as its prior NEE estimate. By assimilating

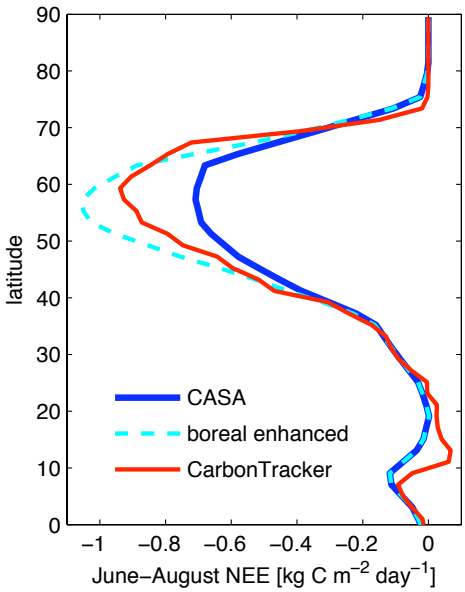

Figure 4.12: Zonal mean net ecosystem exchange averaged for June–August from CASA (solid blue), boreal extended CASA (dashed cyan) and optimized CarbonTracker for 2008 (solid red). CarbonTracker increases boreal fluxes during its assimilation, increasing NEE between 45-65° by 25%.

surface and tower [CO_2] data, CarbonTracker increases growing season NEE by ∼25%, integrated between 45 and 65°N for June through August. Doing so leads to better agreement in $\partial_y\langle CO_2\rangle$ estimated in midlatitudes and results in SCAs somewhat smaller than the SCAs in observations and in AM2 simulations with our boreal flux amplification (Table 4.1).

4.4 Conclusions

Consistent with results from KWS11, TCCON data from Park Falls show that even on hourly timescales, changes in the column are dominated by non-local effects. Diurnal variations in $\langle CO_2\rangle$ only show good agreement with the underlying flux inferred from eddy covariance observations after averaging over several synoptic cycles.

We show that midlatitude column $\langle CO_2\rangle$ data and its correlation with synoptic-scale variations in θ can be used to estimate the large-scale gradient in $\langle CO_2\rangle$. We estimate the north-south gradient at Park Falls to be 1.1 ppb km^{-1}, equivalent to a ∼4 ppm contrast across 30° of latitude. Free

tropospheric [CO_2] data obtained during INTEX-NA are consistent with this meridional gradient. We use θ to define a meridional length scale and show that variations in $\langle CO_2 \rangle$ sampled at northern hemisphere midlatitude TCCON sites are primarily driven by advection of airmasses that originate north and south than the observatories.

TCCON data suggest that northern hemisphere biospheric exchange is underestimated by CASA net ecosystem exchange, as AM2 run with CASA as a boundary condition underestimates both seasonal and spatial variations in $\langle CO_2 \rangle$. From the SCA in $\langle CO_2 \rangle$ at the Park Falls, Wisconsin TCCON site, Yang et al. (2007) concluded that northern hemisphere growing season net flux is underestimated by ∼30% in the mean of TransCom inversions. Here, we use additional TCCON data from other sites to show that this NEE underestimation is traceable to boreal regions. We find that the SCAs at four northern hemisphere TCCON sites are consistent with a boreal NEE integrated over 45-65°N that is increased by 40%. Because column SCA is influenced by hemispheric-scale fluxes, we can simultaneously improve the SCA fit at all four sites through boreal flux amplification. Results from atmospheric inversion studies show that the net northern hemisphere terrestrial carbon sink is sensitive to the gross seasonal fluxes (e.g., Gurney et al. (2002)), so accurately capturing the seasonality in fluxes is crucial to obtaining robust estimates of the terrestrial carbon sink.

We also find that $\langle CO_2 \rangle$ simulated using CASA NEE with amplified boreal fluxes better matches the contrast in $\langle CO_2 \rangle$ across the northern hemisphere TCCON sites. The estimated gradient $\partial_y \widehat{\langle CO_2 \rangle}$ at Park Falls is misrepresented by 45% using CASA fluxes. We confirm that $\partial_y \widehat{\langle CO_2 \rangle}$ represents the large-scale tropospheric gradient using INTEX-NA aircraft data. Both $\partial_y \widehat{\langle CO_2 \rangle}$ at Park Falls and from INTEX data are better represented using boreal amplified fluxes.

While CASA is only one biospheric flux model, it is quite commonly used for biospheric and atmospheric science. An underestimation of terrestrial exchange at high latitudes points to significant error in the description of boreal ecosystem fluxes and suggests further research is necessary to determine the representativeness of available flux data. In terms of future atmospheric CO_2 levels, understanding boreal ecosystem functioning is important, as climate change is focused in this region (Holland and Bitz, 2003). The comparison between CarbonTracker optimized fluxes, which

are informed only by boundary layer CO_2, and fluxes that best represent the TCCON data suggests that column data will provide unique information to inverse models due to its larger footprint and sensitivity to the free troposphere. As the column diagnostics are sensitive to large scale fluxes and transport features, we expect that they will be robust across transport models (KWS11).

We have focused on boreal NEE because it has the largest seasonality in fluxes and therefore has the greatest impact on a large-scale signal such as the column. Simultaneously rectifying the small column SCA in CASA simulations with the small summer north-south gradient can easily be accomplished by drawing down CO_2 in the north. Hypothetically, the north-south gradient could also be increased by greater sources of CO_2 in the south during summer. Such a source of CO_2, however, would reduce the SCA by increasing summer-mean CO_2 in the northern hemisphere.

We expect that TCCON data will provide important large-scale constraints in evaluating flux models. In this paper, we demonstrate that the statistics of variations in $\langle CO_2 \rangle$ can provide important insights into the distribution of fluxes.

Bibliography

Anderson, J. L., Balaji, V., Broccoli, A. J., Cooke, W. F., Delworth, T. L., Dixon, K. W., Donner, L. J., Dunne, K. A., Freidenreich, S. M., Garner, S. T., Gudgel, R. G., Gordon, C. T., Held, I. M., Hemler, R. S., Horowitz, L. W., Klein, S. A., Knutson, T. R., Kushner, P. J., Langenhost, A. R., Lau, N. C., Liang, Z., Malyshev, S. L., Milly, P. C. D., Nath, M. J., Ploshay, J. J., Ramaswamy, V., Schwarzkopf, M. D., Shevliakova, E., Sirutis, J. J., Soden, B. J., Stern, W. F., Thompson, L. A., Wilson, R. J., Wittenberg, A. T., and Wyman, B. L.: The new GFDL global atmosphere and land model AM2-LM2: Evaluation with prescribed SST simulations, J. Climate, 17, 4641–4673, 2004.

Andres, R. J., Marland, G., Fung, I., and Matthews, E.: A 1°x1° Distribution of Carbon Dioxide Emissions From Fossil Fuel Consumption and Cement Manufacture, Global Biogeochem. Cy., 10, 419–429, doi:10.1029/96GB01523, 1996.

Andres, R. J., Gregg, J. S., Losey, L., Marland, G., and Boden, T. A.: Monthly, global emissions of carbon dioxide from fossil fuel consumption, Tellus-B, 2011.

Andrews, A. E., Boering, K. A., Daube, B. C., Wofsy, S. C., Loewenstein, M., Jost, H., Podolske, J. R., Webster, C. R., Herman, R. L., Scott, D. C., Flesch, G. J., Moyer, E. J., Elkins, J. W., Dutton, G. S., Hurst, D. F., Moore, F. L., Ray, E. A., Romashkin, P. A., and Strahan, S. E.: Mean ages of stratospheric air derived from in situ observations of CO_2, CH_4, and N_2O, J. Geophys. Res.-Atmos., 106, 32295–32314, 2001.

Baldocchi, D.: Breathing of the terrestrial biosphere: lessons learned from a global network of carbon dioxide flux measurement systems, Aust. J. Bot., 56, 1–26, 2008.

Bakwin, P. S., Tans, P. P., Hurst, D. F., and Zhao, C. L.: Measurements of carbon dioxide on very tall towers: results of the NOAA/CMDL program, Tellus B, 50, 401–415, 1998.

Berger, B. W., Davis, K. J., Yi, C. X., Bakwin, P. S., and Zhao, C. L.: Long-term carbon dioxide fluxes from a very tall tower in a northern forest: Flux measurement methodology, J. Atmos. Ocean. Tech., 18, 529–542, 2001.

Choi, Y. H., Vay, S. A., Vadrevu, K. P., Soja, A. J., Woo, J. H., Nolf, S. R., Sachse, G. W., Diskin, G. S., Blake, D. R., Blake, N. J., Singh, H. B., Avery, M. A., Fried, A., Pfister, L., and Fuelberg, H. E.: Characteristics of the atmospheric CO2 signal as observed over the conterminous United States during INTEX-NA, J. Geophys. Res.-Atmos., 113, D07301, doi:10.1029/2007JD008899, 2008.

Ciais, P., Tans, P. P., Trolier, M., White, J. W. C., and Francey, R. J.: A Large Northern-hemisphere Terrestrial CO_2 Sink Indicated By the C-13/C-12 Ratio of Atmospheric CO_2, Science, 269, 1098–1102, 1995.

Davis, K. J., Bakwin, P. S., Yi, C., Berger, B. W., Zhao, C., Teclaw, R. M., and Isebrands, J. G.: The annual cycles of CO_2 and H_2O exchange over a northern mixed forest as observed from a very tall tower, Glob. Change Biol., 9, 1278–1293, doi:10.1046/j.1365-2486.2003.00672.x, 2003.

Denning, A. S., Fung, I. Y., and Randall, D.: Latitudinal gradient of Atmospheric CO_2 Due to seasonal exchange with land biota, Nature, 376, 240–243, 1995.

Desai, A. R., Helliker, B. R., Moorcroft, P. R., Andrews, A. E., and Berry, J. A.: Climatic controls in interannual variability in regional carbon fluxes from top-down and bottom-up perspective, J. Geophys. Res.-Biogeosci., 115, G02011, doi:10.1029/2009JG001122, 2010.

Frankenberg, C., Butz, A., and Toon, G.C..: Disentangling chlorophyll fluorescence effects in O_2 A-band spectra of reflected sunlight, J. Geophys. Res.-Atmos., 38, L03801, doi:10.1029/2010GL045896, 2011.

Gloor, M., Sarmiento, J. L., and Gruber, N.: What can be learned about carbon cycle climate feedbacks from the CO_2 airborne fraction?, Atmos. Chem. Phys., 10, 7739–7751, 2010.

Gregg, J. S. and Andres, R. J.: A method for estimating the temporal and spatial patterns of carbon dioxide emissions from national fossil-fuel consumption, Tellus B, 60, 1–10, 2008.

Gregg, J. S., Losey, L. M., Andres, R. J., Blasing, T. J., and Marland, G.: The Temporal and Spatial Distribution of Carbon Dioxide Emissions from Fossil-Fuel Use in North America, J. Appl. Meteorol. Clim., 48, 2528–2542, 2009.

Gurney, K. R., Law, R. M., Denning, A. S., Rayner, P. J., Baker, D., Bousquet, P., Bruhwiler, L., Chen, Y.-H., Ciais, P., Fan, S., Fung, I. Y., Gloor, M., Heimann, M., Higuchi, K., John, J., Maki, T., Maksyutov, S., Masarie, K., Peylin, P., Prather, M., Pak, B. C., Randerson, J., Sarmiento, J., Taguchi, S., Takahashi, T., and Yuen, C.-W.: Towards robust regional estimates of CO_2 sources and sinks using atmospheric transport models, Nature, 415, 626–630, doi:10.1038/415626a, 2002.

Holland, M. M. and Bitz, C. M.: Polar amplification of climate change in coupled models, Clim. Dynam., 21, 221–232, 2003.

Kalnay, E., Kanamitsu, M., Kistler, R., Collins, W., Deaven, D., Gandin, L., Iredell, M., Saha, S., White, G., Woollen, J., Zhu, Y., Chelliah, M., Ebisuzaki, W., Higgins, W., Janowiak, J., Mo,

K. C., Ropelewski, C., Wang, J., Leetmaa, A., Reynolds, R., Jenne, R., and Joseph, D.: The NCEP/NCAR 40-year reanalysis project, B. Am. Meteorol. Soc., 77, 437–471, 1996.

Keeling, R. F., Piper, S. C., and Heimann, M.: Global and hemispheric CO_2 sinks deduced from changes in atmospheric O_2 concentration, Nature, 381, 218–221, 1996.

Keppel-Aleks, G., P. O. Wennberg, and T. Schneider: Sources of variations in total column carbon dioxide, Atmos. Chem. Phys., 11, 3581–3593, 2011.

Marland, G. and Rotty, R. M.: Carbon-dioxide Emissions From Fossil-fuels - A Procedure For Estimation and Results For 1950-1982, Tellus B, 36, 232–261, 1984.

Mesinger, F., DiMego, G., Kalnay, E., Mitchell, K., Shafran, P. C., Ebisuzaki, W., Jovic, D., Woollen, J., Rogers, E., Berbery, E. H., Ek, M. B., Fan, Y., Grumbine, R., Higgins, W., Li, H., Lin, Y., Manikin, G., Parrish, D., and Shi, W.: North American regional reanalysis, B. Am. Meteorol. Soc., 87, 343–360, doi:10.1175/BAMS-87-3-343, 2006.

Olsen, S. C. and Randerson, J. T.: Differences between surface and column atmospheric CO_2 and implications for carbon cycle research, J. Geophys. Res., 109, D02301, doi:10.1029/2003JD003968, 2004.

Peters, W., Jacobson, A. R., Sweeney, C., Andrews, A. E., Conway, T. J., Masarie, K., Miller, J. B., Bruhwiler, L. M. P., Pétron, G., Hirsch, A. I., Worthy, D. E. J., van der Werf, G. R., Randerson, J. T., Wennberg, P. O., Krol, M. C., and Tans, P. P.: An atmospheric perspective on North American carbon dioxide exchange: CarbonTracker, P. Natl. Acad. Sci., 104, 18925–18930, doi:10.1073/pnas.0708986104, 2007.

Randerson, J.T., Thompson, M.V., Conway, T.J., Fung, I.Y., Field, C.B.: The contribution of terrestrial sources and sinks to trends in the seasonal cycle of atmospheric carbon dioxide, Global Biogeochem. Cy., 11, 535–560, 1997.

Rayner, P. J. and O'Brien, D. M.: The utility of remotely sensed CO_2 concentration data in surface source inversions, Geophys. Res. Lett., 28, 175–178, 2001.

Rodgers, C. D. and Connor, B. J.: Intercomparison of remote sounding instruments, J. Geophys. Res., 108, 4116, doi:10.1029/2002JD002299, 2003.

Saatchi, S. S., Houghton, R. A., Alvala, R. C. D. S., Soares, J. V., and Yu, Y.: Distribution of aboveground live biomass in the Amazon basin, Glob. Change Biol., 13, 816–837, doi:10.1111/j.1365-2486.2007.01323.x, 2007.

Stephens, B. B., Gurney, K. R., Tans, P. P., Sweeney, C., Peters, W., Bruhwiler, L., Ciais, P., Ramonet, M., Bousquet, P., Nakazawa, T., Aoki, S., Machida, T., Inoue, G., Vinnichenko, N., Lloyd, J., Jordan, A., Heimann, M., Shibistova, O., Langenfelds, R. L., Steele, L. P., Francey, R. J., and Denning, A. S.: Weak northern and strong tropical land carbon uptake from vertical profiles of atmospheric CO_2, Science, 316, 1732–1735, doi:10.1126/science.1137004, 2007.

Takahashi, T., Sutherland, S. C., Sweeney, C., Poisson, A., Metzl, N., Tilbrook, B., Bates, N., Wanninkhof, R., Feely, R. A., Sabine, C., Olafsson, J., and Nojiri, Y.: Global sea-air CO_2 flux based on climatological surface ocean pCO_2, and seasonal biological and temperature effects, Deep-Sea Res. Pt II, 49, 1601–1622, 2002.

Tohjima, Y., Mukai, H., Machida, T., Nojiri, Y., and Gloor, M.: First measurements of the latitudinal atmospheric O-2 and CO2 distributions across the western Pacific, Geophys. Res. Lett., 32, L17805, doi:10.1029/2005GL023311, 2005.

Vay, S. A., Woo, J. H., Anderson, B. E., Thornhill, K. L., Blake, D. R., Westberg, D. J., Kiley, C. M., Avery, M. A., Sachse, G. W., Streets, D. G., Tsutsumi, Y., and Nolf, S. R.: Influence of regional-scale anthropogenic emissions on CO_2 distributions over the western North Pacific, J. Geophys. Res.-Atmos., 108, 8801, doi:10.1029/2002JD003094, 2003.

Wang, W. G., Davis, K. J., Cook, B. D., Bakwin, P. S., Yi, C. X., Butler, M. P., and Ricciuto, D. A.: Surface layer CO_2 budget and advective contributions to measurements of net ecosystem-atmosphere exchange of CO_2, Agr. Forest Meteorol., 135, 202–214, 2005.

Washenfelder, R. A., Toon, G. C., Blavier, J.-F., Yang, Z., Allen, N. T., Wennberg, P. O., Vay,

S. A., Matross, D. M., and Daube, B. C.: Carbon dioxide column abundances at the Wisconsin Tall Tower site, J. Geophys. Res., 111, D22305, doi:10.1029/2006JD007154, 2006.

Wofsy, S. C. and the HIPPO Science Team: HIAPER Pole-to-Pole Observations (HIPPO): Fine grained, global scale measurements of climatically important atmospheric gases and aerosols, Phil. Trans. R. Soc. A, 369, 2073–2086 , 2011.

Wunch, D., Wennberg, P. O., Toon, G. C., Keppel-Aleks, G., and Yavin, Y. G.: Emissions of greenhouse gases from a North American megacity, Geophys. Res. Lett., 36, L15810, doi:10.1029/2009GL039825, 2009.

Wunch, D., Toon, G. C., Wennberg, P. O., Wofsy, S. C., Stephens, B. B., Fischer, M. L., Uchino, O., Abshire, J. B., Bernath, P., Biraud, S. C., Blavier, J. F. L., Boone, C., Bowman, K. P., Browell, E. V., Campos, T., Connor, B. J., Daube, B. C., Deutscher, N. M., Diao, M., Elkins, J. W., Gerbig, C., Gottlieb, E., Griffith, D. W. T., Hurst, D. F., Jimenez, R., Keppel-Aleks, G., Kort, E. A., Macatangay, R., Machida, T., Matsueda, H., Moore, F., Morino, I., Park, S., Robinson, J., Roehl, C. M., Sawa, Y., Sherlock, V., Sweeney, C., Tanaka, T., and Zondlo, M. A.: Calibration of the Total Carbon Column Observing Network using aircraft profile data, Atmos. Meas. Tech., 3, 1351–1362, 2010.

Wunch, D., Toon, G., J.-F.L, Blavier, Washenfelder, R., Notholt, J., COnnor, B., Griffith, D., Sherlock, V., and Wennberg, P.: The Total Carbon Column Observing Network, Phil. Trans. R. Soc. A, 369, 2087–2112, 2011.

Yang, Z., Washenfelder, R. A., Keppel-Aleks, G., Krakauer, N. Y., Randerson, J. T., Tans, P. P., Sweeney, C., and Wennberg, P. O.: New constraints on Northern Hemisphere growing season net flux, Geophys. Res. Lett., 34, L12807, doi:10.1029/2007GL029742, 2007.

Yi, C., Davis, K. J., Bakwin, P. S., Berger, B. W., and Marr, L. C.: Influence of advection on measurements of the net ecosystem-atmosphere exchange of CO_2 from a very tall tower, J. Geophys. Res.-Atmos, 105, 9991–9999, 2000.

York, D., Evensen, N. M., Martinez, M. L., and Delgado, J. D.: Unified equations for the slope, intercept, and standard errors of the best straight line, Am. J. Phys., 72, 367–375, 2004.

Zhao, C. L., Bakwin, P. S., and Tans, P. P.: A design for unattended monitoring of carbon dioxide on a very tall tower, J. Atmos. Ocean. Tech., 14, 1139–1145, 1997.

Chapter 5

Total column constraints on regional fossil fuel CO_2 emissions

5.1 Introduction

The atmospheric concentration of CO_2 has increased from a preindustrial concentration of 280 ppm to over 390 ppm in 2010. This increase is due to anthropogenic activity: in 2008, 8.7 ± 0.5 Pg C were emitted due to fossil fuel combustion, and 1.2 ± 0.2 Pg C were released to the atmosphere from land use change and biomass burning (Le Quéré et al., 2009). As atmospheric CO_2 concentration has increased, the natural carbon cycle has responded; uptake by oceans and the terrestrial biosphere removes $\sim$50% of anthropogenic CO_2 from the atmosphere annually (Le Quéré et al., 2009).

To date, the focus of most carbon cycle studies (e.g., Gurney et al. (2002); Peters et al. (2007)) has been estimating the strength and global distribution of terrestrial and oceanic sinks of CO_2 using models with prescribed fossil fluxes. This represents a technical challenge because although the gross exchange of carbon between the atmosphere and these natural reservoirs is large, the sinks represent the small residual of the gross fluxes.

Given the risk of global climate change due to increasing atmospheric CO_2 (Meehl et al., 2007), the international community has pursued treaties, such as the Kyoto Protocol, to limit the emissions of CO_2 to the atmosphere. At the UNFCCC Copenhagen Summit in December 2009, the United States indicated that a provision for monitoring and verifying CO_2 emissions is imperative in such a treaty. Currently, the international community relies on self-reporting of greenhouse gas emissions,

but lacks the ability to verify these emissions against independent data (NRC, 2010). Monitoring of fossil fuel emissions from atmospheric CO_2 observations represents a challenge different from attempts to infer natural carbon fluxes. In contrast to natural fluxes, fossil fluxes are geographically concentrated. The net fossil flux is of order the net natural flux globally, but these net fluxes are dwarfed by gross natural exchange, and variations in atmospheric fossil CO_2 are thus masked by spatial and temporal variability in natural CO_2.

Here, we investigate the potential for using total column CO_2, observations from satellites to verify fossil fuel emissions. We illustrate a data-driven approach in which aggregated $\langle CO_2 \rangle$ fields are differenced over emission and upwind regions to determine fossil fuel CO_2 emissions. The value of this approach lies in its simplicity. Because fossil emissions are spatially concentrated, the atmosphere retains a fossil signature that can be used to constrain fluxes from observations. This approach may be attractive in the context of a multilateral treaty. Unlike the most common tool for inferring diffuse natural fluxes, flux inversions (e.g., Gurney et al. (2002)), this approach relies largely on observations and requires no prior assumptions of fossil fluxes that carry over to the ultimate flux estimate. This approach is also straightforward and readily understandable to a general audience.

Total column CO_2 is the vertically integrated mass of CO_2 in the atmosphere above a given location. Although column CO_2 is most sensitive to hemispheric-scale fluxes (Keppel-Aleks et al., 2011), ground-based column data has been demonstrated to provide a mass constraint on anthropogenic fluxes of greenhouse gases in an urban area (Wunch et al., 2009). The column average mixing ratio, $\langle CO_2 \rangle$, is the CO_2 total column, measured in [molecules m^{-2}], normalized by the total column of dry air. $\langle CO_2 \rangle$ is currently measured by satellites such as SCIAMACHY and GOSAT, and will be measured by the upcoming OCO-2 satellite. In addition, $\langle CO_2 \rangle$ is measured by ground-based spectrometers in the TCCON network (Wunch et al., 2011).

In this chapter, we present results from simulated and observed $\langle CO_2 \rangle$ fields. In section 5.2, we describe the model used to simulate $\langle CO_2 \rangle$ fields from surface flux estimates. In section 5.3, we describe the ACOS GOSAT $\langle CO_2 \rangle$. In section 5.4, we describe our analysis of bulk differences in $\langle CO_2 \rangle$ above emission regions and upwind regions and illustrate the utility of using dynamically

defined regions. We also test our model predictions against GOSAT ACOS data. Section 5.5 contains discussion relating to a strategy for observing fossil $\langle CO_2 \rangle$ from space.

5.2 Model

We simulate $\langle CO_2 \rangle$ fields with an atmospheric general circulation model (GCM), using carbon fluxes as boundary conditions. We use the AM2 GCM developed at the NOAA Geophysical Fluid Dynamics Laboratory (Anderson et al., 2004), run at 2° latitude x 2.5° longitude resolution with 25 vertical levels. Fossil emissions are based on monthly mean emissions for the year 2007 (Andres et al., 2011), when net global emissions were 8.1 PgC yr^{-1}. Since then, Chinese emissions have increased by ∼20% although emissions from developed nations have not significantly increased (Boden et al., 2009). The fossil emissions are determined from a proportional-proxy method, in which self-reported fuel consumption data is compiled for countries where available on monthly timescales. Countries that lack data at monthly resolution are paired with a proxy country based on similarities in climate and economics, and self-reported annual emissions are distributed monthly based on patterns in the proxy country (Gregg and Andres, 2008). The geographic distribution of fluxes is determined from energy and electricity consumption, where available; otherwise emissions are gridded based on population (Marland and Rotty, 1984).

In addition to fossil fluxes, we include biospheric and oceanic fluxes in AM2. Biosphere-atmosphere exchange in the AM2 simulations is based on monthly CASA fluxes (Randerson et al., 1997). The net annual exchange is approximately zero at each grid box. The monthly exchange is distributed across each month at three-hourly time steps based on average climatology (Olsen and Randerson, 2004). We have amplified CASA net ecosystem exchange by 40% integrated across the boreal region from 40° to 70° because TCCON data and CarbonTracker reanalysis fluxes suggest that CASA underestimates summer drawdown (Keppel-Aleks et al., 2011b). Ocean exchange is parameterized based on monthly-mean Takahashi fluxes (Takahashi et al., 2002).

We investigate the influence of six source regions on $\langle CO_2 \rangle_{fossil}$: Europe (242°W-28° E, 32-65 ° N; 2007 emissions of 1.2 PgC yr^{-1}); India (68-88° E; 7-33° N; 0.4 PgC yr^{-1}); China (100-135° E,

20-48° N; 2.1 PgC yr^{-1}); Western North America (235-250° E, 30-55° N; 0.3 PgC yr^{-1}); Eastern North America (250-300° E, 25-55° N; 1.4 PgC yr^{-1}); Australia (110-155° E, 20-45° S; 0.1 PgC yr^{-1}). We run AM2 simulations with fossil emissions from individual source regions tagged. We analyze the influence of fossil CO_2 emissions from each of the above source regions on the global distribution of fossil $\langle CO_2 \rangle$ by sampling the daily mean $\langle CO_2 \rangle$ at each model gridbox. We quantify the resulting difference in $\langle CO_2 \rangle_{\text{fossil}}$ and $\langle CO_2 \rangle_{\text{bio}}$ over aggregated regions. Each aggregated region contains an "emission" region that is directly affected by emissions from the source regions, and an "upwind" region. The difference between the mean $\langle CO_2 \rangle$ in the emission region and the upwind region is termed the $\langle CO_2 \rangle$ dipole.

We analyze the dipole for the geographically defined regions demarcated in Fig. 5.1. The boundaries are informed by the zonal anomaly in $\langle CO_2 \rangle_{\text{fossil}}$ in AM2. We also analyze the dipoles for dynamically defined regions. Keppel-Aleks et al. (2011) demonstrated that in simulations with zonally uniform surface fluxes, $\langle CO_2 \rangle$ is very tightly correlated with potential temperature, θ. Therefore, in absence of zonal assymetry in fluxes, isentropic regions would yield dipoles of zero. With flux asymmetries introduced by fossil and biospheric fluxes, regional differences emerge. To implement dynamically defined regions, we fix the coordinates at the northeast and southeast edge of the emission region and calculate the monthly mean θ at 700 hPa at these two points (Fig. 5.2). The north and south boundaries of the emission and upwind regions are then defined by the north and south potential temperature. The geographic boundaries of the regions change each month, but the $\langle CO_2 \rangle$ being averaged in each region is dynamically connected. For India, where wind direction reverses seasonally with the monsoon and where temperature gradients are small, we cannot use θ to define a dynamical region.

5.3 Data

We analyze ACOS $\langle CO_2 \rangle$ data retrieved from GOSAT spectra between April 2009 and March 2011. GOSAT is a carbon-observing satellite developed jointly by the Japanese Ministry of the Environment, the National Institute for Environmental Studies, and the Japan Aerospace Exploration

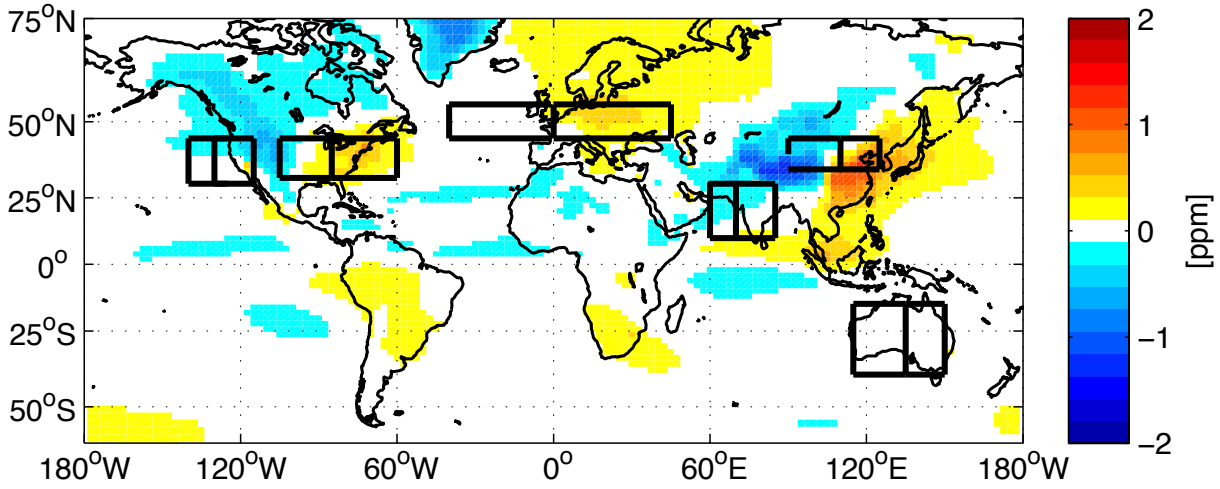

Figure 5.1: Zonal mean fossil $\langle CO_2 \rangle$ Anomaly. Fossil $\langle CO_2 \rangle$ fields from the AM2 GCM are averaged for one year and detrended by the zonal mean to more clearly show the influence of source regions on global $\langle CO_2 \rangle$. Overlaid are black rectangles showing the location of emission and upwind regions used to calculate the geographically defined dipoles in this paper.

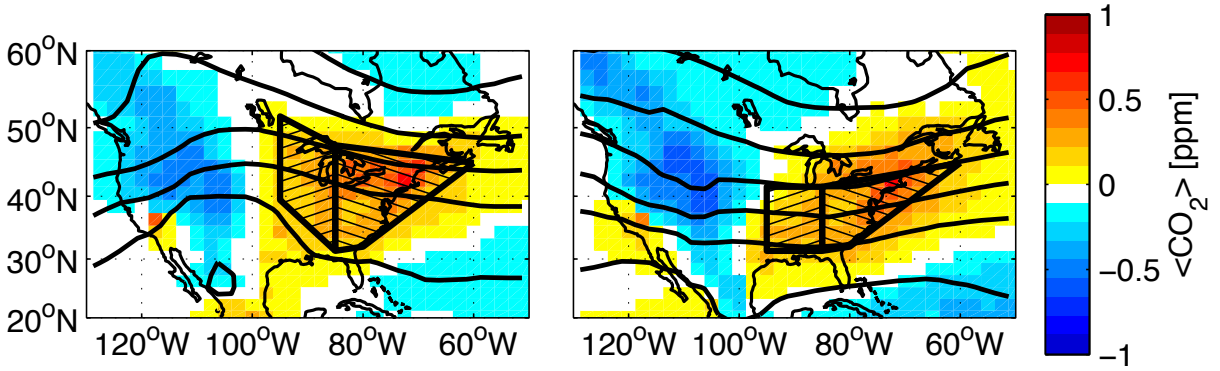

Figure 5.2: May and November dynamically adaptive regions over eastern North America. The eastern and western edges of the emission and upwind regions are fixed, while the north and south boundaries follow isentropes.

Agency. GOSAT samples the same location every three days and a nadir footprint of 10.5 km diameter. Details about the retrieval method are provided by O'Dell (2011). Only data obtained over the land have been validated to date. We therefore test our predictions regarding monthly mean dipoles for China and for Eastern United States, where the corresponding upwind regions are over land. We also analyze dipoles for regions where we expect no contribution from fossil emissions, including Australia and the area west of the upwind-of-China region. We filter the data and apply appropriate corrections as detailed in Wunch et al. (2011b).

5.4 Results

5.4.1 Simulations

The signal in $\langle CO_2 \rangle$ from fossil fuel emissions is small. The enhancement in annual mean $\langle CO_2 \rangle_{\text{fossil}}$ at 2° by 2.5° resolution is at most 1.5 ppm above the zonal mean (Fig. 5.1).

Variability in $\langle CO_2 \rangle_{\text{bio}}$ complicates detection of patterns in $\langle CO_2 \rangle_{\text{fossil}}$ from space. Biospheric fluxes primarily determine the large scale gradient in $\langle CO_2 \rangle$, and advection across those gradients is the dominant source of temporal variations in $\langle CO_2 \rangle$ (Keppel-Aleks et al., 2011). While these variations provide a useful tool to infer the large scale gradient in $\langle CO_2 \rangle$ when measured at a single site on a continuous basis (such as from TCCON observatories), they complicate the interpretation of most satellite data, where observations are made at low temporal resolution. In Fig. 5.3a-d, we show the root mean square variability in $\langle CO_2 \rangle$ in AM2 for two month averages encompassing all seasons. During the northern hemisphere growing season (July-August), when north–south gradients are large, synoptic activity induces RMS variability of order 3 ppm in the northern hemisphere midlatitudes focused along the storm tracks, coincident with the regions in which substantial fossil fluxes occur. Outside the growing season, variations are much smaller suggesting that the signal from fossil fluxes should be easier to diagnose. In the midlatitudes, variability is smallest in fall (October-November), suggesting that detection of trends in the fossil component of $\langle CO_2 \rangle$ may be easiest in this season.

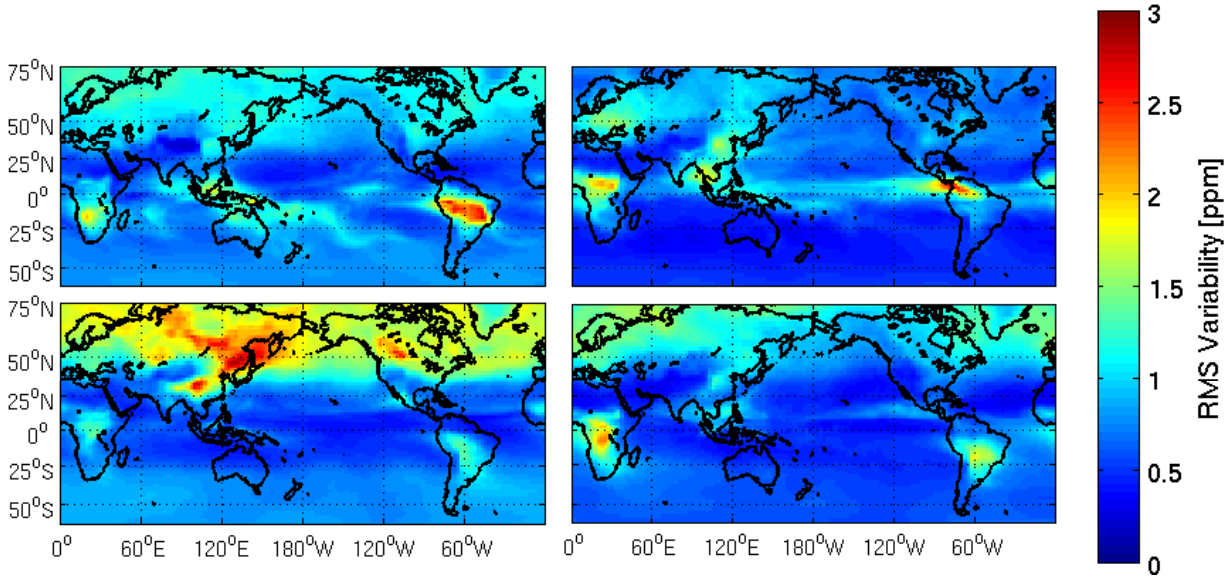

Figure 5.3: variability in $\langle CO_2 \rangle$. (a) RMS variability for January-February. (b) April-May. (c) July-August. (d)October-November

Fig. 5.4 shows the dipole for the aggregated regions shown in Fig. 5.1 resulting from fossil emissions and biospheric fluxes for each month of the year. During the growing season (northern hemisphere summer), variations in $\langle CO_2 \rangle_{\text{bio}}$ dwarf the fossil dipole signature, but the signal to noise ratio is more favorable outside the growing season when spatial gradients owing to natural fluxes are smaller. Much of the biospheric dipole is due to the difference in seasonal cycle in $\langle CO_2 \rangle_{\text{bio}}$ between emission and upwind regions.

The $\langle CO_2 \rangle$ dipoles for dynamically defined regions are less sensitive to biospheric fluxes than are the dipoles for the geographically defined regions. Fig. 5.5 shows the dipole for the four regions with the largest fossil signal: Europe, China, western North America and eastern North America. For Europe, the improvement with a more dynamically consistent definition of the upwind region is relatively smaller than for the other regions because the upwind region is over the ocean so the zonal assymetry in biospheric fluxes is larger. Biospheric uptake over the continent imparts a large negative dipole during the growing season that is not completely removed using our isentropic approach. Outside the growing season, the use of a dynamically defined region lowers the contribution of the biospheric dipole. Both China and eastern North America show a biospheric dipole with much

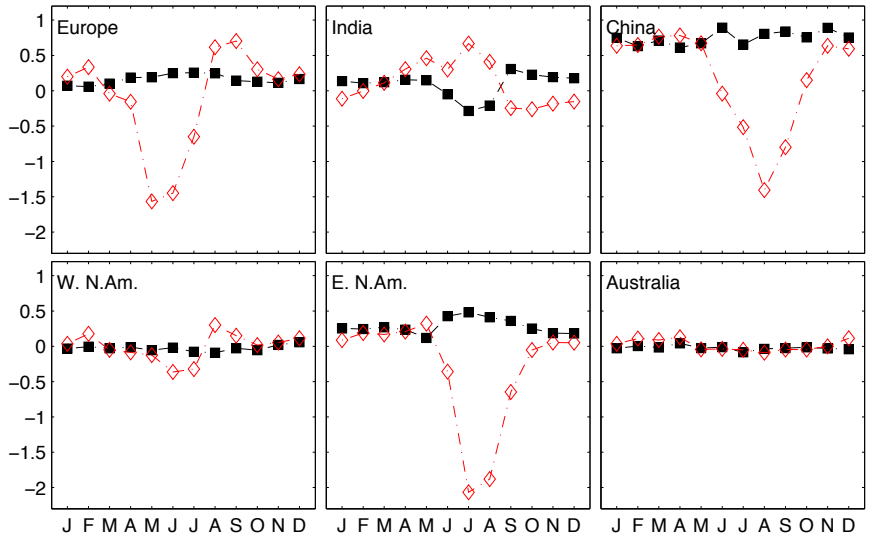

Figure 5.4: Biospheric and fossil $\langle CO_2 \rangle$ dipoles for six aggregated regions. Monthly mean dipole and standard deviation are plotted for biospheric $\langle CO_2 \rangle$ (open circles) and fossil $\langle CO_2 \rangle$ (black squares).

smaller seasonality. For eastern North America, where the emission and upwind are both affected by terrestrial fluxes, the dynamically defined regions lead to a biospheric dipole that is smaller than the fossil dipole year round. For China, the biospheric dipole is reduced by a factor of two during the growing season, but cannot be completely eliminated due to the fact that the Tibetan plateau imparts zonal asymmetry in the biospheric fluxes.

As expected for a passive tracer like CO_2, the constructed dipoles scale linearly with emissions. We simulate $\langle CO_2 \rangle_{\text{fossil}}$ fields with both the base emissions and doubled global emissions; the $\langle CO_2 \rangle_{\text{fossil}}$ dipoles increase by a factor of 2 ± 0.05. To further verify linearity, we simulated $\langle CO_2 \rangle_{\text{fossil}}$ with doubled China emissions. The resulting dipoles were equal to the sum of the dipoles from base global emissions plus the dipoles from tagged China emissions.

Local fossil emissions account for a large fraction of the $\langle CO_2 \rangle_{\text{fossil}}$ dipole in the simulations. Table 5.1 shows $\langle CO_2 \rangle_{\text{fossil}}$ dipoles from tagged emission regions for fall (Oct.–Nov.) compared to $\langle CO_2 \rangle_{\text{fossil}}$ dipoles resulting from global fossil emissions. The off-diagonal elements are close to zero, meaning that the dipoles primarily reflect local emissions. The non-local contribution to the $\langle CO_2 \rangle_{\text{fossil}}$ dipoles are smaller for the dynamically defined regions than for the geographically defined regions, where advected $\langle CO_2 \rangle_{\text{fossil}}$ from other source regions has a relatively larger contribution (not

Table 5.1: $\langle CO_2 \rangle_{fossil}$ dipole [ppm] from regional emissions during October – November. We use dynamically adaptive emission and upwind regions to calculate the dipoles, except for India.

Emission Region	All-Sky Dipole [ppm]					
	Europe	India	China	W. N. Am.	E. N. Am.	Australia
Europe	0.30	-0.01	-0.03	-0.01	-0.03	-0.03
India	0.00	0.14	0.00	0.01	-0.01	-0.01
China	0.08	0.00	0.58	0.01	0.07	0.01
W. N. Am	-0.02	0.01	-0.04	-0.07	-0.01	-0.00
E. N. Am	0.01	-0.00	0.01	-0.02	0.24	-0.00
Australia	0.00	0.00	-0.02	0.01	-0.00	0.01
Global	0.26	0.08	0.76	-0.04	0.25	-0.35

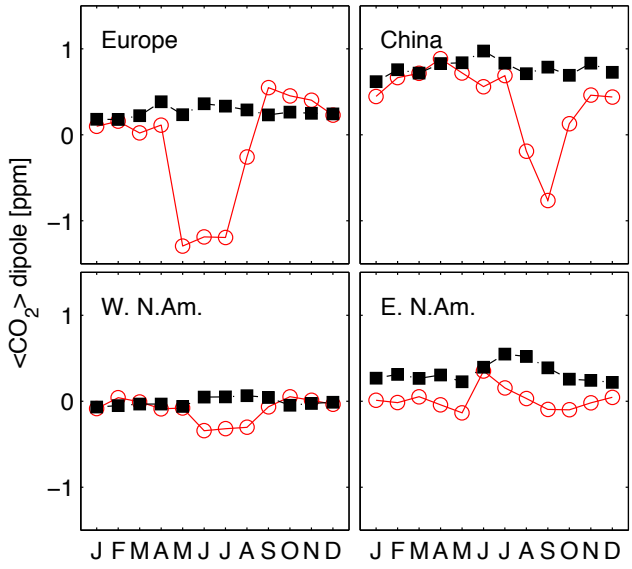

Figure 5.5: $\langle CO_2 \rangle_{bio}$ (red) and $\langle CO_2 \rangle_{fossil}$ (black) dipoles using dynamically adaptive regions shown). The China $\langle CO_2 \rangle_{fossil}$ dipole is augmented by emissions from elsewhere in Asia.

The residence time of fossil CO_2 within the defined emission region affects the expected dipole. To test the sensitivity of the dipole to the residence time, we run the AM2 with fossil fluxes emitted in the free troposphere (∼650 hPa) rather than at the surface. This provides an estimate of the maximum potential error in the dipoles if vertical mixing rates in the model are underestimated. We find that the mean dipoles decrease by only 30±10% due to faster transport times of CO_2 away from the emission region.

A complication of observing $\langle CO_2 \rangle$ from space is interference from clouds. We compare all-sky $\langle CO_2 \rangle_{fossil}$ dipoles to clear-sky $\langle CO_2 \rangle_{fossil}$ dipoles to determine the bias from observing only clear-

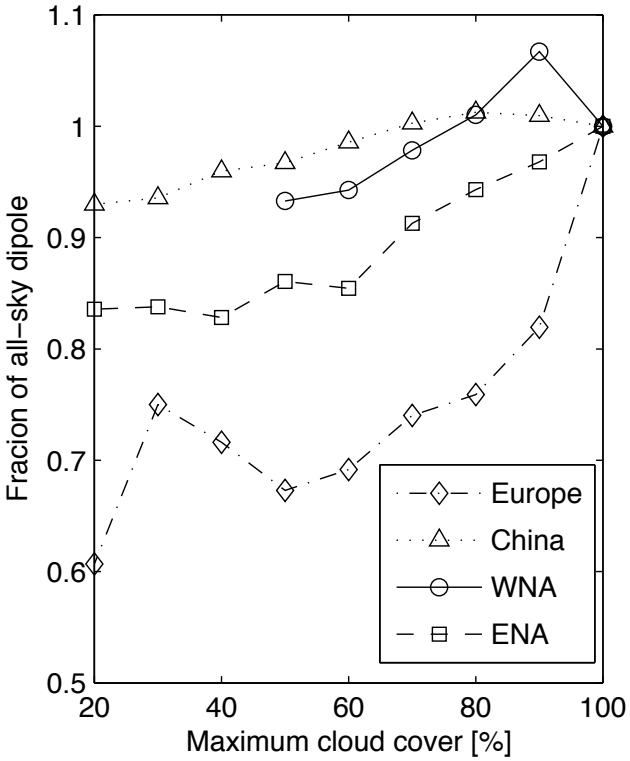

Figure 5.6: Relative change in $\langle CO_2 \rangle$ dipole when data are excluded due to cloud contamination.

sky data, as is expected for space-based observations. We define all-sky as all model grid boxes with cloud cover less than or equal to 99%. Because the fluxes in our model do not interact with meteorology, we explore only the bias due to the covariation of transported CO_2 with cloud cover. GOSAT has a footprint of 85 km^2 and OCO-2 has a footprint of 2 km^2, whereas the AM2 resolution is 2° by 2.5°. More cloud-free retrievals are expected with a smaller satellite footprint, as such a satellite would obtain data between clouds. Fig. 5.6 shows the error in the dipoles for Europe, China, and North America when gridboxes with cloud cover ranging from 20% to 90% are excluded.

The effect of cloud cover on the simulated dipole varies regionally. The China dipole is insensitive to data loss due to cloud cover. Likewise, western North America shows less than 10% bias in the predicted $\langle CO_2 \rangle_{\text{fossil}}$ dipoles when we assume data can be obtained from gridboxes with 50% cloud cover, but there are inadequate gridboxes with less than 50% cloud cover to calculate the $\langle CO_2 \rangle_{\text{fossil}}$ dipole. Obtaining adequate retrievals from a satellite over this region would therefore be quite dependent on the satellite footprint.

5.4.2 Comparison with ACOS GOSAT data

We compare the dipole in GOSAT data for China and the eastern United States with AM2 simulations. We use dynamically defined regions based on NCEP reanalysis potential temperature (Kalnay et al., 1996) to define the emission and upwind regions in which to average GOSAT data. For comparison with AM2, we have increased the simulated China $\langle CO_2 \rangle$ dipole by 25% of the tagged China $\langle CO_2 \rangle_{\text{fossil}}$ dipole to account for the increased emissions compared to 2007.

Because much GOSAT data is filtered due to potential retrieval bias, we average the two years of data seasonally to improve the error statistics (Table 5.2). In regions where simulations predict a discernible fossil signal (China and eastern North America) as well as in regions with no predicted fossil signal (Australia and upwind-of-upwind of China), GOSAT dipoles show large inter- and intra-seasonal variability that do not reflect the simulations. The error estimates in Table 5.2 are the standard error, taking into account the variability predicted by AM2 and the 2.5 ppm (1-σ) precision that characterizes GOSAT data. The seasonal patterns in $\langle CO_2 \rangle$ dipoles are not the same in GOSAT in AM2. Moreover, there are large differences in the AM2 $\langle CO_2 \rangle$ dipole when only data sampled at GOSAT soundings are included compared to when all gridboxes within the dynamically defined regions are included. These biases are smaller in fall and winter, consistent with small spatial gradients and small RMS variability in Fig. 5.3.

5.5 Discussion

Our analysis with simulated $\langle CO_2 \rangle$ fields suggests that fossil CO_2 emissions leave discernable signatures on global $\langle CO_2 \rangle$ fields, although these signatures are small and, even with perfect observations, detection is complicated by variation in natural atmospheric CO_2. The observational challenge is greater considering that satellite data are of moderate precision and spatial coverage is limited by clouds. The simulations show that the fossil signatures respond linearly to changes in fossil emissions. Therefore, changes in observed $\langle CO_2 \rangle$ dipoles could be used to monitor changes in fossil emissions. Carbon forecasts suggest that Chinese emissions will grow by $\sim$3% annually over the next fifty years,

Table 5.2: $\langle CO_2 \rangle$ dipole [ppm] for ACOS GOSAT data and AM2 simulations. The AM2 partial dipole is sampled coincidently with GOSAT data. AM2 full dipoles average all model gridboxes within the dynamically defined regions for all days within the season. GOSAT data are averaged for two years across four seasons: winter (Jan.–Feb.), spring (April-May), summer (July-Aug.), and fall (Oct.–Nov.). The number of points in the ACOS emission and upwind region are listed seasonally.

Season		China	China upwind	E. N. Am.	Australia
Winter	GOSAT dipole	1.4±0.4	-1.1±0.5	-0.4±0.4	-0.1±0.4
	AM2 partial	1.3±0.2	-0.5±0.2	0.1±0.2	0.1±0.1
	AM2 full	1.2±0.2	-0.6±0.2	0.3±0.2	0.0±0.1
	N	98	142	474	418
	N_{upwind}	142	347	329	282
Spring	GOSAT dipole	0.8±0.8	-0.2±0.6	1.0±0.5	-0.5±0.2
	AM2 partial	2.7±0.3	-0.5±0.2	-0.2±0.2	-0.1±0.1
	AM2 full	1.6±0.3	0.3±0.2	0.2±0.2	0.1±0.1
	N	337	459	312	902
	N_{upwind}	459	258	272	1239
Summer	GOSAT dipole	0.8±0.8	-2.1±0.6	1.2±1.0	-0.5±0.2
	AM2 partial	0.8±0.4	-1.5±0.2	1.7±0.5	-0.2±0.1
	AM2 full	1.0±0.4	-0.4±0.2	0.6±0.5	0.0±0.1
	N	109	213	68	1645
	N_{upwind}	213	228	184	2106
Fall	GOSAT dipole	1.6±0.3	-0.2±0.2	0.4±0.3	-0.7±0.3
	AM2 partial	1.1±0.1	-0.2±0.1	0.1±0.1	-0.0±0.1
	AM2 full	1.1±0.3	-0.2±0.1	0.2±0.1	-0.1±0.1
	N	430	851	715	670
	N_{upwind}	851	1188	809	698

essentially two doublings (EIA, 2009). Using the method described here, the observational approach of GOSAT and OCO-2 should quantify a change in emissions with policy relevant accuracy.

Given that in the model, analogous to a satellite with global coverage everyday, we require high regional precision to detect differences in $\langle CO_2 \rangle$ from fossil emissions, it is crucial to have unbiased retrievals. OCO-2 requires single sounding precision of 1 ppm and GOSAT has precision of 2.5 ppm (Miller et al., 2007; Wunch et al., 2011b). With an unbiased retrieval, averaging 400 measurements with 1 ppm precision would yield regional precision of 0.05 ppm. This goal could be more easily achieved with OCO-2 data, which has a much smaller footprint and will therefore be less vulnerable to clouds. Ancillary observations would be quite beneficial, including coretrieved CO and CH_4 from the observing platform (Suntharalingam et al., 2004; Palmer et al., 2006). Such observations would provide a tool to differentiate fossil CO_2 from natural CO_2.

The bias introduced by cloud cover underscores the importance of a small footprint. Additionally, devising a method to remove bias due to cloud cover is necessary for the method to properly monitor fossil emissions from space, as some of the bias in the $\langle CO_2 \rangle$ dipole when AM2 is sampled only where we have GOSAT soundings is due to cloud cover.

Averaging two years of GOSAT data on seasonal timescales does not reveal the regional dipoles expected based on AM2 simulations. When we sample AM2 everywhere in the dynamically designated aggregation regions, we determine significantly different regional dipoles compared to when we sample within those regions according to the distribution of GOSAT data. This finding suggests that OCO-2, with a footprint 40 times smaller than that of GOSAT, may be an easier data set from which to diagnose fossil emission trends as the likelihood of cloud-free scenes will be greater and the spatial coverage will therefore be more complete. Moreover, a greater number of observations will reduce the error in the averaged data.

That we cannot detect the expected regional dipoles on a seasonal basis suggests that the contribution of $\langle CO_2 \rangle_{\text{bio}}$ to the constructed dipoles may be significant and that accurately capturing zonal assymetries and the phasing of biospheric fluxes is necessary. Therefore, tracking $\langle CO_2 \rangle_{\text{fossil}}$ cannot be done without simultaneously optimizing biospheric fluxes through an inversion or data assimilation. We had hoped that computing seasonal dipoles for major emission regions would allow a clear fossil signal to emerge that could be used as a top-down constraint on regional fossil emissions. Based on the current version of the ACOS GOSAT data, this does not seem possible.

The method described here is certainly not the most precise method to infer emissions rates from $\langle CO_2 \rangle$ observations. Techniques such as data assimilation or flux inversions should provide more precise flux estimates. Nevertheless, the approach described here using the mass difference over the industrial and upwind regions has the advantage of being readily understandable to non-scientists and not tied to prior flux estimates. In the context of a policy agreement, such a simple, data-driven approach may prove attractive.

Despite the poor comparison between AM2 and GOSAT data, $\langle CO_2 \rangle$ will play a role ultimately in validating fossil fuel emissions. Satellite observations of $\langle CO_2 \rangle$ will provide large-scale constraints

on surface fluxes, making local observations of boundary layer CO_2 more useful for estimating local emissions. We also note optimistically that retrievals from GOSAT will likely improve as the retrieval algorithm is further developed and potential sources of bias are better characterized. Moreover, the launch of OCO-2 and other satellites will provide more, and potentially better, datasets with which to work.

Bibliography

Anderson, J. L., Balaji, V., Broccoli, A. J., Cooke, W. F., Delworth, T. L., Dixon, K. W., Donner, L. J., Dunne, K. A., Freidenreich, S. M., Garner, S. T., Gudgel, R. G., Gordon, C. T., Held, I. M., Hemler, R. S., Horowitz, L. W., Klein, S. A., Knutson, T. R., Kushner, P. J., Langenhost, A. R., Lau, N. C., Liang, Z., Malyshev, S. L., Milly, P. C. D., Nath, M. J., Ploshay, J. J., Ramaswamy, V., Schwarzkopf, M. D., Shevliakova, E., Sirutis, J. J., Soden, B. J., Stern, W. F., Thompson, L. A., Wilson, R. J., Wittenberg, A. T., and Wyman, B. L.: The new GFDL global atmosphere and land model AM2-LM2: Evaluation with prescribed SST simulations, J. Climate, 17, 4641–4673, 2004.

Andres, R. J., Gregg, J. S., Losey, L., Marland, G., and Boden, T. A.: Monthly, global emissions of carbon dioxide from fossil fuel consumption, Tellus-B, 2011.

Andres, R. J., Marland, G., Fung, I., and Matthews, E.: A 1 1 Distribution of Carbon Dioxide Emissions From Fossil Fuel Consumption and Cement Manufacture,, Global Biogeochem. Cy., 10, 419–429, doi:10.1029/96GB01523, 1996.

Boden, T., G. Marland, and R. Andres: Global, regional, and national fossil-fuel CO_2 emissions, Carbon Dioxide Information Analysis Center, Oak Ridge National Laboratory, U.S. Department of Energy, Oak Ridge, Tenn., U.S.A., doi:10.3334/CDIAC/00001, 2009.

EIA: International Energy Outlook 2009, Tech. rep., U.S Department of Energy, 2009.

Gregg, J. S. and Andres, R. J.: A method for estimating the temporal and spatial patterns of carbon dioxide emissions from national fossil-fuel consumption, Tellus B, 60, 1–10, 2008.

Gurney, K. R., Law, R. M., Denning, A. S., Rayner, P. J., Baker, D., Bousquet, P., Bruhwiler, L., Chen, Y.-H., Ciais, P., Fan, S., Fung, I. Y., Gloor, M., Heimann, M., Higuchi, K., John, J., Maki, T., Maksyutov, S., Masarie, K., Peylin, P., Prather, M., Pak, B. C., Randerson, J., Sarmiento, J., Taguchi, S., Takahashi, T., and Yuen, C.-W.: Towards robust regional estimates of CO_2 sources and sinks using atmospheric transport models, Nature, 415, 626–630, doi:10.1038/415626a, 2002.

Kalnay, E., Kanamitsu, M., Kistler, R., Collins, W., Deaven, D., Gandin, L., Iredell, M., Saha, S., White, G., Woollen, J., Zhu, Y., Chelliah, M., Ebisuzaki, W., Higgins, W., Janowiak, J., Mo, K. C., Ropelewski, C., Wang, J., Leetmaa, A., Reynolds, R., Jenne, R., and Joseph, D.: The NCEP/NCAR 40-year reanalysis project, B. Am. Meteorol. Soc., 77, 437–471, 1996.

Keppel-Aleks, G., Wennberg, P. O., and Schneider, T.: Sources of variations in total column carbon dioxide, Atmos. Chem. Phys., 11, 3581–3593, 2011.

Keppel-Aleks, G., Wennberg, P. O., Washenfelder, R. A., Wunch, D., et al.: The imprint of surface fluxes and transport on variations in total column carbon dioxide, in prep.

Le Quéré, C., Raupach, M. R., Canadell, J. G., Marland, G., Bopp, L., Ciais, P., Conway, T. J., Doney, S. C., Feely, R. A., Foster, P., Friedlingstein, P., Gurney, K., Houghton, R. A., House, J. I., Huntingford, C., Levy, P. E., Lomas, M. R., Majkut, J., Metzl, N., Ometto, J. P., Peters, G. P., Prentice, I. C., Randerson, J. T., Running, S. W., Sarmiento, J. L., Schuster, U., Sitch, S., Takahashi, T., Viovy, N., van der Werf, G. R., and Woodward, F. I.: Trends in the sources and sinks of carbon dioxide, Nature Geoscience, 2, 831–836, 2009.

Marland, G. and Rotty, R. M.: Carbon-dioxide Emissions From Fossil-fuels - A Procedure For Estimation and Results For 1950-1982, Tellus B, 36, 232–261, 1984.

Meehl, G. A., Stocker, T. F., Collins, W. D., Friedlingstein, P., Gaye, A. T., Gregory, J. M., Kitoh, A., Knutti, R., Murphy, J. M., Noda, A., Raper, S. C. B., Watterson, I. G., Weaver, A. J., Zhao, C.:

Global Climate Projections. In Climate Change 2007: The Physical Science Basis. Contribution of Working Group I to the Fourth Assessment Report of the Intergovernmental Panel on Climate Change, Cambridge University Press, 2007.

Miller, C. E., Crisp, D., DeCola, P. L., Olsen, S. C., Randerson, J. T., Michalak, A. M., Alkhaled, A., Rayner, P., Jacob, D. J., Suntharalingam, P., Jones, D. B. A., Denning, A. S., Nicholls, M. E., Doney, S. C., Pawson, S., Boesch, H., Connor, B. J., Fung, I. Y., O'Brien, D., Salawitch, R. J., Sander, S. P., Sen, B., Tans, P., Toon, G. C., Wennberg, P. O., Wofsy, S. C., Yung, Y. L., and Law, R. M.: Precision requirements for space-based X_{CO2} data, J. Geophys. Res., 112, D10314, doi:10.1029/2006JD007659, 2007.

NRC: Verifying Greenhouse Gas Emissions: Methods to Support International Climate Agreements, National Academies Press, 2010.

O'Dell, C., and the ACOS Science Team. In prep.

Olsen, S. C. and Randerson, J. T.: Differences between surface and column atmospheric CO_2 and implications for carbon cycle research, J. Geophys. Res., 109, doi:10.1029/2003JD003968, 2004.

Palmer, P. I., Suntharalingam, P., Jones, D. B. A., Jacob, D. J., Streets, D. G., Fu, Q. Y., Vay, S. A., and Sachse, G. W.: Using CO2 : CO correlations to improve inverse analyses of carbon fluxes, J. Geophys. Res.-Atmos., 111, D12 318, doi:10.1029/2005JD006697, 2006.

Peters, W., Jacobson, A. R., Sweeney, C., Andrews, A. E., Conway, T. J., Masarie, K., Miller, J. B., Bruhwiler, L. M. P., Pétron, G., Hirsch, A. I., Worthy, D. E. J., van der Werf, G. R., Randerson, J. T., Wennberg, P. O., Krol, M. C., and Tans, P. P.: An atmospheric perspective on North American carbon dioxide exchange: CarbonTracker, P. Natl. Acad. Sci., 104, 18925–18930, doi:10.1073/pnas.0708986104, 2007.

Randerson, J. T., Thompson, M. V., Conway, T. J., Fung, I. Y., and Field, C. B.: The contribution of terrestrial sources and sinks to trends in the seasonal cycle of atmospheric carbon dioxide, Global Biogeochem. Cy., 11, 535–560, 1997.

Suntharalingam, P., Jacob, D. J., Palmer, P. I., Logan, J. A., Yantosca, R. M., Xiao, Y., Evans, M. J., Streets, D. G., Vay, S. L., and Sachse, G. W.: Improved quantification of Chinese carbon fluxes using CO_2/CO correlations in Asian outflow, J. Geophys. Res., 109, D18S18, doi:10.1029/2003JD004362, 2004.

Takahashi, T., Sutherland, S. C., Sweeney, C., Poisson, A., Metzl, N., Tilbrook, B., Bates, N., Wanninkhof, R., Feely, R. A., Sabine, C., Olafsson, J., and Nojiri, Y.: Global sea-air CO_2 flux based on climatological surface ocean pCO(2), and seasonal biological and temperature effects, Deep-sea Res. Part II, 49, 1601–1622, 2002.

Wunch, D., Wennberg, P. O., Toon, G. C., Keppel-Aleks, G., and Yavin, Y. G.: Emissions of greenhouse gases from a North American megacity, Geophys. Res. Lett., 36, L15810, doi:10.1029/2009GL039825, 2009.

Wunch, D., Toon, G. C., Wennberg, P. O., Wofsy, S. C., Stephens, B. B., Fischer, M. L., Uchino, O., Abshire, J. B., Bernath, P., Biraud, S. C., Blavier, J. F. L., Boone, C., Bowman, K. P., Browell, E. V., Campos, T., Connor, B. J., Daube, B. C., Deutscher, N. M., Diao, M., Elkins, J. W., Gerbig, C., Gottlieb, E., Griffith, D. W. T., Hurst, D. F., Jimenez, R., Keppel-Aleks, G., Kort, E. A., Macatangay, R., Machida, T., Matsueda, H., Moore, F., Morino, I., Park, S., Robinson, J., Roehl, C. M., Sawa, Y., Sherlock, V., Sweeney, C., Tanaka, T., and Zondlo, M. A.: Calibration of the Total Carbon Column Observing Network using aircraft profile data, Atmos. Meas. Tech., 3, 1351–1362, 2010.

Wunch, D., Toon, G., J.-F.L, Blavier, Washenfelder, R., Notholt, J., COnnor, B., Griffith, D., Sherlock, V., and Wennberg, P.: The Total Carbon Column Observing Network, Phil. Trans. R. Soc. A, 369, 2087–2112, 2011.

Wunch, D., and the ACOS Science Team. In prep.

Appendix A

Appendix

A.1 Removing local pollution

The TCCON site in Pasadena is located within the Los Angeles basin, a megacity with extensive anthropogenic emissions of CO_2 from traffic and other sources. Wunch et al., (2009) document that CO_2 covaries diurnally with CO, due to local pollution. We remove the local anthropogenic component of CO_2 from the timeseries using its correlation with CO. We take a twenty day running mean of the daily median $\langle CO \rangle$, and shift it by 20 ppb so that it skims the bottom of the retrieved $\langle CO \rangle$, representing the clean air $\langle CO \rangle$. We use the following equation to correct $\langle CO_2 \rangle$ based on the offset of coretrieved $\langle CO \rangle$ from its clean air value:

$$\langle CO_2 \rangle_{clean} = \langle CO_2 \rangle - \frac{\langle CO \rangle - (\overline{\langle CO \rangle} - 0.02 ppm)}{\mathrm{EF}} \tag{A.1}$$

where EF represents the emission factor between CO and CO_2 in the basin, equal to 0.011, the slope obtained when $\langle CO_2 \rangle$ is regressed against $\langle CO \rangle$. This value is consistent with combustion efficiency of auto engines of $\sim$99%. The clean air $\langle CO_2 \rangle$ is generally less by $\sim$0.9 ppm compared to the standard retrieval, and the intraseasonal standard deviation is slightly smaller ($\sim$1 ppm).

A.2 Averaging Kernels

Retrieved $\langle CO_2 \rangle$ represents the best estimate of the atmospheric composition given a measured spectrum and a set of prior knowledge about the state of the atmophsere at the time of the observation. Comparing remotely sensed $\langle CO_2 \rangle$ with the model requires proper accounting of the non-ideality of the observing system via the averaging kernel. The averaging kernel, A, represents the sensitivity of the retrieval at any level to the observed spectrum, and is ideally, though rarely, a unit matrix:

$$\hat{x} = A(x - x_a) + x_a + \epsilon. \tag{A.2}$$

As expressed in Rodgers and Connor (2003), the retrieved quantity $\hat{x}$ is sensitive to the prior profile x_a, as well as to the true atmospheric composition x. In an ideal case, A is the identity matrix and $\hat{x}$=x. For our CO_2 retrievals, which use a profile scaling technique, the value of A at each pressure level is generally between 0.5 and 1.5 (see Fig. 3 of Wunch et al. (2010)), depending on solar zenith angle and pressure.

When using remote sensing data in a comparison, the data obtained at higher vertical resolution should be smoothed by the averaging kernel of the data with lower vertical resolution (such as the column, which contains no vertical information). Therefore, in a comparison with eddy covariance observations, which contain information at the surface, we weight the eddy covariance observations by the surface averaging kernel. For comparison with the model output, where we integrate the CO_2 mixing ratio at 25 levels to determine $\langle CO_2 \rangle$, we must apply the averaging kernel at each level.

We apply the FTS averaging kernals to AM2 data by calculating a monthly mean solar zenith angle (SZA) for spectra obtained at each site (Fig. A.1). We likewise calculate the mean CO_2 profile used in GFIT. GFIT uses prior profiles based on GLOBALVIEW-CO2 and incorporates the seasonal cycle and secular increase of CO_2. These prior profiles are recentered to the model $\langle CO_2 \rangle$, maintaining the profile shape. The averaging kernel corresponding to the appropriate monthly mean SZA and the daily a priori profile are interpolated to the pressure profile over each site in AM2. The AM2 $\langle CO_2 \rangle$ incorporating the averaging kernels are then calculated as

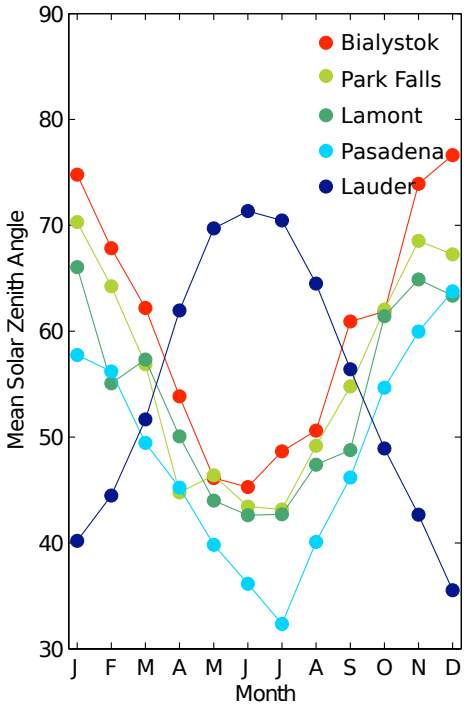

Figure A.1: Monthly mean solar zenith angles for TCCON sites.

$$\langle CO_2 \rangle = \frac{\int A([CO_2] - [CO_2]_p) + [CO_2]_p dp}{\int (1-q)\, dp}, \tag{A.3}$$

where $[CO_2]_p$ is the prior value and q is specific humidity.

We use a simplified parameterization of the averaging kernel for our model (i.e., monthly mean profiles and averaging kernels) to reduce the computational intensity of the comparison and because we use daily mean CO_2 model output, therefore we cannot take into account actual solar zenith angles. We find that applying the FTS averaging kernel to AM2 output has only a small effect on large-scale diagnostics in AM2, such as the seasonal cycle amplitude (< 0.2 ppm) or the estimated north-south gradient (< 0.01 ppb km^{-1}). Therefore, we are satisfied that for these bulk diagnostics, our method is sufficient.

Bibliography

Rodgers, C. D. and Connor, B. J.: Intercomparison of remote sounding instruments, J. Geophys. Res., 108, 4116, doi:10.1029/2002JD002299, 2003.

Wunch, D., Wennberg, P. O., Toon, G. C., Keppel-Aleks, G., and Yavin, Y. G.: Emissions of greenhouse gases from a North American megacity, Geophys. Res. Lett., 36, L15810, doi:10.1029/2009GL039825, 2009.

Wunch, D., Toon, G. C., Wennberg, P. O., Wofsy, S. C., Stephens, B. B., Fischer, M. L., Uchino, O., Abshire, J. B., Bernath, P., Biraud, S. C., Blavier, J. F. L., Boone, C., Bowman, K. P., Browell, E. V., Campos, T., Connor, B. J., Daube, B. C., Deutscher, N. M., Diao, M., Elkins, J. W., Gerbig, C., Gottlieb, E., Griffith, D. W. T., Hurst, D. F., Jimenez, R., Keppel-Aleks, G., Kort, E. A., Macatangay, R., Machida, T., Matsueda, H., Moore, F., Morino, I., Park, S., Robinson, J., Roehl, C. M., Sawa, Y., Sherlock, V., Sweeney, C., Tanaka, T., and Zondlo, M. A.: Calibration of the Total Carbon Column Observing Network using aircraft profile data, Atmos. Meas. Tech., 3, 1351–1362, 2010.